MAX PLANCK INSTITUTE
FOR POLYMER RESEARCH

Ultrafast Carrier Dynamics in Metal-Halide Perovskites by Terahertz Spectroscopy

Heng Zhang

ISBN 978-3-949783-03-6

Ultrafast Carrier Dynamics in Metal-Halide Perovskites by Terahertz Spectroscopy

Heng Zhang

Ultrafast Carrier Dynamics in Metal-Halide Perovskites by Terahertz Spectroscopy

Dutch title:

Ultrasnelle ladingsdrager dynamiek in metaal-halide perovskieten onderzocht met Terahertz spectroscopie

ISBN 978-3-949783-03-6

The work described in this thesis has been performed at the
Max-Planck-Institut für Polymerforschung (MPIP)
Ackermannweg 10, 55128 Mainz, Germany.

Cover picture: a view of Grindelwald (Switzerland), photo by Heng Zhang

Ultrafast Carrier Dynamics in Metal-Halide Perovskites by Terahertz Spectroscopy

ACADEMISCH PROEFSCHRIFT

ter verkrijging van de graad van doctor
aan de Universiteit van Amsterdam
op gezag van de Rector Magnificus
prof. dr. ir. P.P.C.C. Verbeek
ten overstaan van een door het College voor Promoties ingestelde commissie,
in het openbaar te verdedigen in de Agnietenkapel
op dinsdag 29 november 2022, te 15.00 uur

door Heng Zhang
geboren te Shandong

Promotiecommissie

Promotor:	prof. dr. M. Bonn	Universiteit van Amsterdam
Copromotor:	dr. H. Wang	Max Planck Institute for Polymer Research
Overige leden:	dr. E. van Heumen	Universiteit van Amsterdam
	prof. dr. P.C.M. Planken	Universiteit van Amsterdam
	dr. A. Isaeva	Universiteit van Amsterdam
	prof. dr. E. Debroye	KU Leuven
	prof. dr. A.J. Houtepen	TU Delft
	prof. dr. E.C. Garnett	AMOLF

Faculteit der Natuurwetenschappen, Wiskunde en Informatica

PUBLICATIONS COVERED IN THIS THESIS

Chapter 3:

Zhang, H., Debroye, E., Steele, J. A., Roeffaers, M. B. J., Hofkens, J., Wang, H. I. & Bonn, M. *Highly mobile large polarons in black phase $CsPbI_3$*. ACS Energy Lett. **6**, 568-573 (2021).

Chapter 4:

Zhang, H., Debroye, E., Vina-Bausa, B., Valli, D., Fu, S., Zheng, W., Di Virgilio, L., Gao, L., Frost, J. M., Walsh, A., Hofkens, J., Wang, H. I., & Bonn, M. *Experimental quantification of Mott polaron density in lead halide perovskites.* To be submitted.

Chapter 5:

Zhang, H., Debroye, E., Zheng, W., Fu, S., Virgilio, L. D., Kumar, P., Bonn, M. & Wang, H. I. *Highly mobile hot holes in $Cs_2AgBiBr_6$ double perovskite*. Sci. Adv. **7**, eabj9066 (2021).

Chapter 6:

Zhang, H., Debroye, E., Fu, S., González, M. C. R., Feyter, S. D., Hofkens, J., Bonn, M., & Wang, H. I. *Optical switching of hole transfer in double perovskite/graphene heterostructure*. In preparation.

OTHER PUBLICATIONS:

Zheng, W., Sun, B., Li, D., Gali, S. M., **Zhang, H.**, Fu, S., Di Virgilio, L., Li, Z., Yang, S., Zhou, S., Beljonne, D., Yu, M., Feng, X., Wang, H. I. & Bonn, M. *Band transport by large Fröhlich polarons in MXenes*. Nat. Phys. **18**, 544–550. (2022).

Wang, J., Fu, S., **Zhang, H.**, Graf, R., Halim, H., Chen, S., Zheng, W., Bonn, M., Landfester, K., Riedinger, A. & Wang, H. I. *Solution-processed wafer-scale Ag_2S thin films: synthesis and excellent charge transport properties*. Adv. Funct. Mater. 2113147 (2022).

Fu, S., Jin, E., Hanayama, H., Zheng, W., **Zhang, H.**, Di Virgilio, L., Addicoat, M. A., Mezger, M., Narita, A., Bonn, M., Müllen, K. & Wang, H. I. *Outstanding charge mobility by band transport in two-dimensional semiconducting covalent organic frameworks*. J. Am. Chem. Soc. **144**, 7489-7496 (2022).

Fu, S., du Fossé, I., Jia, X., Xu, J., Yu, X., **Zhang, H.**, Zheng, W., Krasel, S., Chen, Z., Wang,

Z. M., Tielrooij, K.-J. , Bonn, M., Houtepen, A. J & Wang, H. I. *Long-lived charge separation following pump-wavelength–dependent ultrafast charge transfer in graphene/WS_2 heterostructures*. Sci. Adv. **7**, eabd9061 (2021).

Keshavarz, M., Debroye, E., Ottesen, M., Martin, C., **Zhang, H.**, Fron, E., Küchler, R., Steele, J. A., Bremholm, M., Van de Vondel, J., Wang, H. I., Bonn, M., Roeffaers, M. B. J., Wiedmann, S. & Hofkens, J. *Tuning the structural and optoelectronic properties of $Cs_2AgBiBr_6$ double-perovskite single crystals through alkali-metal substitution*. Adv. Mater. **32**, 2001878 (2020).

Vasileiadis, T., **Zhang, H.**, Wang, H., Bonn, M., Fytas, G. & Graczykowski, B. *Frequency-domain study of nonthermal gigahertz phonons reveals Fano coupling to charge carriers*. Sci. Adv. **6**, eabd4540 (2020).

Momper, R., **Zhang, H.**, Chen, S., Halim, H., Johannes, E., Yordanov, S., Braga, D., Blulle, B., Doblas, D., Kraus, T., Bonn, M., Wang, H. I. & Riedinger, A. *Kinetic control over self-assembly of semiconductor nanoplatelets*. Nano Lett. **20**, 4102-4110 (2020).

Xu, F., Yu, C., Tries, A., **Zhang, H.**, Klaui, M., Basse, K., Hansen, M. R., Bilbao, N., Bonn, M., Wang, H. I. & Mai, Y. *Tunable superstructures of dendronized graphene nanoribbons in liquid phase*. J. Am. Chem. Soc. **141**, 10972-10977 (2019).

Liu, Z., **Zhang, H.**, Eredia, M., Qiu, H., Baaziz, W., Ersen, O., Ciesielski, A., Bonn, M., Wang, H. I. & Samori, P. *Water-dispersed high-quality graphene: a green solution for efficient energy storage applications*. ACS Nano **13**, 9431-9441 (2019).

ABSTRACT

Solution-processed organic-inorganic hybrid lead halide perovskites (LHPs) have gained tremendous research attention in recent years owing to their superior photovoltaic performance with a certified solar-to-electricity power conversion efficiency (PCE) over 25%. In spite of the great success of the first generation of hybrid perovskites, the chemical instability and the inclusion of the toxic lead element impose fundamental challenges for their practical applications. To address these issues, many recent synthetic efforts have aimed at expanding the library of perovskites towards lead-free and/or chemically stable all-inorganic metal halide perovskites (MHPs).

Employing ultrafast terahertz (THz) time-domain spectroscopy, this thesis investigates the photoexcited charge carrier dynamics and charge transport in newly developed MHPs, focusing on all-inorganic black γ-phase $CsPbI_3$ and lead-free double perovskite $Cs_2AgBiBr_6$. We first unveil that large polarons form in black γ-phase $CsPbI_3$ polycrystalline thin films with a high local mobility up to 270 ± 44 $cm^2V^{-1}s^{-1}$, and polaron-longitudinal optical (LO) phonon interaction governs the charge transport (Chapter 3). With further increasing the photon injection, we conduct the first experimental quantification of the Mott polaron density (~10^{18} cm^{-3}) in lead halide perovskites which is in line with theoretical estimations based on the Feynman polaron model. This effect is found to be universal and independent of the constituted cations and anions, representing an intrinsic property of LHPs. Above the Mott density, excess photoinjected carriers annihilate quickly within tens to hundreds of ps to form a stable, long-lived Mott polaron state (Chapter 4). In the lead-free double perovskite $Cs_2AgBiBr_6$, we reveal excess energy-dependent highly conductive hot carriers, originating primarily from the quasi-ballistic transport of hot holes (Chapter 5). By constructing $Cs_2AgBiBr_6$ double perovskite/graphene heterostructure, we achieve an optical control over hole transfer in both direction and efficiency (Chapter 6). Our studies and findings not only provide a basic understanding on the large polaron transport and interactions in all-inorganic black γ-phase $CsPbI_3$, but also shed light on the intriguing hot carrier transport and charge transfer dynamics (in particular for holes) in double perovskite $Cs_2AgBiBr_6$ and its interfaces. These fundamental insights play a vital role in determining and optimizing the efficiency of optoelectronics of the new generation perovskites.

Table of contents

1 Introduction

1.1 Metal halide perovskite

In 2018, almost 80% of the world's total energy supply comes still from fossil fuels such as coal, oil and natural gas,[1] which leads to the increasing consumption of non-renewable resources and severe environmental issues. To achieve sustainable development and an environmentally friendly society, searching for renewable alternative energy resources has been the ultimate goal for the whole world. One of the most promising candidates is solar energy from sunlight. It's a clean and abundant energy source without greenhouse gas emissions (e.g., CO_2). To make use of solar energy, photovoltaic (PV) technology, i.e., solar cells, has been developed to convert sunlight directly into electricity by photovoltaic effect [2,3]. The first solid-state photovoltaic cell was built by Charles Fritts in 1883 with a solar-to-electricity power conversion efficiency (PCE) of only 1% [4]. The PCE is an important figure of merit for solar cells determining the fraction of incident solar power converted into electricity. After more than 100 years of great efforts in material science and engineering, as well as in device configuration optimization, the current PCEs of solar cells have risen substantially [5]. For example, the PCEs for single-junction solar cells based on single-crystal GaAs and single-crystal silicon are around 27.8% and 26% in 2021, approaching the theoretical limit of ~33%, the so-called Shockley-Queisser limit [5,6]. For multijunction solar cells, the PCEs have even reached more than 40% [5]. The boosted efficiency has promoted the worldwide deployment of solar panels, and now the global solar PV capacity is increasing almost exponentially [7]. However, the current high-efficiency solar cells rely on either high-temperature produced materials (e.g., crystalline silicon) or delicate device configurations (e.g., multijunction solar cells), which leads to a relatively high manufacturing cost. As an alternative, there are emerging low-cost PV technologies, including organic solar cells (OSCs), dye-sensitized solar cells (DSSCs), quantum dot cells, and so on. They usually use inexpensive organic or inorganic materials that can be solution-processed at relatively low temperatures. Though great progress has been made, the resulting PCEs for these low-cost PV cells are still largely lagged behind due to the poor optoelectronic properties of these materials compared to the above-mentioned inorganic semiconductors. For example, the best DSSC so far has a PCE of 15% [8]; the highest PCE achieved now for OSCs is 19.2% [9]. Besides, these emerging cells often experience stability issues which further limit their applications [10]. So, looking for new materials with low-cost, high stability, and superior power conversion efficiencies is a much sough-after goal for achieving the most cost-effective PV devices.

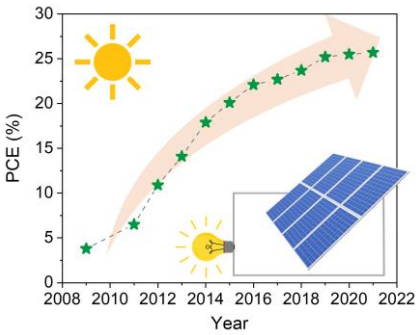

Figure 1.1 | The solar cell efficiency chart. The certified power conversion efficiency evolution of lead halide perovskite solar cells [11].

In the last decade, the world has witnessed a rapid rise of lead halide perovskites (LHPs)-based solar cells with PCEs increasing dramatically as shown in **Figure 1.1** [11]. In 2009, Miyasaka and co-workers constructed the first LHP-based solar cell with LHPs as visible-light sensitizers and achieved a PCE of 3.8% [12]. In 2012, Park *et al.* boosted the PCE to 9.7% by replacing the electrolytes in the perovskite-sensitized solar cells with solid-state hole transport material spiro-MeOTAD [13]. In the same year, Snaith and co-workers further improved the PCE to 10.9% by using LHP thin films instead of nanoparticles as the active layer [14]. Since 2013, various deposition techniques and cell architectures have been developed to optimize the PV performance, and as a consequence, increasingly higher PCEs were achieved [15,16,17]. In 2021, the record PCE for LHP-based single-junction solar cells had increased to more than 25% [18,19]. This efficiency achieved within such a short time is already comparable to that of the conventional inorganic single crystal-based solar cells, for example, single-crystalline silicon solar cells, as mentioned above. What is more appealing about LHPs is their low-temperature solution-processing capability, which significantly reduces the manufacturing cost. The LHPs can be easily prepared at room temperature by different solution deposition techniques, including spin coating, blade coating, spray coating, slot-die coating, inkjet printing, screen printing and so on [20]. The excellent efficiency performance and fabrication simplicity endow LHPs great potential as the most cost-effective light absorbers in PV applications.

Along with the huge success in PV cells, LHPs have also shown superior performance in other photoelectric and optoelectronic applications such as light-emitting diodes (LEDs), lasing, and photodetectors. For instance, the external quantum efficiency (EQE) of LHPs-based LEDs has been boosted to more than 20%, approaching the best efficiencies realized in organic LEDs and conventional semiconductor quantum dots-based LEDs [21]. For the lasing application, LHPs showed a very low lasing threshold of 220 $nJ \cdot cm^{-2}$ and a high-quality factor of 3600 [22]. In addition, considering the near-unity quantum yield and widely tunable wavelength, LHPs

have become strong contenders for nanophotonics. In terms of photodetection, X-ray photodetectors constructed with LHPs achieved an extremely low detection limit of 0.5 $\mu Gy_{air}s^{-1}$ and a high sensitivity of 80 $\mu C\ Gy^{-1}cm^{-2}$ [23]. This performance is even better than the dominating X-ray detecting product α-Se, and endows LHPs great potential to further reduce the X-ray dose for medical inspection and airport security check.

1.1.1 Crystal structure

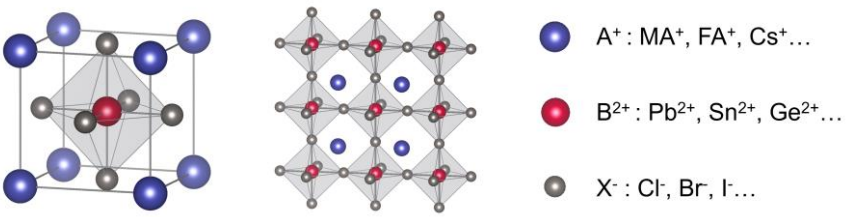

Figure 1.2 | The crystal structure. Schematic illustration of the typical metal halide perovskite crystal structure with the chemical formula of ABX_3.

As shown in **Figure 1.2**, the typical metal halide perovskite crystal structure, with the general chemical formula ABX_3, consists of corner-sharing octahedra $[BX_6]^{4-}$ with A site cations sitting in the inter-octahedra cavities. Very often, this perovskite lattice can be viewed as a combination of two interpenetrating sublattices, that is, $[BX_6]^{4-}$ sublattice and A sublattice [24]. In the chemical formula, A is a monovalent cation which can be either organic (e.g., methylammonium $CH_3NH_3^+$ (MA^+) or formamidinium $CH(NH_2)_2^+$ (FA^+)) or inorganic (e.g., Cs^+, K^+, Rb^+). B is a divalent metal cation such as Pb^{2+}, Sn^{2+}, or Ge^{2+}. Among others, lead-based perovskites are the most investigated material due to their outstanding PV performance. X is a monovalent halogen anion, e.g., Cl^-, Br^-, and I^-. With A site cations being organic molecules, the resulting lead-based perovskites are often called organic-inorganic hybrid LHP (OIHP); while for A being inorganic ions, the material is an all-inorganic LHPs. In addition to the single cation or anion inclusion, mixed cations in A site (e.g., $MA_xFA_{1-x}PbI_3$) or mixed halogen anions in X site (e.g., $MAPbI_xBr_{3-x}$) or mixed both have been extensively explored and shown great potential for realizing stable and efficient optoelectronic applications [25]. Though the high tunability, the composition of the crystal lattice is limited in view of the structural stability. The suitability of different ions or molecules incorporated into the perovskite crystal structure can be evaluated by the Goldschmidt tolerance factor t:

$$t = \frac{R_A + R_X}{\sqrt{2}(R_B + R_X)} \tag{1.1}$$

Here, R_A, R_B and R_X are the radii of the A^+, B^{2+} and X^-, respectively. When $0.9 \leq t \leq 1$, a cubic crystal structure is expected; When $0.7 \leq t \leq 0.9$, octahedra distortions will occur,

resulting in lower structure symmetries including tetragonal, orthorhombic *et al*. For $t < 0.7$ or $t > 1$, non-perovskite structures are usually obtained [26,27].

Benefitting from the diverse chemical composition, the optoelectronic properties of LHPs can be readily and widely modulated. For instance, the bandgap of $MAPbX_3$ can be tuned from ~1.5 eV to ~3.0 eV by varying the halogen anion from I^- to Cl^- [28,29]. This effect leads to wide-ranging management of optical absorption and emission, which can benefit photoelectric applications such as multijunction tandem solar cells [30], and wide color gamut displays [31].

1.1.2 Basic properties

In spite of the facile synthesis, LHPs exhibit superior optoelectronic properties, including high defect tolerance, large absorption coefficient, long carrier lifetime, modest charge mobility, and long carrier diffusion length [32].

Strong optical absorption is a key factor contributing to the success of LHPs in solar cells and other optoelectronic applications. An absorption coefficient of ~10^5 cm^{-1} is commonly reported for LHPs, which is comparable to or even better than that in traditional inorganic semiconductors such as GaAs, CdTe, and CIGS [33,34,35]. Theoretical calculations reveal that such high absorption coefficient in LHPs results from the direct nature of the electronic bandgap and high joint density of states [33]. The high optical absorption is highly desirable for PV cells and makes it possible to reduce the thickness of perovskite films significantly. The high-efficiency perovskite solar cells usually adopt the perovskite film thickness of several hundreds of nanometers (nm). As a comparison, the thickness for crystalline silicon-based solar cells is around 300 um [32]. The thinner films not only reduce the production cost, but also enable more efficient charge collection as charge carriers can now travel less to mitigate the non-radiative recombination loss [32,35].

In addition to the strong absorption, LHPs feature excellent charge transport properties. Despite being low-temperature solution-processed, LHPs are widely reported to possess relatively high charge mobility ranging from several to hundreds $cm^2V^{-1}s^{-1}$ [25]. For example, Sundstrom *et al.* unveiled balanced charge mobility of 25 $cm^2V^{-1}s^{-1}$ in polycrystalline $MAPbI_3$ films [36]. For $MAPbI_3$ single crystals, extremely high charge mobility of 500-800 $cm^2V^{-1}s^{-1}$ was reported by Cooke *et al.* employing broadband THz spectroscopy [37].

Moreover, photogenerated charge carriers in LHPs have a remarkably long carrier lifetime. Chen and co-workers found the lifetime of ~30 μs in $MAPbX_3$ (with *X* being I^- or Br^-) polycrystalline films and ~3 ms in single crystals, respectively [38]. These lifetimes are even longer than those of high-purity conventional inorganic semiconductors (e.g., GaAs). The long-lived charge carriers are recognized to follow the low trap-assisted monomolecular recombination with a coefficient of ~10^6 s^{-1}, as well as considerably low bimolecular (free

electron-hole) recombination with a coefficient of ~10^{-11}-10^{-10} cm^3s^{-1} [38,39].

Benefitting from the modest charge mobility and long carrier lifetime, LHPs show long balanced carrier diffusion length. Snaith and co-workers reported the electron-hole diffusion length exceeding 1 μm in mixed halide perovskite $MAPbI_{3-x}Cl_x$ thin films [40]. Even higher diffusion length >175 um was obtained by Huang *et al.* in $MAPbI_3$ single crystals [41]. This length scale is much larger than the film thickness (100s of nm) utilized in various devices.

Low-temperature solution-processed materials like organic semiconductors, are usually poorly crystallized with lots of defects, which leads to inferior charge transport with low mobilities and short lifetimes [42]. However, the charge carrier properties in LHPs are comparable or even better than those in highly crystalline inorganic semiconductors. This unexpected charge behavior has thus triggered tremendous interest in the scientific community to explore the relevant photophysics and the underlying mechanism.

Even more, LHPs exhibit distinct excited-state characteristics. For instance, researchers observed extremely long-lived hot carriers in LHPs with a lifetime >100 ps, which is two or three orders of magnitude longer than conventional semiconductors [43,44]. In addition, long-range hot carrier transport was reported in LHPs with transport lengths comparable to the film thickness often used in PV cells [45,46]. These fantastic hot carrier properties could enable many novel optoelectronic applications, for instance, hot carrier solar cells. The concept of hot carrier solar cell and exceptional hot carrier properties in LHPs will be discussed in detail in Section 1.2.2.

1.1.3 Perovskites investigated in this thesis

So far, the most efficient perovskite-based PV devices are constructed from organic-inorganic hybrid LHPs, yet the poor intrinsic stability largely limits their practical implementations.

Due to the incorporation of volatile, hygroscopic organic molecules (MA^+ or FA^+) and intrinsic structural instability, hybrid LHPs are susceptible to various external stimuli such as heat, moisture, UV irradiation and pressure [47]. Scientists came up with a variety of device designs and functional materials to encapsulate the LHPs solar cells [48]. For example, Habisreutinger *et al.* used carbon nanotube/polymer composites as a stable hole collection layers to enhance the resistance of LHPs to moisture and heat while maintaining the high PCE [49]. You *et al.* replaced organic transport layers with all-metal-oxides (NiO_x and ZnO) and achieved solar cells with retained efficiency of 90% after 60 days in ambient air [50]. Dai *et al.* included self-assembled monolayer between the electron transport layer and LHP to enhance the interfacial toughing, which results in the enforcement of both mechanical liability and operating stability (more than 4000 hours under 1-sun illumination) [51].

With these great efforts, hybrid LHPs are capable of short-term operation, but still far from the standard requirement of long-term stability for commercialization. Compared to hybrid LHPs, all-inorganic counterparts get rid of the volatile and water-soluble organic constituents, and thus possess better chemical and thermal stability. In 2016, Liang *et al.* reported the fabrication of an all-inorganic perovskite solar cell based on $CsPbBr_3$ and showed no performance degradation over 3 months in humid air and extreme temperatures conditions (100 ℃ and -22 ℃) even without any encapsulation [52]. The most widely used *A* site cation for all-inorganic LHPs is Cs^+ which shows optoelectronic properties resembling its hybrid organic-inorganic counterparts [25]. For single-junction solar cells, $CsPbI_3$ is the most suitable choice considering its relatively small bandgap of ~1.7 eV compared to $CsPbBr_3$ and $CsPbCl_3$ [31]. However, $CsPbI_3$ is in a non-perovskite orthorhombic phase (yellow δ-phase) at room temperature, as shown in **Figure 1.3**. The phase transition from yellow phase to the optically active black cubic phase (black α-phase) occurs at 360 ℃. With decreasing temperature, the black phase undergoes further phase transitions to the tetragonal phase (β-phase) at 260 ℃ and then to orthorhombic phase (γ-phase) at 175 ℃, eventually relaxing to the preferred yellow δ-phase again at room temperature [53]. This phase instability has largely impeded the implementation of $CsPbI_3$ as optical absorbers in PV applications. Recently, various approaches have been applied to stabilize the black phase at room temperature, such as composition engineering, surface passivation, substrate clamping, and biaxial strain [54].

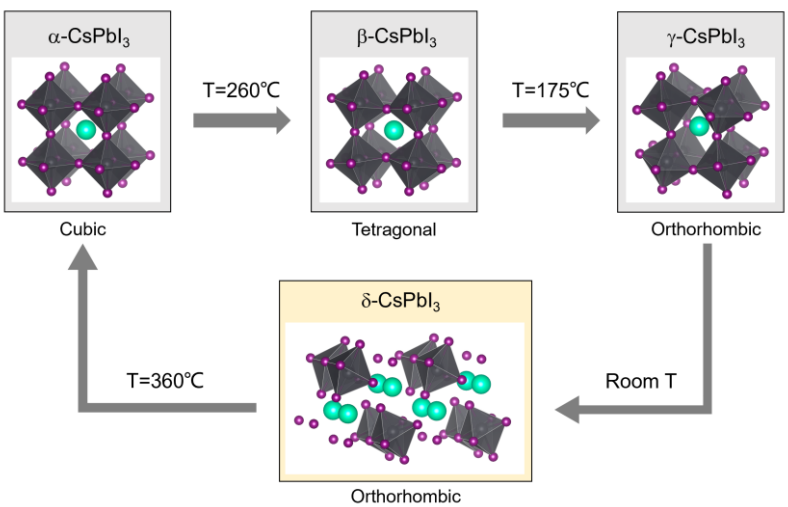

Figure 1.3 | The phase transitions of $CsPbI_3$. Different phase structures and phase transitions of $CsPbI_3$.

Now, the stability of black phase $CsPbI_3$ has been greatly improved, accompanied by superior PV performance. For example, Wang *et al.* reported the black phase $CsPbI_3$ -based solar cell

with a high PCE of 18.4%, 95% of which is retained after 240 hours of continuum illumination at the maximum power point in air [55].

Though LHPs show promising performance in optoelectronic applications, the potential lead leakage imposes strong concerns with distributing LHPs-based devices at large scale in practical implementations. The toxic lead in LHPs can be a threat to the human body and environment [56]. To this end, people have tried different strategies to develop lead-free metal halide perovskites (MHPs) [47]. For example, tin (Sn) halide perovskites have been synthesized and extensively investigated for solar cell applications. However, the device performance is strongly limited due to the easy oxidation of Sn^{2+} to Sn^{4+} because of the high-energy-lying Sn $5s^2$ states [57]. Another approach is to substitute two bivalent lead cations by one monovalent metal cation B'^{+} and one trivalent metal cation B''^{3+}, forming the so-called double perovskite structure with a typical chemical formula of $A_2B'B''X_6$. The schematic of the double perovskite structure is shown in **Figure 1.4a**. So far, one of the most promising double perovskites is $Cs_2AgBiBr_6$ which shows superior stability against moisture and heat, and great performance in optoelectronic applications. For instance, Pan *et al.* employed $Cs_2AgBiBr_6$ single crystal for X-ray detection and revealed a low detection limit with a minimum detectable dose rate of 59.7 nGy_{air} s^{-1} [58]. By a myriad of characteristic techniques, $Cs_2AgBiBr_6$ is found to possess exceptional optoelectronic properties including long carrier lifetime >1 μs [59], long carrier diffusion length >1 μm [60]. However, the best PCE for $Cs_2AgBiBr_6$-based solar cell is still less than 3% despite the great efforts to optimize the film quality and cell configuration [61]. Except for a relatively large indirect bandgap (~2 eV) [62] as shown in **Figure 1.4b**, recent studies claimed that the inferior performance originates from the inherent and extrinsic defect states [61].

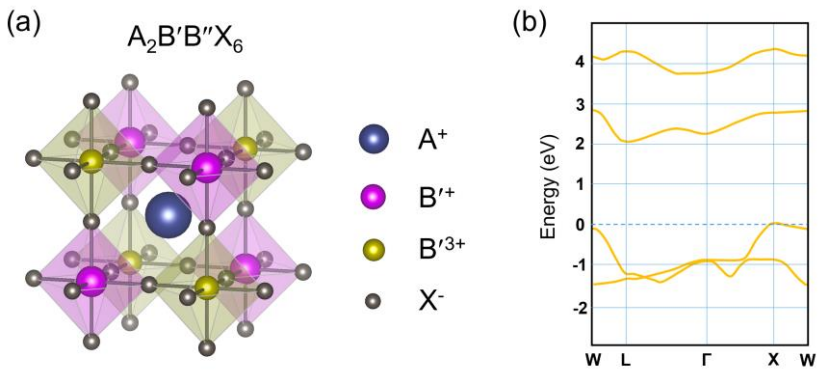

Figure 1.4 | The double perovskite. Schematic illustration of **(a)** double perovskite crystal structure with the chemical formula $A_2B'B''X_6$ and **(b)** the simplified band structure of double perovskite Cs_2AgBBr_6

Though the great potential of black $CsPbI_3$ and double perovskite $Cs_2AgBiBr_6$ for optoelectronic applications, their photophysics has remained largely unexplored compared to hybrid LHPs. Further investigations and understanding of the carrier dynamics and charge transport are crucial for optimizing their performance and extending their functionalities.

1.2 Fundamentals

1.2.1 Polarons

The extraordinary optoelectronic properties in LHPs have driven scientists to interrogate the nature of the charge carriers and fundamental excitations. In 2015, Zhu and Podzorov proposed that the charge carriers in LHPs may be protected as large polarons, which shield the interaction of charge carriers with defects, phonons, and other charges [63]. Since then, the large polaron formation in LHPs was widely demonstrated both in theories and in experiments. In the following, I will briefly introduce the fundamentals of polaron formation and polaron transport.

According to the Kohn-Sham density functional theory, the Schrödinger equation for electrons in the solid is expressed as follows:

$$-\frac{\hbar^2}{2m_e}\nabla^2\psi_n + V_{SCF}\psi_n = E_n\psi_n \tag{1.2}$$

In this equation, the first term is the electron kinetic energy, and the second term is the potential energy experienced by electrons. ψ_n and E_n are the electron eigenfunctions and corresponding eigen energy, respectively. The self-consistent potential V_{SCF} consists of contributions from other electrons and nuclei (or ions). More specifically, this potential reads [64]:

$$V_{SCF}(\boldsymbol{r}) = -\frac{e^2}{4\pi\varepsilon_0}\left[\sum_j \frac{Z_j}{|\boldsymbol{r}-\boldsymbol{R}_j|} - \int \frac{n(\boldsymbol{r}')d\boldsymbol{r}'}{|\boldsymbol{r}-\boldsymbol{r}'|}\right] + V_{xc}[n(\boldsymbol{r})] \tag{1.3}$$

where $\boldsymbol{r}$ is the position vector of the electron, $\boldsymbol{R}_j$ and Z_j are the position vector and atomic number of j-th atom, $n(\boldsymbol{r})$ denotes the electron density at position $\boldsymbol{r}$. On the right side of this equation, V_{xc} is the exchange and correlation potential and the second term is the Hartree potential. The first term on the right side describes the coulomb potential exerted by the nuclei on the electrons, which determines the electron-phonon interactions (EPI). A phonon is a quasi-particle representing the collective motion of atoms in a periodic, elastic structure, specifically in solids. Therefore, the electron energy is affected not only by other charges, but also by the position of the nuclei. When electron transition happens, the nucleus will relax to this new electronic configuration; when the nucleus displaces from its equilibrium position, the surrounding electrons will also adjust themselves accordingly.

In an ionic crystal, the presence of an electron will polarize the surrounding lattice as

illustrated in **Figure 1.5a**. Ions with positive charges will be attracted towards the electron, while negatively charged ions will be repelled away from the electron. When the electron moves, the polarized lattice will move with it. The interaction of the charge carrier (electron or hole) with the displaced surrounding lattice was initially brought forward by Lev Landau in 1933 [65]. To address the resulting electronic combination, in 1946 Solomon Peker started describing it as a quasi-particle named 'polaron' in which an electron or hole is dressed by a virtual cloud of phonons. Depending on the strength of EPI, the spatial extent of the polaron, characterized by polaron radius, can vary dramatically, which leads to two general classifications: large polarons and small polarons. For the large polaron, the charge-induced lattice distortion can spread over many unit cells (i.e., long-range interaction). On the contrary, small polarons localize strongly within a few or even single unit cell (i.e., short-range interaction). Aside from the size, large polaron and small polaron differ drastically in transport, as shown in **Figure 1.5b**. Large polaron features coherent band-like transport with an increased effective mass, and it has a modest mobility (>>1 $cm^2V^{-1}s^{-1}$) which further increases with lowering the temperature. While due to the strong localization, small polaron propagates by thermally activated incoherent hopping with much lower mobility (<<1 $cm^2V^{-1}s^{-1}$). It has an opposite temperature dependence from the large polarons [66].

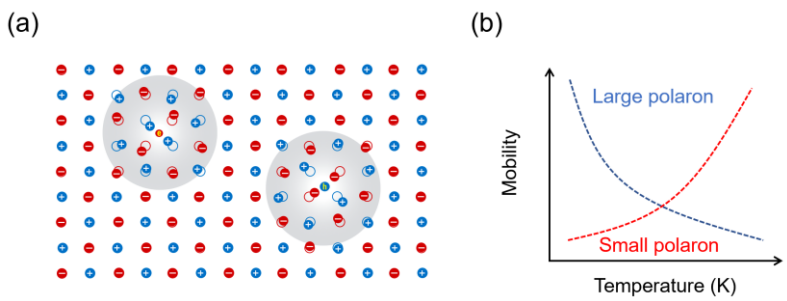

Figure 1.5 | The polarons. The schematic illustration of **(a)** polarons in the ionic lattice and **(b)** the temperature-dependent mobility of large and small polarons.

The strength of EPI can be evaluated by the dimensionless Fröhlich electron-phonon coupling constant [67]:

$$\alpha = \frac{e^2}{4\pi\hbar}\left(\frac{1}{\varepsilon_\infty} - \frac{1}{\varepsilon_s}\right)\sqrt{\frac{m_b^*}{2\hbar\omega_{LO}}} \tag{1.4}$$

where ε_∞ and ε_s are the high-frequency (electronic, ion-clamped) and static (electronic and ionic) dielectric constants (in units of vacuum permittivity ε_0) respectively, ω_{LO} is the characteristic LO phonon frequency of the coupled modes, and $\hbar$ is the reduced Planck constant. For $\alpha < 6$, the polaron size lies in the large or intermediate range; while for $\alpha > 6$,

small polarons are often formed.

Theoretically, Herbert Fröhlich [68] and Theodore Holstein [69] set the groundwork for rigorous quantum-field Hamiltonians for large and small polarons, respectively. So, the large polaron is also known as Fröhlich polaron and small polaron is named as Holstein polaron. Originally, Fröhlich constructed the first quantum-field Hamiltonian describing independent electrons interacting with polar optical phonons [68]. Since then, it has been very challenging to obtain an appropriate solution that applies to all coupling regions. In 1955, Feynman utilized the path integral formulation innovatively to calculate the ground state of a polaron on the basis of Fröhlich Hamiltonian, which is applicable for arbitrary coupling strength α [70]. In his model, the Hamiltonian is expressed as a coupled electron to a finite mass with a harmonic spring constant. Later, Ōsaka further improved Feynman's athermal variational solution to finite temperatures by providing finite-temperature free energies for the coupled electron-phonon system [71]. The ground state of the polaron can be obtained by minimizing the free energy via modulating two variational parameters.

As a typical ionic, polar semiconductor, the incredible photovoltaic performance combined with the low-temperature solution processability has triggered people to ask if polarons are formed and play an important role in LHPs [63]. Due to the large contrast of the static and high-frequency dielectric constants in LHPs [72,73], the calculated coupling constant α ranges from 1 to 3 based on Equation 1.4, which makes LHPs favorable for large polaron formation. Furthermore, the polaron formation can effectively screen the Coulomb interaction of charge carriers with defects, phonons and opposite charges. This can, in principle, explain the unexpected optoelectronic properties in LHPs, including high defect tolerance, modest charge mobility, low bimolecular recombination rate and thus long carrier lifetime.

To collect the evidence of large polaron formation in LHPs, a variety of experiments have been conducted. Miyata *et al.* employed the time-resolved optical Kerr effect (TR-OKE) to probe the phonon response before and after the photoinduced charge injection, in combination with first-principle calculations [74]. They found the increased overdamping of low-frequency modes from inorganic sublattice of $[PbBr_3]^-$ upon photoinjection, which is mainly responsible for the polaron formation. Guzelturk *et al.* visualized the polaron-induced local lattice strain directly by momentum-resolved phonon spectroscopy [75]. Puppin *et al.* observed ~50% enhancement of the hole band mass by angle-resolved photoemission spectroscopy (ARPES) compared to the calculation from density functional theory, which provides a strong evidence of the polaron-induced mass renormalization [76].

As a figure of merit in charge transport, polaron mobility μ has been widely studied theoretically and experimentally. Based on the obtained polaron state from Feynman's model, the polaron mobility formula was initially proposed by Feymann, Hellwarth, Iddings and

Platzman (FHIP) by simply considering the polaron center-of-mass in a weak field [77]:

$$\mu_{FHIP} = \left(\frac{w}{v}\right)^3 \frac{3e}{4m_b} \frac{e^{\beta}}{\omega\alpha\beta} e^{\frac{v^2-w^2}{w^2 v}} \tag{1.5}$$

Here, w and v are variational parameters in Feynman's model, m_b is the bare band effective mass, $\beta = \frac{\hbar\omega}{k_B T}$ is the reduced thermodynamic temperature, ω is the angular frequency of the phonon mode, α is the electron-phonon coupling constant.

However, FHIP mobility was quickly realized to be pathological for high temperatures. Starting from the Boltzmann equation, Kadanoff attempted to release the low-temperature limit and derived a mobility formula that reads [78]:

$$\mu_K = \left(\frac{w}{v}\right)^3 \frac{e}{2m_b} \frac{e^{\beta}}{\omega\alpha} e^{\frac{v^2-w^2}{w^2 v}} \tag{1.6}$$

Recently, Hellwarth and Biaggio got rid of the power expansion with which FHIP derived their formula, and performed the more accurate contour integral for polaron free energy. The derived mobility is expressed below [79]:

$$\mu_H = \left(\frac{w}{v}\right)^3 \frac{3e}{m_b} \frac{\sqrt{\pi}\sinh\left(\frac{\beta}{2}\right)}{\omega\alpha\beta^{\frac{5}{2}}} K^{-1} \tag{1.7}$$

in which K represents the integral of the polaron response to the first-order change in the driving force.

Following the essence of the Feynman-Ōsaka variational approach, Jarvist Moore Frost calculated the polaron mobilities in LHPs, including both hybrid and all-inorganic types [72]. Quantitative agreement was found between the calculations and experiments from time-resolved microwave conductivity measurements.

Other than mobility, the polaron effective mass m^* and polaron radius r_p can be approximated as well following Feynman's theory [74]:

$$m^* = m_b\left(1 + \frac{\alpha}{6} + \frac{\alpha^2}{40} + \cdots\right) \tag{1.8}$$

$$r_p = \left(\frac{3\hbar}{2m_{red} \cdot v \cdot 2\pi\omega}\right)^{\frac{1}{2}} \tag{1.9}$$

where $m_{red} (= m_b \cdot \frac{v^2-w^2}{v^2})$ is the reduced mass of the coupled charge-harmonic oscillator.

1.2.2 Hot charge carriers

Theoretically, the highest PCE that can be achieved for a standard single-junction solar cell under 1-sun illumination is ~ 33%, which is the so-called Shockley-Queisser limit (SQ limit) [6]. This limited conversion efficiency results mainly from two energy losses: 1) The solar irradiation with photon energies below the bandgap of the semiconducting absorbers will

directly transmit through the solar cell instead of being absorbed; 2) The energy loss from energetic hot carriers. The solar irradiation with photon energies above the bandgap of the semiconducting absorbers will be absorbed and generate charge carriers with energies above the band edges (the maximum of the valence band or the minimum of the conduction band), as shown in **Figure 1.6**. These are the so-called hot carriers. However, instead of being converted to electrical power, these hot carriers will quickly lose their excess energy as heat and relax to the band edges. This energy loss represents one of the main limitations to PCEs in solar cells. Thermodynamic calculations predict a ~66% PCE if these hot carriers can be extracted and collected by the electrodes instead of losing their excess energy as wasted heat [80]. To this end, a novel concept for a solar cell, i.e., hot-carrier solar cell, has long been proposed to greatly promote the power conversion efficiency by extracting and utilizing these hot carriers [80]. The basic idea is that: after the solar absorption, there is an efficient hot carrier extraction by energy selective contacts (ESCs), which have a narrow energy range to avoid further hot carrier energy loss within the contacts. The energy of this contact is higher than the band edge, leading to a higher output voltage [81]. The prerequisite for realizing such an efficient solar cell is to slow down the hot carrier cooling process so as to facilitate the hot carrier extraction by ESCs. In addition, these hot carriers should be able to travel sufficiently fast and far to mitigate the energy loss during the transport within the absorber. In the last years, looking for materials with long hot carrier lifetimes and excellent transport lengths has been a 'holy grail' for achieving hot carrier solar cells.

In addition, hot carriers play critical roles in many other optoelectronic applications, for instance, photocatalysis and photochemistry [82]. So, understanding and controlling hot carriers is of fundamental importance for further efficiency enhancement in optoelectronic devices and for realizing hot carrier-based innovative technologies. Before discussing the hot carrier studies in LHPs, let's first review the hot carrier dynamics and transport properties in conventional semiconductors.

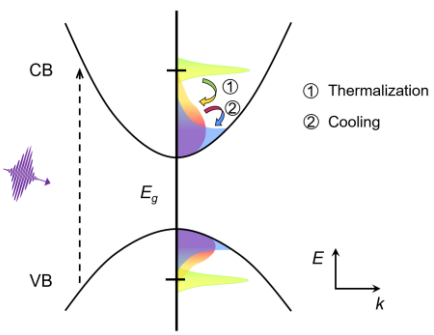

Figure 1.6 | Hot carrier generation and relaxation in semiconductors. The temporal evolution of hot carrier population created by the photoexcitation.

Initially, photoexcitations with photon energies higher than the bandgap induce interband polarization, which is a superposition of ground states and excited states [83]. After a short dephasing time, the coherences are destroyed by a variety of scattering processes, and some hot electrons remain in the conduction band and equivalent hot holes in the valence band. Originally, these hot carriers follow non-thermal distribution thermodynamically, and cannot be described by a temperature. The hot carriers will subsequently experience ultrafast energy exchange via mainly carrier-carrier scattering, resulting in a Fermi-Dirac distribution characterized by a temperature T_c higher than the lattice temperature T_L. This process is called thermalization, and it has been reported to occur within the timescale of 100 fs in conventional semiconductors, e.g., GaAs [83].

Afterwards, the thermalized hot carriers dissipate their excess energy through mainly optical phonon emission and relax to the band edges, becoming cold carriers. The non-equilibrium optical phonon population will decay into acoustic phonons, which further dissipate as heat. Eventually, thermodynamic equilibrium is achieved between the electronic system and the surrounding lattice, i.e., T_c=T_L. This process is known as hot carrier cooling, which usually happens on a sub-ps timescale due to the efficient carrier-optical phonon interaction. For example, the measured hot carrier cooling time in silicon is ~350 fs under solar illumination [84].

Regarding the transport, distinct hot carrier transport behavior has been observed as well. After thermalization, hot carriers are usually subject to diffusive transport in which hot carriers experience quick scattering during diffusion. In this regime, hot carriers usually have drastically reduced mobility compared to cold carriers because of the enhanced carrier-phonon interactions from the increased phase space. *Ab initio* theoretical calculations have revealed a strong and positive correlation between the hot carrier scattering rates and electronic density of states (DOS) [85,86]. Besides, it confirms the dominant role of hot carrier-optical phonon scattering over other scattering mechanisms, e.g., carrier-carrier scattering. In silicon, the scattering time (the inverse of scattering rate) for energetic hot carriers is ~10 fs, while for cold carriers ~100 fs [85]. A similar result hold for GaAs [86]. The short scattering time or equivalently large scattering rate leads to substantially reduced hot carrier mobility, thus short transport length (tens of nm) considering the short hot carrier lifetime as well. On the other hand, hot carrier transport without scattering or very few scattering has also been reported [46,87,88]. This is the so-called ballistic or quasi-ballistic transport. This can occur right after the hot carrier generation before the first collision with other charges, or when hot carriers have enough energy to avoid other scattering, e.g., defect scattering.

Since the discovery of the extraordinary optoelectronic performance of LHPs, the hot carrier properties in LHPs are also studied extensively by a variety of pump-probe techniques.

Surprisingly, the hot carrier lifetime in LHPs is found to be two or three orders of magnitude longer than that in conventional organic and inorganic semiconductors. For instance, by transient absorption (TA) spectroscopy, Beard *et al.* observed a hot carrier lifetime of ~60 ps in $MAPbI_3$ with the pump photon energy of 3.10 eV and the excitation fluence of 6×10^{18} cm^{-3} [43]. They attributed the long hot carrier lifetime to the hot phonon bottleneck effect in which the efficient optical phonon emission combined with retarded optical-to-acoustic phonon conversion gives rise to accumulated non-equilibrium optical phonon populations. These optical phonons can be re-absorbed by intraband charge carriers, leading to a slow-down of net energy loss of hot carriers [81]. In addition, Auger heating can be responsible for further suppression of hot carrier cooling at even higher carrier densities above ~10^{19} cm^{-3} [89]. In this mechanism, non-radiative electron-hole recombination transfers its energy to another charge in the conduction or valence band, which raises its energy again. Yet, different from the high photoexcitation situation, Zhu and co-workers reported long-lived (~100 ps) hot carriers in both $MAPbBr_3$ and $FAPbBr_3$ single crystals at a low pump fluence of 7×10^{16} cm^{-3} employing time-resolved photoluminescence spectroscopy (TRPL) [44]. Moreover, they observed that the hot carrier cooling is accelerated with increasing the pump fluences and lowering the sample temperature. This observation is in contrast to the hot phonon bottleneck effect in which a high carrier density is necessarily required. With time-resolved optical Kerr effect, the authors assigned this phenomenon to the Coulomb screening of hot carrier interaction with LO phonons by fast large polaron formation.

Not only long lifetimes but also the long-range transport of hot carriers has been observed in LHPs. Using TA microscopy, Huang *et al.* directly recorded the hot carrier transport length and resolved two distinct transport regimes for hot carriers [45]. Immediately after the photoexcitation, the hot carriers first experience quasi-ballistic transport of ~230 nm within the time resolution of 300 fs. The long-range ballistic transport was also reported later by Sung *et al.* who employed TA microscopy as well but with much higher temporal (10 fs) and spatial (10 nm) resolution [46]. They observed that non-thermalized hot carriers propagate ballistically over 150 nm within the first 20 fs. During the next tens of ps, i.e., the cooling process, hot carriers travel through 600 nm before reaching the diffusive transport of cold carriers [45].

The substantially slowed hot carrier cooling and excellent transport range endow LHPs great potential for hot carrier-based optoelectronic devices, especially the hot carrier solar cells.

1.2.3 Charge transfer

Charge transfer (CT), or electron transfer (ET) (equivalent to hole transfer in the opposite direction), is a dynamic process occurring at the interface of two constituent materials. When putting two materials in contact with each other, charge flow can happen from one material to

another across the interface due to the mismatch of chemical potentials. As an example, two metals A and B, with different Fermi energies E_F, are connected directly, as shown in **Figure 1.7**.

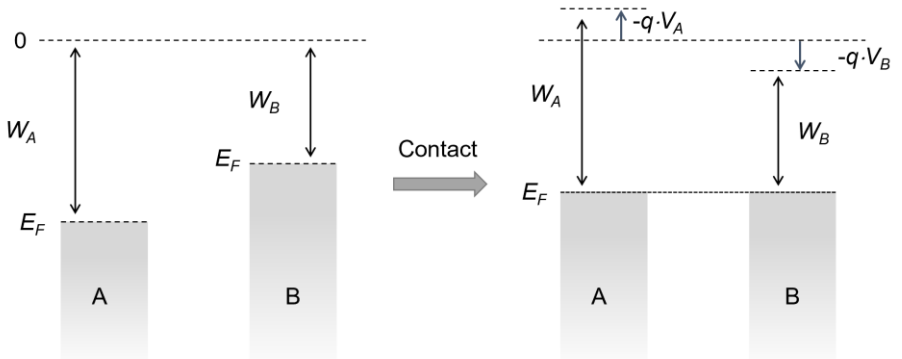

Figure 1.7 | Charge transfer between two metals with different work functions. The schematic illustration of the band diagrams of two metals before and after the contact.

Due to the different chemical potentials manifested by different Fermi energies, electrons will transfer from metal B to metal A. As a consequence, there are extra electrons accumulating in metal A, which induces a negative electrostatic potential $V_A < 0$. The opposite holds for metal B, i.e., a positive electrostatic potential $V_B > 0$. Therefore, extra potential energy ($-q\cdot V_A > 0$) is added to the electrons in metal A, which shifts the whole energy band upwards. The negative potential energy ($-q\cdot V_A < 0$) shifts the energy band of metal B downwards until the Fermi levels equal each other. Eventually, an equilibrium condition is established between the two metals. The same mechanism also applies to metal-semiconductor, and semiconductor-semiconductor interfaces. More specifically, for the metal-semiconductor interface, two distinct contacts can be formed, as shown in **Figure 1.8a**: Schottky contact and Ohmic contact. The band bending occurs due to the built-in electric field created at the interface. There is a large energy barrier Φ_B in the Schottky contact for electron transfer from metal to semiconductor, but this contact favors the electron flow from semiconductor to metal. On the contrary, electrons can conduct easily in both directions for Ohmic contact because of the small energy barrier. While for semiconductor-semiconductor configuration, three types of interfaces exist based on band alignment, as shown in **Figure 1.8b**: straddling gap (Type I), staggered gap (Type II) and broken gap (Type III) [90]. Note here, that band bending also occurs in semiconductor-semiconductor heterostructures, but it's not schematically shown in **Figure 1.8b** for simplicity.

After establishing the equilibrium condition, charge transfer can be further triggered by external stimuli, for example, photoexcitation. In semiconductor-semiconductor heterostructures, the photoexcited electrons will accumulate in the semiconductor with the

lowest conduction band minimum E_{CM}, while photoexcited holes will end up in the semiconductor with the highest valence band maximum E_{VM}. As in type I semiconductor-semiconductor heterostructure, electrons and holes all flow from the larger-bandgap semiconductor to the smaller-bandgap semiconductor; On the other hand, in type II and type III semiconductor-semiconductor heterostructures, electrons and holes are eventually separated in different semiconductors.

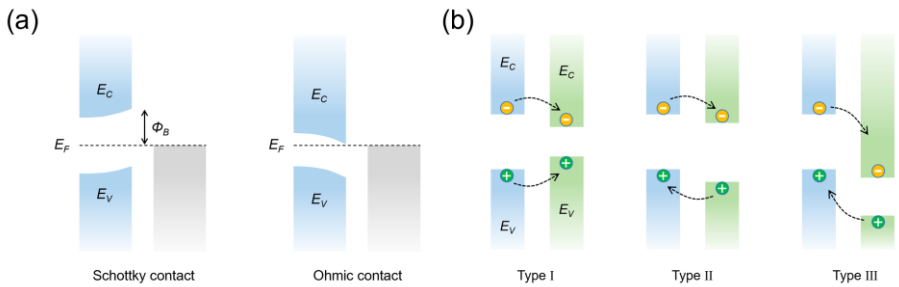

Figure 1.8 | The band alignments of different material contacts. Schematic illustration of band alignment for **(a)** metal-semiconductor contacts and **(b)** semiconductor-semiconductor heterostructures. The allowed charge transfer directions are also shown for three different types of band alignment.

1.3 Outline of this thesis

This thesis aims to explore and understand the fundamentals of photoinduced ultrafast charge carrier dynamics and charge transport in metal halide perovskites employing THz time-domain spectroscopy (THz-TDS). THz-TDS is a non-contact, all-optical spectrometer that enables the time-resolved and frequency-resolved photoconductivity measurements with sub-ps time resolution. These measurements could provide intrinsic material parameters, including carrier lifetime, charge mobility, phonon absorption, etc., that are extremely relevant for optoelectronic applications. The interrogation of the photophysics in metal halide perovskites could disclose the secrets behind their unique optoelectronic properties and pave the way for further optimization and innovation of PV devices. Below I briefly summarize the chapters in this thesis.

Chapter 1: We introduce the crystal structures and basic optoelectronic properties of metal halide perovskites, specifically focusing on the most studied hybrid organic-inorganic lead halide perovskites. Then we present the newly developed all-inorganic lead halide perovskite $CsPbI_3$ and double perovskite $Cs_2AgBiBr_6$, which are investigated in this thesis. The necessary fundamentals regarding the research works are provided in the following chapters.

Chapter 2: The experimental technique of THz-TDS is described, including the historical development, the theoretical principles of THz generation and detection, and the experimental setup utilized in this thesis. The approaches for extracting the photoconductivity and the

corresponding theoretical models are also presented.

Chapter 3: Here, we study photoinduced charge transport in all-inorganic black γ-phase LHP $CsPbI_3$. The measured photoconductivity spectra are consistent with the classical Drude model, which is a strong indication of band-like charge transport. In addition, temperature-dependent measurements reveal that large polaron formation governs charge carrier transport, following the Feynman polaron model. Furthermore, we extract the polaron mobility of up to 270 ± 44 $cm^2V^{-1}s^{-1}$, which is nearly one order of magnitude higher than that reported for hybrid organic-inorganic lead halide perovskites and approaches the theoretical limit for polarons scattering from longitudinal optical (LO) phonons.

Chapter 4: Establishing the polaron nature, we further study the photophysics in black γ-$CsPbI_3$ when the polaron density exceeds the so-called Mott polaron density. Above this density, the wavefunctions of large polarons start to overlap. By THz spectroscopy, we observe carrier density saturation effect after photoexcitations. This effect is also observed in $MAPbI_3$ and $CsPbBr_3$, demonstrating it is an intrinsic property of LHPs. We quantify experimentally this saturated density which agrees very well with the calculated Mott density based on the Feynman polaron model. The temperature-dependent measurement further supports the Mott polaron state formation. In addition, we reveal much-enhanced polaron-polaron scattering above the Mott density setting a strong limitation on the charge mobility, even though the polarons still follow delocalized band transport.

Chapter 5: Hot carrier dynamics is investigated in $Cs_2AgBiBr_6$ double perovskite. Following photo-excitation, hot carriers generated with excess energy exhibit boosted mobility, reaching a 4-fold enhancement compared to cold carriers at an excess energy of ~1.5 eV and a long-range hot-carrier transport length beyond 200 nm. By optical pump-IR push-THz probe spectroscopy and frequency-resolved photoconductivity measurements, we provide experimental evidence that the conductivity enhancement originates primarily from hot holes which experience reduced momentum scattering compared to their cold states. We rationalize our observation by considering (quasi-)ballistic transport of thermalized hot holes with energies above an energetic threshold in $Cs_2AgBiBr_6$.

Chapter 6: By constructing $Cs_2AgBiBr_6$ double perovskite/graphene heterostructure, we study the charge transfer dynamics at the interface. Upon photoexcitations with photon energy below the bandgap of double perovskite, we observe hole transfer from graphene to double perovskite; while with photon energy above the bandgap of double perovskite, there is hole transfer from double perovskite to graphene. In both cases, the transfer efficiency increases with photon energies.

2 THz spectroscopy

2.1 Introduction

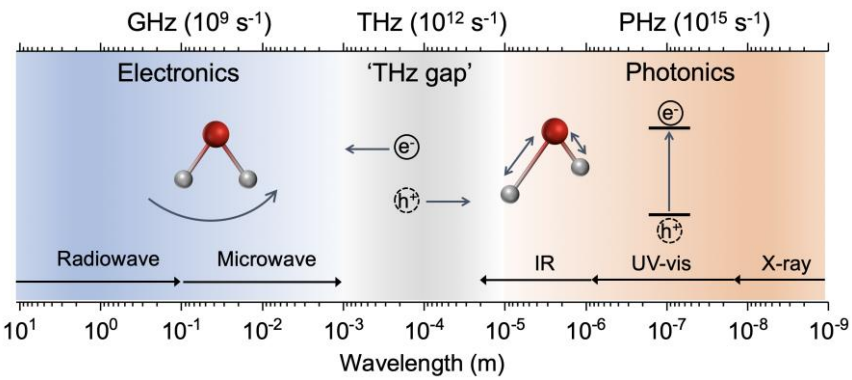

Figure 2.1 | The electromagnetic spectrum. Electromagnetic spectrum and corresponding typical electronic transitions in different frequency ranges, including molecular rotations and vibrations, intraband charge motion and interband transitions. Specifically, THz frequency range shown in shaded grey bridges the frequency spectrum of 'electronics' and 'photonics'.

THz radiation is a specific range of electromagnetic (EM) waves as shown in **Figure 2.1**, which covers typically from 10^{11} Hz to 10^{13} Hz, that is, 0.1 THz to 10 THz. The equivalent quantities corresponding to 1 THz are:

$$1\ \text{THz} = 10^{12}\ \text{Hz} = 0.3\ \text{mm} = 1\ \text{ps per cycle} = 4.1\ \text{meV} = 33\ \text{cm}^{-1} = 47.6\ \text{K}.$$

From the perspective of the wavelength, the THz radiation is also called submillimeter waves. The energy of THz radiation is very small (several to 10s of meV), so it matches well with many resonant transitions of fundamental excitations, for example, the motion of free carriers, phonons, excitons, plasmons and so on [91]. Therefore, THz waves can be used as noninvasive optical probes to investigate many material properties.

However, the application of THz waves has been challenging for a long time due to the lack of efficient and stable THz emitters and detectors. On one hand, the electronic devices that generate GHz and MHz waves are not sufficient to run at THz frequency. On the other hand, the THz photon energy is too low for electronic transitions that are often used for optical light generation. As a consequence, the THz radiation becomes a special and unexplored EM frequency range between 'electronics' and 'photonics'. Historically, this is the so-called 'THz

gap'.

The experimental investigation employing THz spectroscopy has not been possible until 1970s, when THz generation and detection techniques were developed. In 1971, Shen *et al.* produced 0.05-0.5 THz radiation by optical rectification of picosecond laser pulse in a nonlinear crystal $LiNbO_3$ [92]. This method is based on the non-resonant optical processes in which the difference frequency from an ultrashort laser pulse is generated in a nonlinear crystal. Following this approach, different crystals (e.g., ZnTe, GaP, GaSe) and shorter laser pulses are employed to extend the THz bandwidth [93,94]. In 1984, another method was developed by Auston and co-workers to generate and detect THz pulses, that is, photoconductive method [95]. In this method, an optical pulse is sent to the channel area of a semiconductor between two electrodes to generate free charge carriers, and then a voltage is applied between the electrodes generating a transient current that will radiate THz waves. The reversed process is utilized for THz detection: after the generation of free carriers by optical pulse, incident THz field will induce a transient current that is read out between the electrodes. By controlling the relative delay between optical pulse and THz pulse, the time-resolved THz waveform can be obtained. Yet, the detected THz bandwidth by this method is not only limited by the optical pulse duration, but also the scattering time, recombination lifetime and drift time of the photogenerated charge carriers in the semiconductors [91]. In 1996, Zhang *et al.* developed the free-space electrooptic sampling (FEOS) for detecting THz pulse utilizing the Pockels effect [96]. Different from photoconductive THz detection scheme, FEOS is based on nonlinear crystals in which the birefringence can be induced or changed by the incoming THz electric field. The birefringence variation in time is then tracked by a time-delayed sampling pulse. With this method, the time resolution is, in principle, only limited by the optical pulse duration, and thus large bandwidth can be obtained [91]. In this thesis, the THz generation and detection are based on optical rectification and free-space electrooptic sampling, respectively.

2.2 THz generation and detection

2.2.1 Maxwell's equations in a dielectric material and its solution

The electromagnetic wave generation and propagation in a medium without magnetization is governed by the Maxwell's equations:

$$\nabla \cdot \boldsymbol{E} = \frac{\rho}{\varepsilon_0} \tag{2.1}$$

$$\nabla \cdot \boldsymbol{B} = 0 \tag{2.2}$$

$$\nabla \times \boldsymbol{E} = -\frac{\partial \boldsymbol{B}}{\partial t} \tag{2.3}$$

$$\nabla \times \boldsymbol{B} = \mu_0 \varepsilon_0 \frac{\partial \boldsymbol{E}}{\partial t} + \mu_0 \boldsymbol{J} \tag{2.4}$$

where $\boldsymbol{E}$ is the electric field, $\boldsymbol{B}$ magnetic induction, ρ charge density, $\boldsymbol{J}$ current density, ε_0 vacuum permittivity, μ_0 vacuum permeability, t time. $\boldsymbol{E}$, $\boldsymbol{B}$, and $\boldsymbol{J}$ are all vectors.

In a medium, the total charge density ρ is a combination of externally added charges ρ_f (e.g., incoming current) and polarization-induced charges ρ_p: $\rho = \rho_f + \rho_p$. Here, ρ_p is related to polarization $\boldsymbol{P}$ following:

$$\rho_p = -\nabla \cdot \boldsymbol{P} \tag{2.5}$$

Similarly, the total current density $\boldsymbol{J}$ is composed of conduction current $\boldsymbol{J}_f$ and polarization-induced current $\boldsymbol{J}_p$: $\boldsymbol{J} = \boldsymbol{J}_f + \boldsymbol{J}_p$. And $\boldsymbol{J}_p$ can be expressed in terms of polarization:

$$\boldsymbol{J}_p = \frac{\partial \boldsymbol{P}}{\partial t} \tag{2.6}$$

Applying the identity $\nabla \times (\nabla \times \boldsymbol{E}) = \nabla \cdot (\nabla \cdot \boldsymbol{E}) - \nabla^2 \boldsymbol{E}$, and knowing $\nabla \cdot (\nabla \cdot \boldsymbol{E}) = 0$, we derive the following wave equation:

$$\nabla^2 \boldsymbol{E} - \frac{1}{c^2}\frac{\partial^2 \boldsymbol{E}}{\partial^2 t} = \mu_0 \left(\frac{\partial \boldsymbol{J}_f}{\partial t} + \frac{\partial^2 \boldsymbol{P}}{\partial^2 t} \right) \tag{2.7}$$

A far-field on-axis solution to the wave equation (2.7) is calculated approximately as [97,98,99,100]:

$$\boldsymbol{E}(t) \approx -\frac{\mu_0}{4\pi}\frac{S}{z}\left(\frac{\partial \boldsymbol{J}_f}{\partial t} + \frac{\partial^2 \boldsymbol{P}}{\partial^2 t} \right) \tag{2.8}$$

in which S is the radiation area, z is the distance from the emitting surface to the detector.

This solution indicates that the time-varying current density or polarization in a material can be used to generate propagating EM waves. Accordingly, two techniques are developed to generate THz EM wave: photoconductive switch based on time-varying current and optical rectification based on fast-changing polarization. As introduced above, THz generation by photoconductive switches is realized by accelerating the photoexcited charge carriers in a semiconductor under an externally applied or built-in electric field. Thus, a transient current is formed, which in turn emits EM waves. Since the far-field EM radiation is proportional to the first derivative of this transient current, the THz pulse duration depends strongly on the rise and fall time of the current. Therefore, the THz bandwidth in this method is limited by the optical pulse duration, the carrier scattering time, the drift time across the active emitting area, and, more importantly, the recombination time of photoexcited charge carriers [91]. In contrast, THz generation via optical rectification is a non-resonant second-order nonlinear process that relies only on the optical pulse duration.

2.2.2 Optical rectification

Polarization in matter $\boldsymbol{P}(\boldsymbol{k}, \omega)$ can be induced instantaneously by an external electric field $\boldsymbol{E}(\boldsymbol{k}, \omega)$ via dielectric susceptibility χ:

$$\boldsymbol{P}(\boldsymbol{k},\omega) = (\varepsilon - 1)\varepsilon_0 \cdot \boldsymbol{E}(\boldsymbol{k},\omega) = \chi \cdot \boldsymbol{E}(\boldsymbol{k},\omega) \quad (2.9)$$

where ε is relative dielectric function, $\boldsymbol{k}$ is the wave vector, ω is the angular frequency.

Expanding $\boldsymbol{P}(\boldsymbol{k},\omega)$ into the series as a power of $\boldsymbol{E}(\boldsymbol{k},\omega)$:

$$\boldsymbol{P}(\boldsymbol{k},\omega) = \boldsymbol{P}^{(1)}(\boldsymbol{k},\omega) + \boldsymbol{P}^{(2)}(\boldsymbol{k},\omega) + \boldsymbol{P}^{(3)}(\boldsymbol{k},\omega) + \cdots \quad (2.10)$$

with

$$\boldsymbol{P}^{(1)}(\omega) = \chi^{(1)} \cdot \boldsymbol{E}(\omega_i) \quad (2.11)$$

$$\boldsymbol{P}^{(2)}(\omega) = \chi^{(2)} \cdot \boldsymbol{E}(\omega_i)\boldsymbol{E}(\omega_j) \quad (2.12)$$

$$\boldsymbol{P}^{(3)}(\omega) = \chi^{(3)} \cdot \boldsymbol{E}(\omega_i)\boldsymbol{E}(\omega_j)\boldsymbol{E}(\omega_k) \quad (2.13)$$

Here, $\omega_{i,j,k}$ is the different frequency component in the applied electric field $\boldsymbol{E}(\boldsymbol{k},\omega)$. The above formulas indicate that the high-order nonlinear susceptibilities provide mixing of frequencies of different monochromatic waves.

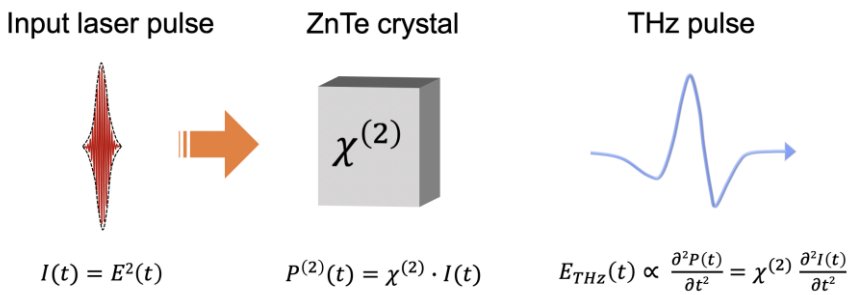

Figure 2.2 | THz generation by optical rectification. The short laser pulse induces second-order nonlinear polarization, which radiates THz waves.

Now we will focus ourselves on the second-order polarization term which results in the optical rectification upon photoexcitation as shown in **Figure 2.2**. Assuming there are two EM plane waves with electric field amplitudes of A_1, A_2 and frequencies of ω_1, ω_2: $E_1(t) = A_1(\mathrm{t})\cos(\omega_1 \cdot t)$ and $E_2(t) = A_2(\mathrm{t})\cos(\omega_2 \cdot t)$, the second-order polarization is then expressed as:

$$P^{(2)}(\omega,t) = \chi^{(2)}A_1(\mathrm{t})A_2(\mathrm{t})\cos(\omega_1 \cdot t)\cos(\omega_2 \cdot t) \quad (2.14)$$

Using the identities in the trigonometric functions, one obtains the following equation:

$$P^{(2)}(\omega,t) = \frac{1}{2}\chi^{(2)}A_1(\mathrm{t})A_2(\mathrm{t})\cos(\omega_1 + \omega_2)t + \frac{1}{2}\chi^{(2)}A_1(\mathrm{t})A_2(\mathrm{t})\cos(\omega_1 - \omega_2)t \quad (2.15)$$

Therefore, the second-order polarization contains two components with *sum* and *difference* frequencies. Furthermore, if the two plane waves are identical, that is, $A_1 = A_2 = A$ and $\omega_1 = \omega_2 = \omega$, then expression (2.15) is reduced to:

$$P^{(2)}(\omega,t) = \frac{1}{2}\chi^{(2)}A^2(t)\cos(2\omega)t + \frac{1}{2}\chi^{(2)}A^2(t) \quad (2.16)$$

Bring (2.16) back to solution (2.8), the far-field EM wave is obtained. The first term here has

a doubled carrier frequency of 2ω, so it can be used for *second harmonic generation (SHG)*. While the second term has no frequency dependence, it is suitable for *optical rectification (OR)*.

To achieve efficient OR, three basic requirements need to be fulfilled:

1) Modulated laser

According to solution (2.8), time-varying polarization is needed to generate EM waves. Since the polarization relies only on the envelope of the incoming laser pulse, modulated pulse with time-varying amplitudes is necessary.

2) Strong electric field

Higher-order nonlinear polarizations are often too weak to generate appreciable EM waves. The ratio of two successive polarization terms can be roughly approximated as:

$$\left|\frac{P^{(n+1)}}{P^{(n)}}\right| = \left|\frac{\chi^{(n+1)} \cdot E}{\chi^{(n)}}\right| \approx \left|\frac{E}{E_{mat}}\right| \tag{2.17}$$

Here, E_{mat} is the inherent electric field inside a material, which is typically on the order of 10^8 V/cm. For OR, the power scales to the square of laser intensity, and the power conversion efficiency is quite low, in the range of 10^{-6} - 10^{-3}. Therefore, a powerful laser with a strong electric field is required.

3) Non-centrosymmetric material

As higher-order polarization depends on incoming laser electric field, as well as higher-order susceptibility, the material symmetry needs to be considered. $\chi^{(n)}$ is a tensor, which correlates strongly with the internal symmetry of the material. For centrosymmetric material, for example, silicon, $\chi^{(2n)} = 0$ $(n = 1, 2, 3 \ldots)$. Therefore, non-centrosymmetric materials are required for optical rectification.

2.2.3 Free-space electrooptic sampling (FEOS)

THz detection utilized in this thesis is *free-space electrooptic (EO) sampling* which is based on *Pockels effect* or *linear electrooptic effect*. In Pockels effect, the refractive index of a medium can be modified linearly by the applied electric field [91]. This will induce or change the birefringence in a non-centrosymmetric EO crystal. In 1996, Zhang *et al.* made use of this effect and invented FEOS for THz detection [101]. In this method, the THz field-induced birefringence is probed by measuring the polarization change of another linearly polarized, co-propagating ultrashort optical pulse (i.e., sampling pulse). Because the polarization change is linearly proportional to the THz electric field, the time-domain THz waveform can thus be mapped out by varying the relative delay between the sampling pulse and the THz pulse via an optical delay line. The advantage of FEOS is that the time resolution is in principle only limited by the optical pulse duration [91].

Figure 2.3 shows the FEOS detection scheme used in our setup. We use <110>-orientated

zinc telluride (ZnTe) as EO crystal. ZnTe crystal has a cubic lattice, belonging to the $\bar{4}3m$ symmetry class. As a result, the refractive indices are the same in all directions in the absence of an external electric field. Now the linearly polarized sampling pulse will experience no polarization change after propagating through the ZnTe crystal. Through a quarter-waveplate, the sampling pulse become circularly polarized and is then separated by the Wollaston prism into two beams (I_s and I_p) with linear polarizations orthogonal to each other. These two components have the same electric field intensity which thus leads to no net current in the balanced photodiodes, that is, $\Delta I = I_s - I_p = 0$.

On the other hand, when THz pulse incidents upon the ZnTe crystal, the refractive indices of the crystal will be modulated to give rise to birefringence. Now the electric field components of the sampling pulse along fast and slow optical axes (with corresponding refractive indices of n_f and n_s) will experience phase retardation $\Delta\phi$. More specifically, this phase retardation can be mathematically expressed as following [102]:

$$\Delta\phi = \frac{\omega \cdot (n_f - n_s) \cdot d}{c} = \frac{1}{2}\frac{\omega \cdot n_0^3 \cdot r_{41} \cdot d \cdot E_{THz}}{c} \tag{2.18}$$

Here, $n_0 = 2.58$ is the refractive index of the ZnTe crystal without external electric field [103], $r_{41} = 4.1\ pm/V$ is the EO coefficient [104], d is the thickness of the ZnTe crystal, E_{THz} is the electric field of the incident THz pulse.

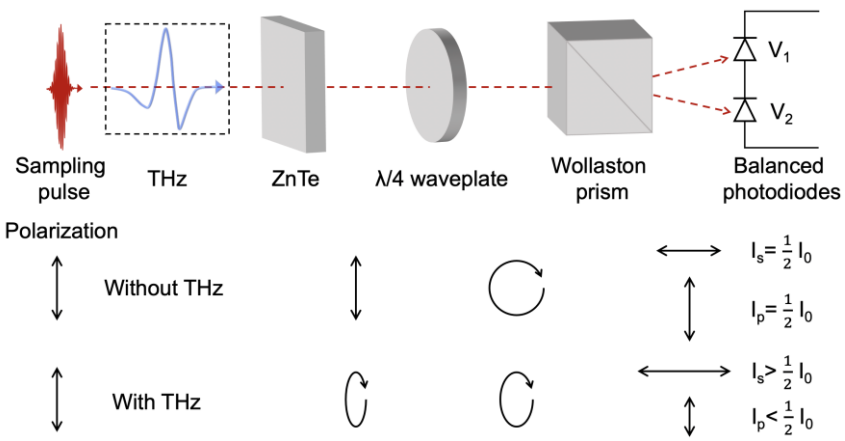

Figure 2.3 | THz detection by free-space electro-optic sampling. The optical elements required for EO sampling is shown above and the corresponding polarization states of the sampling pulse after each element are shown below for both conditions, that is, with and without THz illumination.

Due to the phase retardation, the linearly polarized sampling pulse will become elliptically polarized and now the separated two beams after the Wollaston prism have different intensities. Therefore, a net photocurrent is generated in the balanced photodiodes which can be read out by a lock-in amplifier. In the small-signal approximation, i.e., $\Delta\phi \ll 1$, the differential current

is proportional to the THz electric field $\Delta I = I_s - I_p \propto E_{THz}$ [105]. By varying the relative time delay between the THz pulse and the sampling pulse, the time-resolved photocurrent transient can be recorded, so that one obtains time-domain THz electric field. As the sampling pulse has a time duration of 10s fs which is much shorter than that of THz pulse of ~1 ps, the time resolution in FEOS is mainly limited by the sampling pulse duration. Yet, there are other factors that can influence the temporal and frequency resolution for EO sampling, e.g., the phase mismatch between phase velocity of THz pulse and group velocity of sampling pulse, the dispersion of the nonlinear susceptibility, the frequency dependence of the absorption and refractive index of the EO crystal.

2.3 Experimental setup

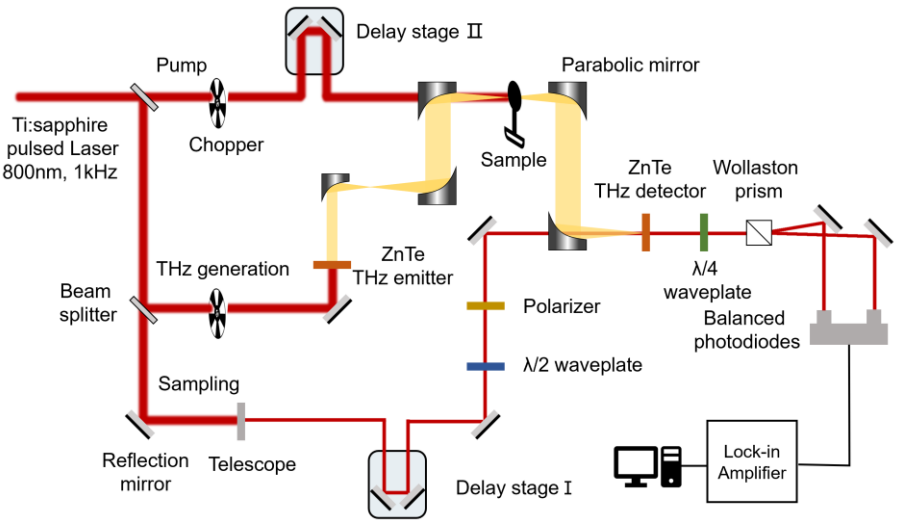

Figure 2.4 | Schematic illustration of the THz setup.

The THz spectroscopy setup used for the works in this thesis is driven by a commercial, regenerative amplified, mode-locked titanium-sapphire (Ti: sapphire) pulsed laser with 1 kHz repetition rate, 800 nm central wavelength and sub-100 fs pulse duration. The output laser is separated into three parts by beam splitters as shown in **Figure 2.4**, one for THz generation, one for sampling, and one for photoexciting the material of interest, i.e., pump.

The THz pulse is generated based on optical rectification by shedding 800 nm pulse on a 1 mm thick, <110>-orientated ZnTe crystal. ZnTe crystal is one of the most popular THz generators, due to both the large second-order nonlinear susceptibility ($\chi^{(2)} = 1.6 \times 10^{-7}\ esu$) and electrooptic coefficient ($r_{41} = 4.04\ pm/V$) at 800 nm. Besides, it has a large bandgap of 2.28 eV, which makes it transparent for 800 nm pump laser. After the THz generation, the

transmitted 800 nm beam through ZnTe is blocked by a thick polymeric foam. The generated THz pulse is then collected, collimated and eventually focused by 90° off-axis parabolic mirrors on the detecting medium. The investigated samples will be placed at the focus of THz pulse between two parabolic mirrors. Since the THz radiation is invisible to naked eyes, we use red light diodes to align the THz beam.

For THz detection, another ZnTe crystal is employed for free-space electro-optic sampling, as discussed in the last section. Once the THz pulse incidents upon the ZnTe crystal, its electric field induces birefringence. Now a weak 800 nm sampling pulse goes through a half waveplate and a polarizer, and then propagates collinearly through ZnTe crystal. The induced birefringence by THz electric field causes elliptical polarization of the initially linearly polarized sampling pulse. After a quarter waveplate and a Wollaston prism, the elliptically polarized sampling pulse is separated into two linearly polarized pulses. These two polarizations are orthogonal to each other. The intensity of two separated pulses is detected by a balanced photodiodes generating a differential voltage that is proportional to the transient THz electric field. This small voltage signal is filtered out and amplified by a Model 7270 DSP lock-in amplifier. To resolve the temporal profile of THz wave, the arrival of the sampling pulse at the ZnTe detecting crystal is delayed relative to the THz pulse by a motorized optical delay stage.

For studying the THz response of photoexcited materials, a pump pulse is utilized, the wavelength of which can be modulated by either beta-barium-borate (BBO) or optical parametric amplifier (OPA). The available wavelength ranges from deep ultraviolet (UV) to near-infrared (IR). To study the charge carrier dynamics, the pump delay relative to the THz pulse, i.e., the pump-probe delay time, is realized via another optical delay stage. In our setup, the pump pulse propagates collinearly with the THz pulse to impinge on the sample.

2.4 Extracting conductivity

There are three equivalent complex-valued parameters to characterize the electronic properties of a material of interest: conductivity $\tilde{\sigma}(\omega)$, refractive index $\tilde{n}(\omega)$, and permittivity $\tilde{\varepsilon}(\omega)$. All these three parameters are related as:

$$\tilde{\varepsilon}(\omega) = \tilde{n}^2(\omega) \tag{2.19}$$

$$\tilde{\sigma}(\omega) = -i \cdot (\tilde{\varepsilon}(\omega) - 1) \cdot \varepsilon_0 \cdot \omega \tag{2.20}$$

in which ω is the angular frequency, ε_0 is the vacuum permittivity, i is the imaginary unit. Therefore, these three quantities contain the same optoelectronic information. In this thesis, we primarily use the complex conductivity $\tilde{\sigma}(\omega)$ to describe the material response in the following THz spectroscopic studies. Depending on the different operation modes of THz spectroscopy, we are able to extract the static conductivity (without photoexcitation) and photoconductivity

(with photoexcitation).

2.4.1 THz time-domain spectroscopy (THz-TDS)

THz-TDS measures the THz transmission through the material of interest in the equilibrium condition, i.e., without photoexcitation. In a practical measurement, a thin film material is usually deposited on a fused silica substrate or sandwiched by front and back fused silica windows. To accurately derive the conductivity, one needs to take the substrates into account, i.e., measures the THz transmission through only pure substrates as the reference signal. As shown in **Figure 2.5**, we consider a general situation where the sample with a refractive index of $\tilde{n}_s$ is sandwiched between two dielectric windows with refractive indices of n_1 and n_2. The whole sample is surrounded by dry air or nitrogen ($n_0 = 1$). Now a THz pulse with an electric field $\widetilde{\boldsymbol{E}}_{\boldsymbol{0}}(\omega)$ is normally incident on the front window, and then the THz transmission $\widetilde{\boldsymbol{E}}_{\boldsymbol{sam}}(\omega)$ is described as:

$$\widetilde{\boldsymbol{E}}_{\boldsymbol{sam}}(\omega) = \widetilde{\boldsymbol{E}}_{\boldsymbol{0}}(\omega) \cdot t_{01} \cdot e^{i\cdot\omega\cdot n_1\cdot l_1/c} \cdot \tilde{t}_{1s} \cdot e^{i\cdot\omega\cdot\tilde{n}_s\cdot d/c} \cdot \tilde{t}_{s2} \cdot \widetilde{MR} \cdot e^{i\cdot\omega\cdot n_2\cdot l_2/c} \cdot t_{20} \quad (2.21)$$

For the reference signal:

$$\widetilde{\boldsymbol{E}}_{\boldsymbol{ref}}(\omega) = \widetilde{\boldsymbol{E}}_{\boldsymbol{0}}(\omega) \cdot t_{01} \cdot e^{i\cdot\omega\cdot n_1\cdot l_1/c} \cdot t_{1s} \cdot e^{i\cdot\omega\cdot d/c} \cdot t_{s2} \cdot e^{i\cdot\omega\cdot n_2\cdot l_2/c} \cdot t_{20} \quad (2.22)$$

Thereby the ratio of the sample signal to the reference signal reads as:

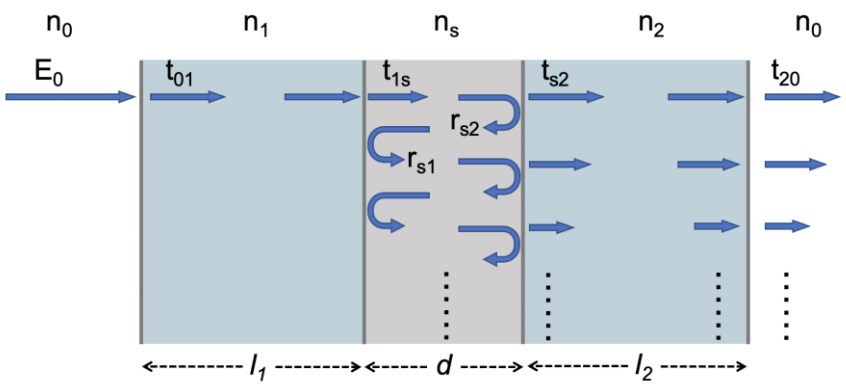

Figure 2.5 | THz transmission through thin films. For a general layout, the thin film with thickness of d is sandwiched between front and back dielectric windows with thicknesses of l_1 and l_2, respectively.

$$\tilde{\boldsymbol{T}}(\omega) = \frac{\widetilde{\boldsymbol{E}}_{\boldsymbol{sam}}(\omega)}{\widetilde{\boldsymbol{E}}_{\boldsymbol{ref}}(\omega)} = \frac{\tilde{t}_{1s} \cdot \tilde{t}_{s2}}{t_{1s} \cdot t_{s2}} \cdot e^{i\cdot\omega\cdot(\tilde{n}_s-1)\cdot d/c} \cdot \widetilde{MR} \quad (2.23)$$

$\widetilde{MR}$ is a factor if considering the multiple reflection within the thin film and given by:

$$\widetilde{MR} = \frac{1}{1 - \tilde{r}_{s1} \cdot \tilde{r}_{s2} \cdot e^{i\cdot 2\cdot\omega\cdot\tilde{n}_s\cdot d/c}} \quad (2.24)$$

Here, t_{xy} and r_{xy} are the Fresnel field transmission and reflection coefficients. More

specifically, for isotropic, homogeneous samples and dielectric windows with negligible magnetic properties, $\tilde{t}_{1s} = \frac{2 \cdot n_1}{n_1 + \tilde{n}_s}$, $\tilde{t}_{s2} = \frac{2 \cdot \tilde{n}_s}{n_2 + \tilde{n}_s}$, $t_{1s} = \frac{2 \cdot n_1}{n_1 + 1}$, $t_{s2} = \frac{2}{n_1 + 1}$, $\tilde{r}_{s1} = \frac{n_1 - \tilde{n}_s}{n_1 + \tilde{n}_s}$, $\tilde{r}_{s2} = \frac{n_2 - \tilde{n}_s}{n_2 + \tilde{n}_s}$.

Substituting with the above Fresnel coefficients, one gets:

$$\tilde{\boldsymbol{T}}(\omega) = \frac{(n_1 + 1) \cdot (n_2 + 1) \cdot \tilde{n}_s}{2 \cdot (n_1 + n_2) \cdot \tilde{n}_s \cdot cos\frac{\omega \cdot \tilde{n}_s \cdot d}{c} - i \cdot 2 \cdot (n_1 \cdot n_2 + \tilde{n}_s{}^2) \cdot sin\frac{\omega \cdot \tilde{n}_s \cdot d}{c}} \tag{2.25}$$

Very often, we deal with very thin conductive films with thickness of 10s to 100s of nm, even less in some cases, for example, single or few layers of two-dimensional materials. Therefore, two approximations can be made to simplify the data analysis:

1) Thin film approximation, that is, the thickness of the sample is much smaller than the THz wavelength: $\frac{d}{\lambda} \ll 1$, i.e., $\frac{\omega \cdot d}{c} \ll 1$. With this approximation, the equation is simplified to:

$$\tilde{\boldsymbol{T}}(\omega) \approx \frac{(n_1 + 1) \cdot (n_2 + 1)}{2 \cdot (n_1 + n_2) - i \cdot 2 \cdot \left(n_1 \cdot n_2 + \tilde{n}_s{}^2\right) \cdot \frac{\omega \cdot d}{c}} \tag{2.26}$$

2) Conductive approximation: $\tilde{n}_s \gg n_1$, $\tilde{n}_s \gg n_2$,

$$\tilde{\boldsymbol{T}}(\omega) \approx \frac{(n_1 + 1) \cdot (n_2 + 1)}{2 \cdot (n_1 + n_2) - i \cdot 2 \cdot \tilde{n}_s{}^2 \cdot \frac{\omega \cdot d}{c}} \tag{2.27}$$

In this thesis, the front window is usually the nitrogen, so $n_1 = 1$. For this special case, we extract the static conductivity $\sigma_0(\omega)$ as following:

$$\sigma_0(\omega) = \frac{1 + n_2}{Z_0 \cdot d} \cdot \left(\frac{1}{\tilde{\boldsymbol{T}}} - 1\right) \tag{2.28}$$

in which Z_0 represents the free space impedance ($Z_0 = \frac{1}{\varepsilon_0 \cdot c}$). This is the so-called Tinkham formula.

2.4.2 Optical pump - THz probe spectroscopy

What makes THz spectroscopy really powerful and unique in studying material properties is its pump-probe configuration. In this thesis, an optical pulse from ultraviolet (UV) to infrared (IR) is employed to pump the sample out of equilibrium, and then the THz pulse is sent propagating through the sample with a controlled pump-probe delay time t_P to probe the time-dependent photoconductivity. In consequence, this technique is often called optical pump - THz probe spectroscopy (OPTP). Benefitted from the high time resolution, OPTP is capable of detecting ultrafast carrier dynamics, including hot carrier thermalization and cooling, charge recombination, charge transfer in the heterostructures, and so on. Because of the coherent THz sampling approach, one can monitor the pump-induced THz transmission change by looking at one single point in the THz wave or scanning the whole THz pulse. Therefore, OPTP can be

classified into two different modes: 1D spectroscopy and 2D spectroscopy.

For 1D spectroscopy, one fixes the sampling pulse at a specific point in the THz waveform and then records its change as a function of pump-probe delay time t_P, in other words, the sampling delay stage is fixed while only the pump delay stage is moving. In such a way, one can easily obtain the time-resolved THz transmission change which can be related to the carrier dynamics.

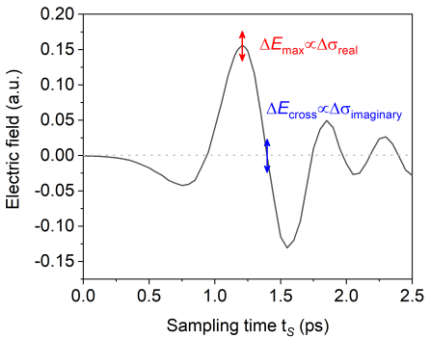

Figure 2.6 | Real and imaginary photoconductivity measurement in 1D OPTP configuration. When the sampling pulse is fixed at the THz peak (red arrow), the photoinduced modulation of the THz transmission scales linearly with the real part of the photoconductivity; While the imaginary part of the photoconductivity is given by measuring the change of the zero-crossing (blue arrow).

Depending on the exact sampling point in the THz wave, not only the THz intensity change but also the phase variance can be resolved in time as shown in **Figure 2.6**.

When the sampling pulse is fixed at the peak of the main THz pulse, one measures only the intensity change modulated by photoexcitation, i.e., the real part of photoconductivity. Note here, this method is valid only when the phase modulation or the refractive index change after photoexcitation is substantially small.

When the sampling pulse is fixed at the zero-crossing point, one measures primarily the phase change by photoexcitation, i.e., the imaginary part of photoconductivity. In the close vicinity of this crossing point, the THz electric field is linearly proportional to the phase modulation.

1D spectroscopy measures the frequency-averaged THz transmission change as a function of pump-probe delay time, so the frequency-dependent THz spectrum is missing, which is however very important and useful for obtaining intrinsic material properties. Besides, a 1D scan is not adequate and accurate when there is a large change of the refractive index in the photoresponse or transient THz pulse distortion [106]. For this purpose, 2D spectroscopy is established as a powerful tool to gain more information about the intrinsic charge transport properties. Instead of fixing the sampling pulse at one specific point in the THz waveform, one scans the whole THz pulse in time domain with respect to a fixed pump-probe delay time in 2D

spectroscopy. By recording the THz electric field before and after the photoexcitation, and then applying the Fourier Transformation, the frequency-resolved complex photoconductivity spectrum can be achieved at varied pump-probe delay times. However, intrinsic complications occur for data analysis when the change of carrier dynamics is comparable or even faster in time than the duration of the THz pulse [107]. In such a case, the different points in the THz wave 'see' different carrier dynamics, e.g., different carrier density or scattering events, if one simply fixes the pump delay stage and moves the sampling delay stage. Furthermore, there are issues at early pump-probe delay times when the pump pulse and THz pulse are partially overlap with each other. Now only the trailing end of the THz pulse will be modulated by photoexcitation [106]. To overcome this drawback, we move the delay stages for both pump and sampling simultaneously to keep the pump-sampling delay time fixed. As a result, the time resolution for 2D spectroscopy is limited only by sampling pulse (sub-100 fs), rather than by THz pulse duration (~1 ps). With such improved time resolution, many ultrafast change carrier dynamics can be investigated without complicated data deconvolution, for example, hot carrier cooling.

Similar to THz-TDS, one could derive the frequency-resolved photoconductivity based on the THz transmission before and after the photoexcitation. We still consider a sample configuration as shown in **Figure 2.5** in which the sample ($\tilde{n}_s$) is sandwiched between two dielectric windows (n_1 and n_2).

The THz transmission before photoexcitation is expressed:

$$\widetilde{\boldsymbol{E}}_{\boldsymbol{sam}}^{\boldsymbol{unpump}}(\omega) = \widetilde{\boldsymbol{E}}_{\boldsymbol{0}}(\omega) \cdot t_{01} \cdot e^{i\cdot\omega\cdot n_1\cdot l_1/c} \cdot \tilde{t}_{1s} \cdot e^{i\cdot\omega\cdot\tilde{n}_s\cdot d/c} \cdot \tilde{t}_{s2} \cdot \widetilde{MR} \cdot e^{i\cdot\omega\cdot n_2\cdot l_2/c} \cdot t_{20} \quad (2.29)$$

The THz transmission after photoexcitation is expressed with a dielectric function $\tilde{n}_s^*$:

$$\widetilde{\boldsymbol{E}}_{\boldsymbol{sam}}^{\boldsymbol{pump}}(\omega) = \widetilde{\boldsymbol{E}}_{\boldsymbol{0}}(\omega) \cdot t_{01} \cdot e^{i\cdot\omega\cdot n_1\cdot l_1/c} \cdot \tilde{t}_{1s}^* \cdot e^{i\cdot\omega\cdot\tilde{n}_s^*\cdot d/c} \cdot \tilde{t}_{s2}^* \cdot \widetilde{MR}^* \cdot e^{i\cdot\omega\cdot n_2\cdot l_2/c} \cdot t_{20} \quad (2.30)$$

And the THz transmission and reflection through the front and back surfaces of the sample are now changed to: $\tilde{t}_{1s} = \frac{2\cdot n_1}{n_1+\tilde{n}_s^*}$, $\tilde{t}_{s2} = \frac{2\cdot\tilde{n}_s^*}{n_2+\tilde{n}_s^*}$, $\tilde{r}_{s1} = \frac{n_1-\tilde{n}_s^*}{n_1+\tilde{n}_s^*}$, $\tilde{r}_{s2} = \frac{n_2-\tilde{n}_s^*}{n_2+\tilde{n}_s^*}$.

So, the ratio of the THz transmission through pumped and unpumped sample reads as:

$$\widetilde{\boldsymbol{T}}^*(\omega) = \frac{\widetilde{\boldsymbol{E}}_{\boldsymbol{sam}}^{\boldsymbol{pump}}(\omega)}{\widetilde{\boldsymbol{E}}_{\boldsymbol{sam}}^{\boldsymbol{unpump}}(\omega)} = \frac{\tilde{t}_{1s}^* \cdot \tilde{t}_{s2}^* \cdot \widetilde{MR}^*}{\tilde{t}_{1s} \cdot \tilde{t}_{s2} \cdot \widetilde{MR}} \cdot e^{i\cdot\omega\cdot(\Delta\tilde{n})\cdot d/c} \quad (2.31)$$

Here, $\Delta\tilde{n} = \tilde{n}_s^* - \tilde{n}_s$.

Applying the following approximations:

1) Thin-film approximation: $\frac{d}{\lambda} \ll 1$;
2) Weak optical absorption: $\alpha d \ll 1$, α is the absorption coefficient;

The photoconductivity $\Delta\sigma(=\sigma-\sigma_0)$ can be derived as [108]:

$$\Delta\sigma(\omega) = -\frac{n_1+n_2}{Z_0\cdot d}\cdot\frac{\Delta\widetilde{\boldsymbol{E}}(\omega)}{\widetilde{\boldsymbol{E}}_{\boldsymbol{sam}}^{\boldsymbol{unpump}}(\omega)} \quad (2.32)$$

in which $\Delta\widetilde{\boldsymbol{E}}(\omega) = \widetilde{\boldsymbol{E}}_{\boldsymbol{sam}}^{\boldsymbol{pump}}(\omega) - \widetilde{\boldsymbol{E}}_{\boldsymbol{sam}}^{\boldsymbol{unpump}}(\omega)$.

For the intrinsic or slightly doped semiconductors, e.g., the perovskites investigated in this thesis, the static conductivity σ_0 (the conductivity before the pump) is negligible, i.e., $\sigma \gg \sigma_0$. Therefore, $\Delta\sigma$ can be approximated to be equal to σ.

2.5 Conductivity models

The THz conductivity spectrum can vary drastically according to the properties of the materials of interest. To gain more insights into the charge transport properties, many theoretical models have been developed to describe the various conductivity spectrum from different materials.

2.5.1 Drude model

In many inorganic bulk materials, the photoexcited or doped charge carriers behave like free particle gas, the conductivity spectrum of which can be well described by the Drude model [109,110]. The Drude model was developed in 1900 based on the kinetic theory for gases and applied to explain the electrical conduction in materials, especially in metals [111,112]. It contains only one free intrinsic parameter, scattering time. Though its simplicity, it has been verified over a large spectral range from MHz to THz [113].

To derive the Drude response, several assumptions are made:

1) In the absence of the external electric field, the charge carriers scatter randomly with crystal lattice (i.e., phonon), defects, other charge carriers and so on, so that there is no direction-preferential charge transport. The ensemble charge scattering effect is represented by a mean scattering time τ which is the average time between two consecutive collision events;
2) Once a collision occurs, the charges lose their momentum completely, i.e., $\boldsymbol{P} = 0$;
3) In the presence of a DC or AC electric field, between two collision events, the charges will be accelerated following Lorentz force and damped by various scattering events as mentioned above.

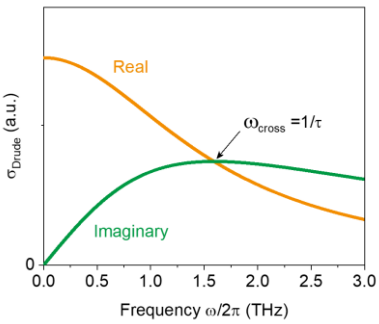

Figure 2.7 | The complex conductivity spectrum in the Drude model. ω_{cross} represents the angular frequency at which the real and imaginary parts of the Drude response cross each other. This frequency is the inverse of the scattering time.

From the scattering time, one obtains the scattering probability for a free charge carrier within a time interval dt: $\frac{dt}{\tau}$, therefore, the non-scattering probability is: $(1-\frac{dt}{\tau})$.

Assuming there is a charge carrier with momentum $\boldsymbol{P}(t)$ at time t. According to Newton's law $d\boldsymbol{P} = \boldsymbol{F}\cdot dt$ and momentum conservation, the charge momentum after dt between two collisions reads as: $\boldsymbol{P}(t+dt) = \boldsymbol{P}(t) + \boldsymbol{F}\cdot dt$. Considering the scattering probability, the average momentum after dt follows: $\langle \boldsymbol{P}(t+dt)\rangle = \left(1-\frac{dt}{\tau}\right)(\boldsymbol{P}(t)+\boldsymbol{F}\cdot dt) + \frac{dt}{\tau}\cdot 0$. Expanding the right side of the equation and keeping the terms to the first order in dt, one gets:

$$\frac{d\boldsymbol{P}(t)}{dt} = \boldsymbol{F} - \frac{\boldsymbol{P}(t)}{\tau} \tag{2.33}$$

In the presence of an alternating electric field $\boldsymbol{E}(t) = \boldsymbol{E}_0\cdot e^{-i\omega t}$ with angular frequency ω and applying Ohm's law $\boldsymbol{j}(t) = \sigma\cdot\boldsymbol{E}(t)$ to the above Equation (2.33), one finally derives the expression for frequency-resolved conductivity, i.e., Drude model:

$$\sigma(\omega) = \frac{\omega_p^2\varepsilon_0\tau}{1-i\omega\tau} \tag{2.34}$$

Here, ω_p is plasma frequency and has a form of $\omega_p = \sqrt{\frac{e^2\cdot n}{\varepsilon_0\cdot m^*}}$ in which n is the carrier density, m^* is the effective mass, ε_0 is the vacuum permittivity, e is the elementary charge.

Figure 2.7 shows a typical complex Drude response dispersion within 3 THz, in which both real and imaginary parts are positive. From the expression (2.34), Drude model contains two free parameters: scattering time τ and plasma frequency ω_p. By fitting this equation to the measured complex THz conductivity, one can easily extract these two parameters. The scattering time happens to be the inverse of angular frequency at the cross point of real and imaginary parts. If the effective mass is known, one can calculate the charge mobility in the DC limit according to $\mu = \frac{e\cdot\tau}{m^*}$.

2.5.2 Drude-Smith model

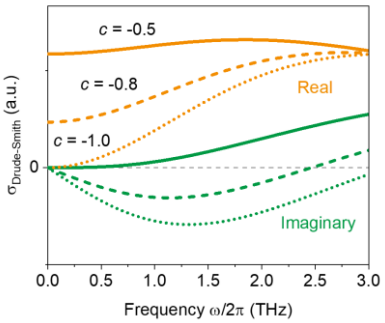

Figure 2.8 | The complex conductivity spectrum in the Drude-smith model. Three conditions are plotted here as examples for c = -0.5 (solid lines), c = -0.8 (dashed lines), c = -1.0 (dotted lines).

In many materials with reduced sizes to the mesoscopic scale, the free carrier response strongly deviates from the Drude model, for example, graphene nanoribbons, nanoparticles and nanowires [114,115]. In these materials, the low-frequency conductivity is suppressed to some extent or completely. This arises from the much-reduced crystalline size, which is now smaller than the mean free path of charge carriers. In this case, the charge momentum scattering is no longer randomized, leading to the breakdown of the Drude model.

To account for such charge confinement, a modified version of the Drude model, the Drude-Smith (DS) model, was developed [116]:

$$\sigma(\omega) = \frac{\omega_p^2 \varepsilon_0 \tau_{DS}}{1 - i\omega\tau_{DS}} \left(1 + \frac{c}{1 - i\omega\tau_{DS}}\right) \tag{2.35}$$

This model introduced another parameter c which is sometimes referred to as 'localization parameter'. c is defined only from -1 to 0. For $c = 0$, the DS model reverts back to the Drude model. While for $c = -1$, the DC conductivity is completely suppressed to 0, as shown in **Figure 2.8**, meaning there is no long-range charge transport. The charge carriers are strongly confined within a certain domain. Please note that the charge scattering time here can be different from that in the Drude model, referred to as DS scattering time τ_{DS} [117].

2.5.3 Lorentz model

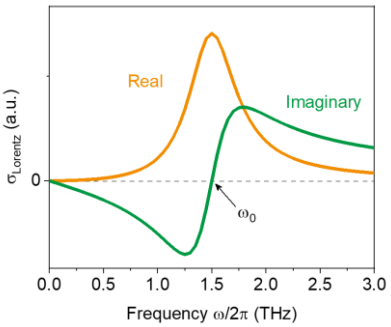

Figure 2.9 | The complex conductivity spectrum in the Lorentz model. ω_0 represents the resonant frequency of an oscillator.

In addition to the free carriers, many materials contain strongly correlated charge carriers, which can form quasi-particles, for instance, excitons. Especially nowadays, with the emergence of low dimensional semiconductors, e.g., 2D transition metal dichalcogenides (TMDs), quantum dots, and layered perovskites, the charge species are present as excitons, even at room temperature. To describe the oscillator-like quasiparticles, the Lorentz model has been developed.

For an electron that is bound to a hole as dipoles, the equation of its motion can be expressed as follows for an applied external electric field $\boldsymbol{E}(t) = \boldsymbol{E}_0 \cdot e^{-i\omega t}$:

$$m\frac{\partial^2 \boldsymbol{r}}{\partial t^2} + m\Gamma\frac{\partial \boldsymbol{r}}{\partial t} + m\omega_0^2 \boldsymbol{r} = -e\boldsymbol{E} \tag{2.36}$$

Here, Γ is the damping rate, ω_0 is the resonance frequency, m is the electron mass.

Applying the Fourier transformation to the above equation, the displacement $\boldsymbol{r}$ is solved:

$$\boldsymbol{r}(\omega) = -\frac{e}{m}\cdot\frac{\boldsymbol{E}}{\omega_0^2 - \omega^2 - i\omega\Gamma} \tag{2.37}$$

Subsequently, the dipole moment $\boldsymbol{\mu}(\omega)$ and polarization $\boldsymbol{P}(\omega)$ read as:

$$\boldsymbol{\mu}(\omega) = -e\cdot\boldsymbol{r}(\omega) = \frac{e^2}{m}\cdot\frac{\boldsymbol{E}}{\omega_0^2 - \omega^2 - i\omega\Gamma} \tag{2.38}$$

$$\boldsymbol{P}(\omega) = n\cdot\langle\boldsymbol{\mu}(\omega)\rangle = \frac{ne^2}{m}\cdot\frac{\boldsymbol{E}}{\omega_0^2 - \omega^2 - i\omega\Gamma} \tag{2.39}$$

in which n is the dipole density, $\langle\boldsymbol{\mu}(\omega)\rangle$

Since $\boldsymbol{P}(\omega) = \varepsilon_0\chi\boldsymbol{E}$, one extracts the susceptibility $\chi(\omega)$ and then the dielectric function $\varepsilon(\omega)$:

$$\varepsilon(\omega) = 1 + \chi(\omega) = 1 + \frac{\omega_p^2}{\omega_0^2 - \omega^2 - i\omega\Gamma} \tag{2.40}$$

The plasma frequency is defined just like that in the Drude model: $\omega_p = \sqrt{\frac{e^2 \cdot n}{\varepsilon_0 \cdot m}}$.

According to Equation (2.20), the corresponding conductivity is:

$$\sigma(\omega) = \frac{\omega_p^2 \varepsilon_0 \omega}{i(\omega_0^2 - \omega^2) + \omega\Gamma} \tag{2.41}$$

Figure 2.9 shows a typical Lorentz response in the THz window with a finite resonance frequency. From this resonance frequency, one can estimate the binding energy of the excitons or the phonon frequency in the case of phonon absorption.

3 Highly mobile large polarons in black phase $CsPbI_3$

We report the band-like transport of photogenerated charge carriers within all-inorganic black γ-phase $CsPbI_3$ (γ-$CsPbI_3$) thin films, with local mobilities up to 270 ± 44 $cm^2V^{-1}s^{-1}$ recorded using THz spectroscopy at room temperature. Temperature-dependent, high-frequency photoconductivity measurements indicate that large polaron formation governs charge carrier transport, following the Feynman polaron model. The mobility values derived using THz spectroscopy are nearly one order of magnitude higher than that reported for hybrid organic-inorganic lead halide perovskites and approach the theoretical limit for polarons scattering from longitudinal optical (LO) phonons. Our results identify γ-$CsPbI_3$ as a fascinating all-inorganic perovskite semiconductor with high charge carrier mobility for optoelectronics and reveal the effect of polaron formation on charge transport properties.

3.1 Introduction

Low-cost, solution-processable lead halide perovskites (LHPs) have attracted tremendous attention in recent years owing to their superior photovoltaic performance with the reported single-junction solar cell power conversion efficiency beyond 25% [118]. Such high photovoltaic efficiency originates from the excellent optoelectronic properties of LHPs, including high absorption coefficients [35], large carrier diffusion lengths [40,41], and inherent defect tolerance [32,119].

Despite their great promise, the volatility of organic cations in organic-inorganic hybrid LHPs (e.g., $APbX_3$ with A = methylammonium (MA) or formamidinium (FA), with X = Cl, Br or I) imposes severe thermal and chemical instability, which impedes the practical realization of hybrid LHPs-based applications [53,120,121,122]. Within this context, cesium-based all-inorganic LHPs (e.g., $CsPbX_3$) are promising alternatives for efficient photovoltaics with improved chemical stability [53,123,124]. In particular, the optically active black phase of $CsPbI_3$ possesses both a solar-friendly bandgap (~1.7 eV) and strong optical absorption in the UV-vis regime, holding great promise for the development of efficient all-inorganic perovskite photovoltaics [125]. Despite the high chemical stability, the black phase $CsPbI_3$ perovskite is thermodynamically unstable at room temperature (RT), energetically preferring the formation of its optically inactive yellow phase. Concerted efforts have been made to stabilize the black phase at RT [53,126,127,128,129,130], yet its photophysical details remain largely unexplored.

3.1 Introduction

Initial optical studies focused on understanding the evolution of charge carriers (charge separation and recombination, carrier multiplication, *etc.*) on the picosecond (ps) time scale following photoexcitation [131,132,133,134]. While the inferred carrier lifetimes in these reports are of great interest for developing efficient devices, the charge transport properties, such as the mobility of photogenerated carriers, a vital figure of merit for photovoltaic applications, are yet to be revealed.

Due to the "soft" and polar nature of lead halide perovskite crystals, photogenerated charge carriers have been shown to polarize the lattice and induce atomic displacement of the ions from their equilibrium positions [72,135]. The charge carriers, together with the associated local lattice deformation, can be described as a polaron quasi-particle [136]. Several recent experiments have provided spectroscopic evidence of polaron formation in perovskites [74,75,137,138,139,140,141], by, e.g., probing sub-ps lattice or vibrational dynamics. Polaron formation has been reported to be responsible for several of the fascinating optoelectronic properties in LHPs, including long-lived hot carriers and slow carrier recombination processes [44,63]. Exploring the influence of polaron formation on the photogenerated charge carrier transport will be essential for fundamentally understanding $CsPbI_3$-based optical device design and function.

Here, we report on the temperature-dependent transport properties of photogenerated charge carriers in γ-$CsPbI_3$ thin films employing ultrafast terahertz spectroscopy. The remarkably high charge carrier mobility in γ-$CsPbI_3$ of ~270 ± 44 $cm^2V^{-1}s^{-1}$ at room temperature approaches the theoretical limit, based on the Feynman polaron model of charge-LO phonon interaction. This result indicates that grain boundaries and defects do not play critical roles in determining the charge mobility in our samples. As such, we expect the mobility reported here for a polycrystalline sample to be that in single γ-$CsPbI_3$ crystals. Furthermore, this value is almost an order of magnitude higher than that for hybrid LHPs.

3.2 Materials

Black phase $CsPbI_3$ preparation

The CsI and PbI_2 precursor agents were dried for 12 h in the vacuum oven at 60 °C to remove all traces of water. A 0.2 M perovskite precursor solution was prepared by dissolving an equimolar ratio of CsI (99.9%; Sigma-Aldrich) and PbI_2 (99%; Sigma-Aldrich) in extra dry N,N-dimethylformamide (DMF). The yellow precursor solution was filtered by a 0.45 μm PTFE filter and spin-coated onto a 5×5 mm^2 fused silica substrate at 2000 rpm for 30 s and 3000 rpm for 60 s in a nitrogen glove box. The substrate was then transferred onto a hotplate for annealing at 160 °C for 60 s, yielding a $CsPbI_3$ thin film with a thickness of ~200 nm.

The $CsPbI_3$ black phase was accessed through thermal annealing of the $CsPbI_3$ thin film at

330 °C by using a Linkam stage, followed by immediate thermal quenching of the film by quickly transferring the substrate to a cold metal slab. This rapid cooling procedure allowed to achieve a room temperature stable black γ-phase by kinetically trapping the thin film [53]. The γ-$CsPbI_3$ persists at RT long enough to finalize the reported spectroscopic study when maintained under a nitrogen atmosphere or under vacuum conditions – supported by stable photoconductivity properties.

3.3 Results and Discussion

Comparison of optical absorption and photoconductivity dynamics of black and yellow phase $CsPbI_3$

A schematic illustration of the orthorhombic crystal structure of the γ-$CsPbI_3$ is shown in **Figure 3.1a**. The RT UV-vis absorption spectra of the same sample before (yellow phase) and after (black γ-phase) the thermal-driven phase transition are shown in **Figure 3.1b**. Compared to the yellow phase, the γ-$CsPbI_3$ exhibits much stronger absorption across the UV-vis spectrum with a direct bandgap around the expected 1.75 eV (**Figure 3.A.1** in the Appendix).

To investigate the dynamics and transport properties of photogenerated carriers in polycrystalline γ-$CsPbI_3$ thin films, we employed ultrafast optical pump-THz probe spectroscopy. In the OPTP measurement, a 400 nm laser pulse is used as pump to promote electrons from the valence to the conduction band. The photoconductivity is calculated based on Equation (2.32). Here in this work, n_1 and n_2 are 1 and 1.95 for vacuum and fused silica, respectively. The film thickness is ~200 nm.

In **Figure 3.1c,** the photoconductivity dynamics at the same absorbed photon density are compared for yellow phase and γ-$CsPbI_3$ thin films. The photoconductivity rise in γ-$CsPbI_3$ in the first 2-3 ps is attributed to hot carrier cooling [142]. Relative to the yellow phase, the charge carriers in the black phase possess a much longer lifetime (ns *vs.* sub-ps, see **Figures 3.1c and 3.1d**) and a ~50 times higher peak conductivity. The yellow phase's fast photoconductivity decay is assigned to ultrafast charge trapping due to the high defect density. This high defect density may be partially responsible for the low photoconductivity of yellow phase $CsPbI_3$. The comparative study demonstrates the superior photophysical and charge transport properties of γ-$CsPbI_3$ and its suitability for photovoltaics. The data in **Figure 3.1d** were recorded at sufficiently low excitation fluence to avoid higher-order recombination effects. Detailed fluence-dependent results (**Figure 3.A.2**) and analysis can be found in the Appendix, including the corresponding charge recombination fitting by the rate equation and a comparison of the rate constants with previous reports. Based on the analysis (see **Section 3.A.2 and 3.A.3**), we find that the mono-molecular trapping rate is enhanced (~40 times higher) compared to $MAPbI_3$ samples reported by Herz [39]. This indicates a relatively high defect density present in our

samples.

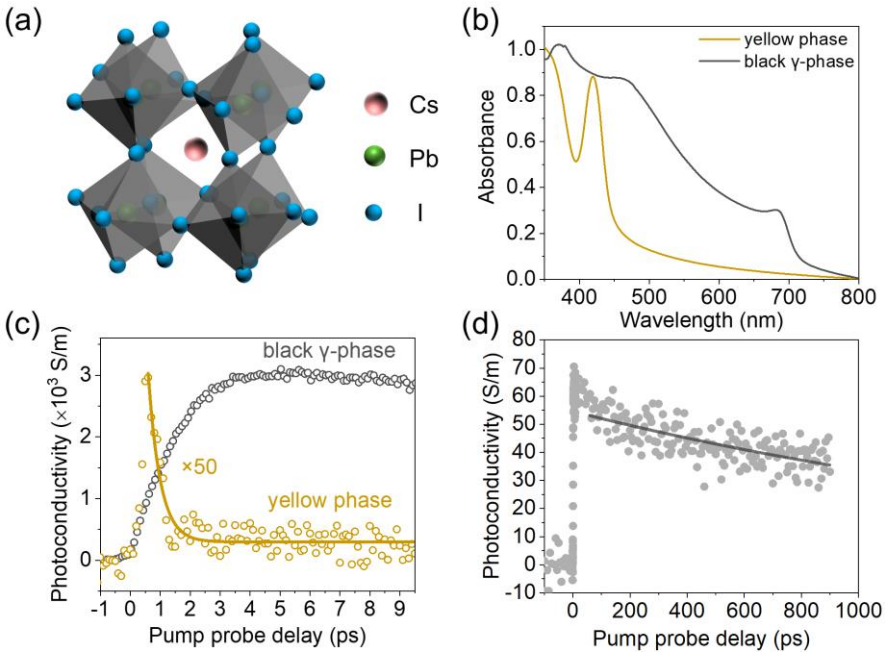

Figure 3.1 | Optical absorption and photoconductivity dynamics of yellow phase and γ-$CsPbI_3$. (a) Schematic representation of the black γ-$CsPbI_3$ crystal structure; **(b)** Absorption spectra of yellow phase and γ-$CsPbI_3$; **(c)** THz photoconductivity comparison for γ-$CsPbI_3$ and yellow phase at the same absorbed photon density of 5.81×10^{13} cm^{-2}. The solid line represents a single exponential fit with an offset; **(d)** photoconductivity dynamics of γ-$CsPbI_3$ at the absorbed photon density of 1.67×10^{12} cm^{-2}. The solid line is an exponential fit that yields a decay time of ~2 ns.

Extracting Drude scattering time from photoconductivity spectra of γ-$CsPbI_3$

To determine the charge carrier mobility, an important figure of merit within photovoltaic devices, we conduct a time-domain spectroscopic analysis for the γ-$CsPbI_3$ thin film at a given pump-probe delay time. TDS provides frequency-resolved complex conductivity spectra as exemplarily shown in **Figure 3.2a**, 4 ps, 124 ps, 524 ps after photoexcitation.

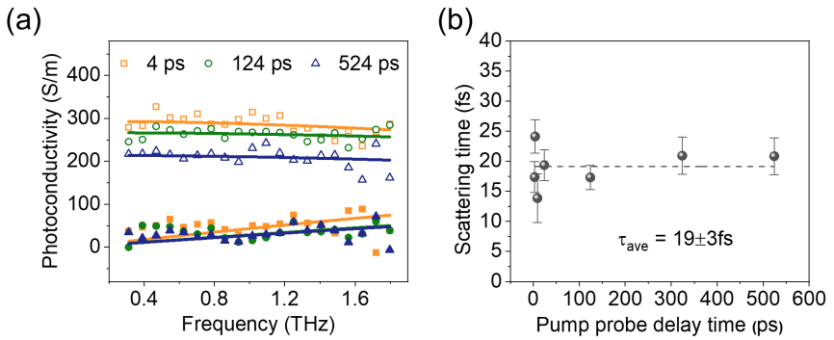

Figure 3.2 | Frequency-resolved photoconductivity of black γ-$CsPbI_3$. (a) Real (open symbols) and imaginary (solid symbols) components of the THz frequency-domain conductivity measured 4 ps, 124 ps, 524 ps after photoexcitation with a photon density of 5.9×10^{12} cm^{-2} at RT in vacuum. The solid lines represent Drude model fits; **(b)** Scattering times measured at different pump-probe time delays. The dashed line is the average of all scattering times.

Both the real and imaginary parts are positive and show negative and positive dispersion within the 0.25-1.8 THz bandwidth of the THz pulse, respectively. The Drude model (lines in **Figure 3.2a**) provides a quantitative description of the data. From the good agreement, we infer the mean charge scattering time τ_s to be 19 ± 3 fs based on measurements spanning time delays from 3 to ~550 ps, as shown in **Figure 3.2b**. Remarkably, despite the relatively high defect density (manifested by the large first-order recombination constant k_1, see Appendix), the obtained charge scattering time in black phase $CsPbI_3$ is found to be ~5 times longer than that in hybrid LHP samples with the same polycrystalline nature in the film as our γ-$CsPbI_3$. For example, a scattering time of 4 ± 0.5 fs in $MAPbI_3$ films has been reported previously [143].

Temperature-dependence of carrier mobility in γ-$CsPbI_3$

To gain additional insight into the charge carrier transport, we conducted temperature (T) dependent THz conductivity measurements between 77 K and RT. Previous THz-based measurements on hybrid perovskites found a $T^{-1.5}$ dependence of the mobility, which was interpreted by free electron-acoustic phonon scattering [143,144,145,146]. Meanwhile, the formation of large polarons (i.e., with lattice distortion beyond several lattice constants), has shown to occur on sub-ps time scales in all-inorganic perovskites, including $CsPbI_3$ [142,147]. Large polarons undergo band-like transport, with the mobility decreasing with increasing temperature, i.e., $d\mu/dT < 0$. Frost [72] has calculated the charge mobility in perovskites, including all-inorganic $CsPbI_3$, based on the Feynman polaron model, assuming the dominant role of LO phonon scattering for polaron transport. In addition, the polaron mobility is found to increase nonlinearly with lowering T. For the T range studied here, Frost predicts that: $\mu \propto T^{-\beta}$, with $\beta \sim 0.5$ [72].

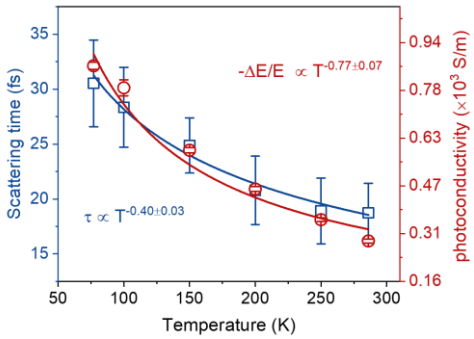

Figure 3.3 | Temperature-dependent scattering time and photoconductivity (proportional to $-\Delta E/E$). In this study, the incident photon density and wavelength for the optical excitation pulse is fixed (5.9×10^{12} cm^{-2} for 400 nm excitation). The solid lines are power-law fits.

As shown in **Figure 3.3**, we present both the photoconductivity of charge carriers based on the OPTP study, and the charge scattering time extracted from the Drude model, as a function of temperature. The general trend for both parameters is consistent with the transport of large polarons. For the experimental data in **Figure 3.3**, we find $\beta \sim 0.40$ for the scattering time and $\beta \sim 0.77$ for the photoconductivity. This reasonable agreement between our experimental results and theoretical predictions supports the notion of large polaron transport, limited by polaron-LO phonon scattering in γ-$CsPbI_3$. The large polaron formation can also explain the observed high defect tolerance in our sample [44,63].

Quantifying the polaron mobility in γ-$CsPbI_3$

To quantify the charge carrier mobility, μ, from the scattering time using the relation $\mu = \frac{e\tau_s}{m^*}$, we need knowledge of the effective mass of the photogenerated charge carriers m^*. This can be obtained from band structure calculations, but other renormalization factors, e.g., polaron formation need to be considered. Large polarons can exhibit band-like transport with an increased effective mass, m^*, relative to the bare band mass, m_b^*, of the solids, following Equation (1.8). To calculate the polaron effective mass, the electron-phonon coupling constant α needs to be first determined. Notably, previous theoretical calculations have reported very similar properties for α- and γ-black phases in terms of electronic structure and electron-phonon coupling strength [148,149]. Therefore, here we estimate the Fröhlich electron-phonon coupling constant α of the γ-phase, using the widely reported dielectric properties and vibrational modes of the α-phase (ε_{opt} = 6.1 ε_0, ε_s = 18.1 ε_0, ω_{LO} = 16.15 THz, respectively), based on theoretical studies [72]. These values are in line with previously reported experimental results for black phase $CsPbI_3$ [150,151]. We calculate α to be 1.23. The small value of α is consistent with the formation of large polarons ($\alpha < 6$) in the γ-$CsPbI_3$ as well [152]. Using

the band effective mass, m_b^*, from DFT calculations (~0.1 m_0, in which m_0 is the rest mass of an electron [149,153]), m^* is calculated to be 0.124 m_0 [154]. With this value, the charge carrier mobility amounts to ~270 ± 44 $cm^2V^{-1}s^{-1}$, which is nearly an order of magnitude higher than other hybrid LHPs polycrystalline thin films, as summarized in **Table 3.1**. The high mobility of the large polaron originates primarily from the long charge scattering time. Previous theoretical studies by Zheng *et al.* revealed that dynamic disorder caused by the organic cations can cause localization of charge carriers and thus reduce the mobility of large polarons in LHPs [135]. Our observation of a substantial enhancement in charge carrier mobility in all-inorganic perovskites compared to their organic-inorganic hybrid counterparts supports this conclusion. Furthermore, based on the lifetime inferred from the dynamics and the estimated mobility, the diffusion length of photogenerated polarons exceeds 1 μm (See **Section 3.A.4** for the calculation). This result illustrates the great potential of the γ-$CsPbI_3$ for photovoltaic applications.

To further verify the high mobility of charge carriers in γ-$CsPbI_3$, we conducted a second estimate of the mobility from the amplitude of the OPTP data as exhibited in **Figures 3.1c and 3.1d** (see **Section 3.A.5** for more details). This is distinct from the first method, which relies on the dispersion of the complex photoconductivity. Briefly, $-\Delta E/E$ is proportional to the photoconductivity, σ, of the free charge carriers, and $\mu = \sigma/(e\,n)$. The photogenerated carrier density, n, can be obtained from the Drude model, since $\omega_p^2 = \frac{e^2 \cdot n}{\varepsilon_0 \cdot m^*}$. This estimate reveals a mobility of 258 ± 6 $cm^2V^{-1}s^{-1}$. This value is in good agreement with the polaron-based mobility estimation made from the TDS dispersion analysis, supporting the estimates of the electron-phonon coupling constant and polaron effective mass giving rise to highly mobile large polarons in black phase $CsPbI_3$.

Furthermore, based on the code developed by Frost and using the band effective mass (0.1 m_0) given by previous DFT studies [149], we calculate the maximum polaron mobility to be 344 $cm^2V^{-1}s^{-1}$ at RT for γ-$CsPbI_3$. Thus, the experimentally determined mobility in our sample reaches ~80% of the theoretical limit. The remaining difference between the experimental and theoretical results may be due to the contributions from defect scattering or dielectric drag effects in perovskites [152].

Table 3.1 | Comparison of the mobility measured in γ-$CsPbI_3$ with that from calculations and measurements in other reports for hybrid LHPs.

Material (Polycrystalline thin film)	Mobility ($cm^2V^{-1}s^{-1}$)	Technique
$CsPbI_3$ (This work)	278 ± 44	THz

$CsPbI_3$	344	Calculation[72]
$MAPbI_3$	~27	THz[143]
$MAPbI_3$	~20-75	TRMC[155],[a]
$MAPbI_3$	~25	THz[36]
$FAPbI_3$	~75	THz[156]
$FAPbI_3$	~27	THz[157]
$MAPbI_3$ (Single crystal)	~620	THz[37]

[a] TRMC = time-resolved microwave conductivity

In conclusion, we have performed a systematic THz spectroscopic study of γ-$CsPbI_3$ and revealed a remarkably high charge carrier mobility in the material, up to 270 ± 44 $cm^2V^{-1}s^{-1}$, which is nearly one order of magnitude higher than that of conventional hybrid lead halide perovskites. We further provide evidence for large polaron formation dictating the transport properties and T-dependent conductivity of the photogenerated carriers. Our results highlight the black γ-phase $CsPbI_3$ as a fascinating all-inorganic perovskite material class for efficient optoelectronics.

3.4 Conclusions

In conclusion, we have performed a systematic THz spectroscopic study of γ-$CsPbI_3$ and revealed a remarkably high charge carrier mobility in the material, up to 278 ± 44 $cm^2V^{-1}s^{-1}$, which is nearly one order of magnitude higher than that of conventional hybrid lead halide perovskites. We further provide evidence for large polaron formation dictating the transport properties and T-dependent conductivity of the photogenerated carriers. Our results highlight the black γ-phase $CsPbI_3$ as a fascinating all-organic perovskite material class for efficient optoelectronics.

3.5 Appendix

Section 3.A.1: Estimation of the direct bandgap energy in black phase $CsPbI_3$

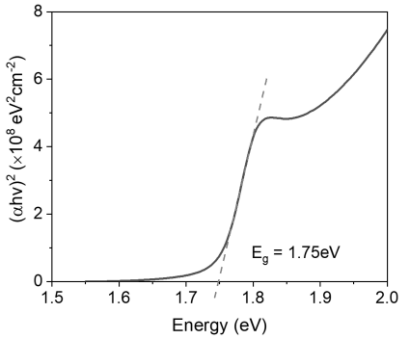

Figure 3.A.1 | Bandgap of the black phase $CsPbI_3$. Bandgap energy estimation for black phase $CsPbI_3$ by the Tauc plot method.

Section 3.A.2: Recombination rate equation fitting to the photoconductivity transient dynamics

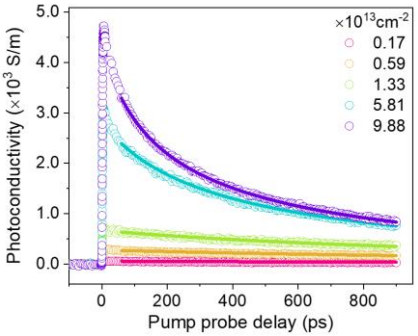

Figure 3.A.2 | Fluence-dependent THz photoconductivity for γ-$CsPbI_3$. All indicated fluences are absorbed fluences by the sample. The solid lines are fits as described in the text. The resulting rate constants k_1, k_2,and k_3 are respectively 4.42×10^{8} s^{-1}, 5.79×10^{-10} cm^3s^{-1}, and 2.60×10^{-28} cm^6s^{-1}.

To further elucidate the charge carrier dynamics in black γ-phase $CsPbI_3$ thin films, we conduct fluence dependent photoconductivity measurements and apply the recombination rate equation to globally fit the dynamics following [158]:

$$\frac{dn(t)}{dt} = -k_1 \cdot n - k_2 \cdot n^2 - k_3 \cdot n^3 \qquad (3.1)$$

in which $n(t)$ is the time-dependent carrier density. Here k_1 is the monomolecular recombination rate constant which arises from charge trapping; k_2 represents the bimolecular recombination rate constant which represents the free electron-hole pair recombination, and k_3 stands for the Auger recombination rate constant.

While instead of measuring carrier density directly in our experiment, we measure the THz response $-\Delta E/E$, which is proportional to the photoconductivity σ as mentioned above. In

principle, the photoconductivity σ is defined as: $\sigma = n \cdot e \cdot \mu$, in which n and μ are the carrier density and charge mobility, respectively. In the data fitting range, the charge mobility doesn't change in time as demonstrated in **Figure 3.2b**. As a result, the THz response $-\Delta E/E$ can be directly linked and linearly proportional to the carrier density n, which can be expressed as $n(t) = \phi \cdot C \cdot (-\Delta E/E)(t)$, where ϕ is the photon-to-charge quantum efficiency representing the number of charges created per absorbed photon and C is the proportionality of absorbed photon density N_{abs} to $-\Delta E/E$ at the peak of the OPTP dynamics (i.e., $C = N_{abs}/(-\Delta E/E)$). Substituting $-\Delta E/E$ into the rate equation and replacing $-\Delta E/E$ with x to simplify the formula, we get the derived equation as follows:

$$\frac{dx(t)}{dt} = -k_1 \cdot x - k_2 \cdot \phi \cdot C \cdot x^2 - k_3 \cdot \phi^2 \cdot C^2 \cdot x^3 \qquad (3.2)$$

Fitting all the fluence dependent THz transients globally, as shown in **Figure 3.A.2** for the γ-$CsPbI_3$ with the above equation, yields k_1, k_2 and k_3. As shown in **Figure 3.A.2**, we find that the model fits our data very well.

Since the reported rate constants are all based on the assumption of $\phi = 100\%$, we adapt this assumption as well to conduct a fair comparison, as shown in the main text and **Table 3.A.2**. However, THz time-domain spectroscopy enables us to extract the exact carrier density by the Drude model fitting to the frequency-domain conductivity, as shown in **Figure 3.2a**. With this, we estimate the photon-to-charge branching ratio ϕ by comparing the extracted carrier density from fitting to the absorbed photon density N_{abs}. A ϕ of ~30% is utilized to extract more accurate values of k_1, k_2 and k_3 as shown in **Table 3.A.1** below.

Table 3.A.1 | Comparison of rate constants k_1, k_2 and k_3 of the black phase $CsPbI_3$ with photon-to-charge conversion efficiencies of $\phi = 100\%$ and $\phi = 30\%$.

ϕ	k_1 (μs^{-1})	k_2 (10^{-10} $cm^3 s^{-1}$)	k_3 (10^{-28} $cm^6 s^{-1}$)
100%	442	5.79	2.60
30%	442	19.29	28.92

Note here, that the applicability of Equation (3.1) only holds for a homogeneous distribution of charge carriers following excitation. In our case, the initial charge density profile is not homogeneous, as the penetration depth in the black phase $CsPbI_3$ is close to the thickness of the sample (~215nm *vs.* 200 nm). This leads to an initially exponential distribution of charge carrier density following photoexcitation in the pump propagation direction, and thus local inhomogeneity of the charge carriers. Consequently, the rate equation (3.1) does not apply. For that, we estimate the diffusion time to be 57 ps for the charge carriers across the sample from

the front to the back side (based on the measured mobility of 270 $cm^2V^{-1}s^{-1}$ and the film thickness of 200 nm). Consequently, we start the fitting from 60 ps on here.

Section 3.A.3: Comparison of recombination rate constants

Table 3.A.2 | Comparison of rate constants k_1, k_2 and k_3 of the black phase $CsPbI_3$ with that of other hybrid and all-inorganic perovskites (by assuming $\phi = 100\%$, see the discussion in the last section).

Material	Technique	k_1 (μs^{-1})	k_2 (10^{-10} cm^3s^{-1})	k_3 (10^{-28} cm^6s^{-1})
$CsPbI_3$ (This work)	TRTS	442	5.79	2.60
$CsPbBr_3$	TRTS[159]	1500	13	0.01
$CsPbI_2Br$	TA[160]	865	0	0.03-1.5
$MAPbI_3$	TRTS[39]	14	9.2	1.3
$MAPbI_3$	TA[161]	-----	23	-----
$MAPbI_3$	TRMC[145]	7	13	-----
$MAPbI_3$	TRPL[162]	18	1.7	-----
$MAPbBr_3$	TRTS[163]	102-104	-----	-----
$MAPbI_{3-x}Cl_x$	TRTS[39]	12	1.1	0.23
$FAPbI_3$	TRTS[157]	6.7	1.1	2.2
$FAPbBr_3$	TRTS[157]	21	11	15

Note: TRTS: time-resolved THz spectroscopy; TA: transient absorption; TRMC: time-resolved microwave conductance; TRPL: time-resolved photoluminescence.

The extracted k_2 and k_3 of black γ-phase $CsPbI_3$ are very similar to that previously reported for other organic-inorganic hybrid LHPs: i.e., from the perspective of intrinsic carrier lifetime, there seems to be no major difference between $CsPbI_3$ and other LHPs. The inferred k_1(~442 μs^{-1}), on the other hand, is about 2-order of magnitude larger than previously reported values

(<10 μs^{-1}). This may indicate the presence of a relatively high density of trap states in our samples, which limits the carrier lifetime to ~2.1 ns (see below). This extrinsic effect can be further reduced by improving the crystallinity and passivating the defects [164].

Section 3.A.4: Estimation of charge carrier lifetime and diffusion length

The charge-carrier diffusion length is calculated following the equation [40]:

$$L_D = \sqrt{D \cdot \tau} = \sqrt{\frac{D}{R_{total}(n)}} \tag{3.3}$$

where D is the diffusion coefficient ($D = \mu \cdot k_B \cdot T/e$), $\tau = 1/R_{total}(n)$ is the carrier lifetime, R_{total} is the carrier density-dependent total charge carrier recombination rate, which is defined by:

$$R_{total}(n) = -\frac{1}{n}\frac{dn}{dt} = k_1 + k_2 \cdot n + k_3 \cdot n^2 \tag{3.4}$$

Section 3.A.5: Mobility estimation from optical pump-THz probe (OPTP) measurement

As mentioned above, the photoconductivity σ can be inferred from THz response transients according to the thin-film approximation, from which the charge mobility could be calculated following: $\mu = \sigma/(e \cdot n)$ where $n\ (= \phi N_{abs})$ is the photogenerated carrier density. Normally, the carrier density is set to be the absorbed photon density N_{abs} by assuming the photon-to-charge branching ratio ϕ to be 100%. In reality, the branching ratio can be much smaller than 100%, so the estimation of charge mobility from OPTP represents the lower limit. In our work, the frequency domain conductivity can be well fitted by the Drude model as shown in **Figure 3.2**, so the photogenerated carrier density can be directly extracted in the fitting without any assumption. Because of the relatively long carrier lifetime (~2 ns), we can safely assume that the carrier density keeps the same during the first 10 ps. Plugging in the extracted carrier density, we therefore calculated the mean value of mobility from 5 to 10 ps to be 258 ± 6 $cm^2V^{-1}s^{-1}$.

4 Experimental quantification of the Mott polaron density in lead halide perovskites

Free, mobile charges in lead halide perovskite (LHP) are known to form polarons: a quasiparticle consisting of the charge carrier dressed with a local lattice deformation. Isolated polarons, at low density, have been well-researched, but at elevated polaron densities, many-body interactions occur, relevant for LHP-based devices such as light-emitting diodes and concentrator photovoltaics. Specifically, when the polaron density exceeds the so-called Mott criterion (i.e., Mott polaron density), the polaron wavefunctions overlap, affecting the optoelectronic properties of LHPs. However, the Mott polaron density in LHPs has been largely unexplored experimentally. Here, employing ultrafast terahertz spectroscopy, we report the first experimental quantification of the Mott polaron density in LHPs to be ~10^{18} cm^{-3} which agrees well with theoretical calculations based on the Feynman polaron model. The signature of the electronic phase transition in LHPs is found to be universal and independent of the constituted ions. Exceeding the Mott polaron density, excess photoinjected charge carriers annihilate quickly within tens to hundreds of picoseconds, reaching the stable and long-lived Mott density. These results have large implications for device design, but also for understanding exotic phenomena observed in LHPs, including strong Auger recombination and slow hot carrier cooling.

4.1 Introduction

Low-temperature solution-processed lead halide perovskites (LHPs) have shown superior performance in various electro-optic applications, such as light-emitting diodes (LEDs) [21,165] and photovoltaic cells [18,19]. These devices rely on the interconversion of photons and mobile charge carriers. Due to the ionic and soft nature of perovskite crystal lattice, the lattice is readily polarized and distorted around an injected charge carrier. The charge carrier becomes dressed by a local lattice deformation, forming a polaron quasiparticle. Because of the weak-to-intermediate electron-phonon interaction in LHPs, large polarons develop, with the lattice distortion spanning over multiple lattice constants, i.e., a few nanometers (nm). Large polaron formation has been proposed in LHPs to underpin their fascinating optoelectronic properties [63], including long carrier lifetime [38], modest charge mobility [25], and high defect tolerance [119]. The polarized crystal structure could act as a protection ‘shield’ to effectively screen the Coulomb interactions between the charge carriers and ionized defects, phonons, and among

themselves. So far, the spectroscopic and transport studies of polarons in LHPs have mainly focused on the low polaron density (~10^{16} cm^{-3}) regime [44,143,166], relevant for, for instance, solar cell applications, where large polarons are, on average, well-separated.

LHPs have also shown great potential in other optoelectronic applications, including LEDs [21], lasing [167], and concentrator photovoltaics [168], where the photoinjected carrier density exceeds 10^{18} cm^{-3}. In this high-density regime, the distorted lattice pattern from different polarons may start to interfere as polarons approach each other. The resultant polaron-polaron interaction may significantly impact the optoelectronic properties, including charge transport and carrier lifetime. For example, strong Auger recombination is typical for LHPs, leading to an efficiency roll-off in, e.g., LEDs [169,170]. Extremely long-lived hot carriers with lifetime >100 picoseconds (ps) have been reported in LHPs [43] at carrier densities exceeding 10^{18} cm^{-3}. Frost *et al.* attributed this delayed hot carrier cooling at high fluence to a Mott transition defined at the carrier density where polaron wavefunctions overlap [171]. This critical density is also referred to as Mott polaron density [24,171], being analogous to the metal-nonmetal transition that is observed in doped semiconductors [172]. However, the specific polaron density regime has remained largely unexplored experimentally for LHPs, despite its importance and relevance for many applications.

In this work, we employ ultrafast Terahertz (THz) spectroscopy to quantify the Mott polaron density N_{Mott} in LHPs to be ~10^{18} cm^{-3}, in line with theoretical estimation from a numerical solution to the Feynman polaron model. This effect is found to be universal and independent of the detailed composition of LHPs, representing an intrinsic property of LHPs. With increasing excitation density, the excess photoinjected charge carriers beyond N_{Mott} annihilate quickly within tens to hundreds of ps to form a stable, long-lived Mott polaron state.

4.2 Materials

Synthesis of lead halide perovskites

All reagents were used as received without any further purification. Methylammonium iodide >99.99% (Greatcell Solar Materials); Lead(II) iodide ultra-dry 99.999% (metals basis) (Thermo Scientific™); N,N-Dimethylformamide 99.8% Extra Dry over Molecular Sieve AcroSeal® (Acros Organics); Cesium bromide 99.9% (metals basis) (Thermo Scientific™); Lead (II) bromide ≥98% (Sigma Aldrich); Methyl sulfoxide 99.7+% Extra Dry over Molecular Sieve AcroSeal® (Acros Organics); Chlorobenzene 99+% for spectroscopy (Acros Organics); γ-Butyrolactone ReagentPlus® ≥99% (Sigma Aldrich); Cesium iodide 99.9% trace metals basis (Sigma Aldrich).

The substrates for the film deposition consisted of fused silica substrates (1 cm×1 cm) which were washed with isopropanol, dried and left in an ozone reactor chamber for 30 minutes.

Thin films of $CH_3NH_3PbI_3$ were prepared by a modified protocol according to a previous report.[1] CH_3NH_3I (0.0795 g) and PbI_2 (0.2301 g) were mixed in a 1:1 stoichiometric ratio in anhydrous N,N-dimethylformamide (1 mL) to give a 0.5 M solution, which after stirring at room temperature for at least 20 minutes produced a clear $CH_3NH_3PbI_3$ solution. The solution was filtered with a 0.20 µm pores hydrophilic PTFE filter. The perovskite film deposition was performed under an inert atmosphere inside a glovebox. The $CH_3NH_3PbI_3$ solution (50 µL) was deposited on the fused silica glass, and then spin-coated at 5000 rpm for 30 s. The solvent was evaporated at 100°C for 10 min (still in the glovebox), resulting in a clear brown film. The more diluted $CH_3NH_3PbI_3$ film was obtained by diluting 15 µl of the former $CH_3NH_3PbI_3$ solution in 45 µl of anhydrous DMF, while keeping the rest of the protocol the same. The film was stored in the dark under inert atmosphere until further measurements.

$CsPbBr_3$ thin films were prepared by spin-coating a 0.5 M DMSO solution of CsBr and $PbBr_2$ (1:1 stoichiometric ratio). The solution was prepared by mixing CsBr (0.1064 g) and $PbBr_2$ (0.1835 g) in 1-1.5 mL of dry DMSO at around 70 °C. The solution was then filtered with a 0.20 µL pore PTFE hydrophilic filter. For obtaining the thin film, 70 µL of the perovskite solution was spin-coated on the fused silica glass, in a glovebox. Subsequent spin coating at 1000 rpm for 10 s, followed by 60 s at 3000 rpm with the addition of 125 µl of chlorobenzene 35 s before the end of the program, resulted in the desired thin film after solvent evaporation (for 10 minutes on a hot plate at 60 °C). The diluted $CsPbBr_3$ thin film was prepared by diluting the former perovskite solution by 25% in volume, while retaining all other steps. Both the films were annealed outside the glovebox for 30 minutes at 150 °C. The films were stored in the dark under inert atmosphere until further measurements.

$CsPbI_3$ thin films were prepared from a 1:1 stoichiometric solution of CsI and PbI_2, similarly as shown in Chapter 3. The two salts were mixed in a 4:1 DMSO:GBL solution (1 M) at 60°C overnight and then filtered with a 0.20 µL pore PTFE hydrophilic filter. 70 µL of the clear solution was spin coated on the substrate using the following program: 300 rpm for 30 s, 1000 rpm for 20 s and finally 4000 rpm for 60 s. The coated substrate was heated first at 160 °C for 1 hour and then at 320 °C for 15 minutes, until the substrate changed colour to the desired black phase. The whole procedure was carried out under inert atmosphere (N_2) in a glovebox. The samples were stored in the dark under an inert atmosphere for further measurements.

4.3 Results and Discussion

In this work, three types of LHPs (i.e., $MAPbI_3$, $CsPbI_3$, and $CsPbBr_3$) are prepared and spin-coated on the fused silica substrates for THz measurements. The UV-vis absorption spectra are measured and shown in **Figure 4.A.1**, and the inferred optical properties (e.g., bandgap) are consistent with previous reports. During THz measurements, the samples are kept under a high

vacuum in a cryostat with a background pressure of ~2×10^{-4} mbar. We observe no sample degradation during the THz measurements.

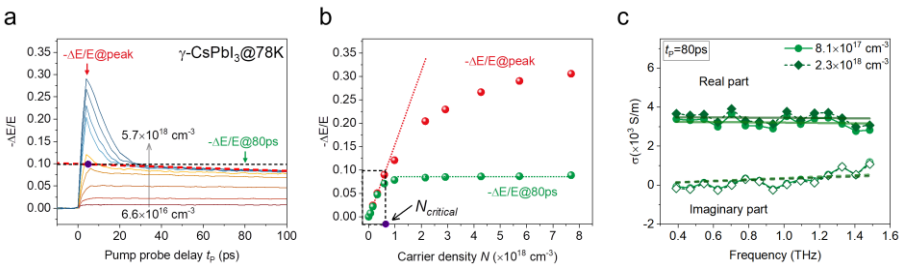

Figure 4.1 | Carrier density saturation in black γ-CsPbI$_3$. (a) Time-dependent $-\Delta E/E$ signals (reflecting carrier densities) at different fluences, in black γ-CsPbI$_3$ at 78 K, with pump photon energy of 3.10 eV. The red dashed line is a linear extrapolation of the slow decay between 40 ps and 100 ps at the highest fluence to zero delay. The black dashed line denotes the corresponding signal at the peak $-\Delta E/E$ (the purple dot). **(b)** The intensity of $-\Delta E/E$ at the peak and at t_P = 80 ps in **(a)** as a function of initially photoinjected carrier density. The red dotted line is the linear fit to peak $-\Delta E/E$ values in the low carrier density regime. The green dashed line is the constant fit to $-\Delta E/E$ at t_P = 80 ps in the high carrier density regime. $N_{critical}$ is defined as the carrier density at which peak $-\Delta E/E$ value is the same with the cross point (the purple dot) in **(a)**. **(c)** Frequency-resolved complex photoconductivity spectra consisting of real and imaginary components measured at t_P = 80 ps for initial carrier density of 8.1×10^{17} cm^{-3} and 2.3×10^{18} cm^{-3}. The solid and dashed lines represent the Drude fits.

To investigate the polaron dynamics in LHPs, we use contact-free optical pump-THz probe spectroscopy and THz time-domain spectroscopy. In **Figure 4.1a**, we show the fluence-dependent OPTP dynamics in black γ-CsPbI$_3$ at 78 K with varying photoinjected carrier density N for over nearly two orders of magnitude (from 6.6×10^{16} cm^{-3} to 5.7×10^{18} cm^{-3}). N is determined by taking into account the incident photon density N_{photon}, the sample absorption A and the photon-to-charge quantum yield Φ: $N = \Phi N_{photon} A$. Φ is around 30% for black γ-CsPbI$_3$ [166]. An independent determination of the quantum yield from the plasma frequency obtained from the terahertz conductivity spectra confirms this number (see **Section 4.A.2**). Due to the similar effective masses [149], both electrons and holes are included here as they contribute almost equally to the measured photoconductivity. With increasing carrier density N, distinct features appear in the OPTP dynamics: in the low excitation regime (N < ~7×10^{17} cm^{-3}), the amplitude of the photoconductivity increases linearly with excitation density, and shows little decay within our time window of ~1 ns (see the inferred lifetime at low fluence in **Figure 4.A.3** in the Appendix). The observed low charge carrier recombination rate is fully in line with our previous report on the carrier dynamics of γ-CsPbI$_3$ [166], and is also consistent with the picture of large polaron formation, which reportedly screens the charge carriers from

defects and other charge carriers [38,74,142,166]. When the polaron density is low, the overlap between their wavefunctions is small, thus limiting the bimolecular recombination rate. In the high excitation regime (with N > ~7×10^{17} cm^{-3}), a rapid decay appears with the decay time spanning from several to tens of ps, then followed by a long-lived signal again as in the low excitation regime (see **Figure 4.A.3** for fluence-dependent OPTP dynamics at long time scale). The peak photoconductivity increases continuously with photoinjected carrier density, yet the signals quickly decay to the same level, independent of the initial excitation density. This unique carrier density-dependent photoconductivity evolution is summarized in **Figure 4.1b**, by plotting the signal amplitude at two time points: at the photoconductivity peak, and at 80 ps after photoexcitation. This figure reveals the existence of a critical charge carrier density $N_{critical}$: below $N_{critical}$, the photoconductivity increases linearly with N, and it is long-lived; exceeding $N_{critical}$, the peak photoconductivity is still increasing with N, yet the conductivity at later times (e.g., t_P = 80 ps) reaches a plateau. Note the slight carrier density decay from ~30 ps after the signal is saturated. To accurately estimate the critical density $N_{critical}$, we extrapolate the long-lived signal at the highest fluence (from 40 ps to 100 ps here for γ-CsPbI$_3$) back to peak $-\Delta E/E$ value as shown in **Figure 4.1a** and then project this value to the corresponding carrier density N, i.e., critical density $N_{critical}$ by using the linear relation of peak $-\Delta E/E$ with N at low fluences. For black γ-CsPbI$_3$ investigated here, we find $N_{critical}$= (6.4 ± 1.5)×10^{17} cm^{-3}.

To verify that the long-time photoconductivity for all excitation fluences reaches the same state and is determined by the charge carrier density, and is not affected by varying mobility, we measured full photoconductivity spectra at t_P = 80 ps. **Figure 4.1c** shows two typical complex photoconductivity spectra under two different excitation densities (with N = 8.1×10^{17} cm^{-3} and 2.3×10^{18} cm^{-3}). The complex spectra display the same dispersion and intensity (see more data and discussion below). This result indicates that independent of initial excitation density, for t_P > 30 ps, the charge carriers reach the same state with the same charge mobility and carrier density, independent of the initial excitation density. The fast carrier loss during the first 30 ps is consistent with Auger recombination, as detailed in **Section 4.A.4** in the Appendix.

At the same time, THz-TDS measurement provides an independent way to estimate the critical density, that is, to fit the photoconductivity spectrum by theoretical models (e.g., Drude model or Drude-Smith model) and extract the carrier density (see the spectra and fitting for all three samples in the Appendix). For black γ-CsPbI$_3$, we fit the photoconductivity spectrum (measured at t_P = 80 ps at excitation fluence of 9.35×10^{17} cm^{-3}) by the Drude model. Correcting for the small density decay occurring up to 80 ps, we find $N_{critical}$= (7.2 ± 1.4)×10^{17} cm^{-3}, in good agreement with the value obtained from the OPTP result. Importantly, we find the critical density is independent of the excitation photon energy (see a comparison of 400 nm and 750

nm excitation in **Section 4.A.6**). This result further confirms the intrinsic origin of the observed critical density.

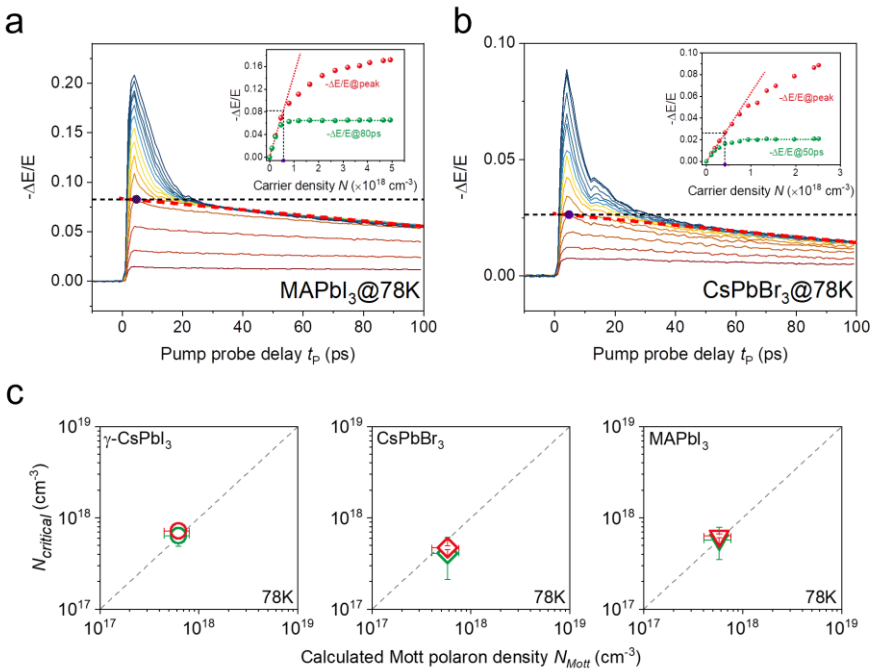

Figure 4.2 | THz measurements in $MAPbI_3$ and $CsPbBr_3$. (a, b) The fluence-dependent OPTP dynamics in $MAPbI_3$ and $CsPbBr_3$ at 78 K, with an excitation photon energy of 3.10eV. Insets: the intensity of $-\Delta E/E$ at the peak and at later time delays (t_P = 80 ps for $MAPbI_3$ and t_P = 50 ps for $CsPbBr_3$) as a function of photoinjected carrier density. **(c)** The comparison between the experimentally extracted critical density $N_{critical}$ and the calculated Mott polaron density based on the Feynman polaron model for $CsPbI_3$, $MAPbI_3$ and $CsPbBr_3$. The green symbols represent $N_{critical}$ from OPTP measurements, while the red symbols are $N_{critical}$ extracted from THz-TDS measurements. The dashed line indicates $N_{critical} = N_{Mott}$.

To test whether the observed carrier density saturation is unique for black γ-$CsPbI_3$, we conduct measurements on the other two popular LHPs, $MAPbI_3$ and $CsPbBr_3$, with either A-site cation or X-site anion being changed in comparison to $CsPbI_3$. Although some details about OPTP dynamics vary for different perovskites (e.g., the carrier lifetime and signal amplitude), the same carrier-density saturation phenomenon is observed in $MAPbI_3$ and $CsPbBr_3$ when the carrier density exceeds a threshold $N_{critical}$, as shown in **Figures 4.2a and 4.2b**. Based on this observation, we can conclude that this effect seems universal in LHPs, including organic-inorganic hybrid and all-inorganic LHPs, independent of the constituted ionic composition. By the same approach utilized in black γ-$CsPbI_3$ to extract the critical density from OPTP measurement, the insets of **Figures 4.2a and 4.2b** show that the obtained $N_{critical}$ for $MAPbI_3$

and $CsPbBr_3$ are $(5.7 \pm 2.2)\times10^{17}$ cm^{-3} and $(4.1 \pm 2.0)\times10^{17}$ cm^{-3}, respectively. By THz-TDS, we extract the fitted $N_{critical}$ for $MAPbI_3$ and $CsPbBr_3$ are $(5.8 \pm 0.3)\times10^{17}$ cm^{-3} and $(4.7 \pm 0.2)\times10^{17}$ cm^{-3} respectively, with taking the density decay into consideration as well (see **Section 4.A.5**).

Converting the critical density to the average distance d between neighboring carriers, we estimate d to be around 10 nm. This value is similar to the polaron diameter in LHPs [171,173]. This simple estimate indicates that the $N_{critical}$ can be interpreted as the Mott polaron density N_{Mott} in LHPs in which neighboring polarons overlap, sets the upper limit of the charge carrier density that LHPs can support. To examine this hypothesis, in **Figure 4.2c** we correlate the experimentally extracted critical density $N_{critical}$ (from both OPTP and THz-TDS) to the calculated N_{Mott} for all three perovskites at 78K. The Mott polaron density is calculated based on a finite temperature numeric solution to the Feynman polaron model [72]. The polaron radius is defined following Schultz as the width of the Gaussian polaron wavefunction ansatz in the Feynman model [174]. Assuming for simplicity that the polaron occupies a cube with sides twice the polaron radius, the Mott polaron density is thus inferred. The parameters used for calculating N_{Mott} for the three perovskites are shown in **Table 4.A.2** in the Appendix. As can be seen in **Figure 4.2c**, a direct correlation between the extracted critical density $N_{critical}$ and the Mott polaron density N_{Mott} is evident for all three LHPs.

However, the variation between $N_{critical}$ and N_{Mott} for the different LHPs is relatively small. A more critical test of the hypothesis that $N_{critical} = N_{Mott}$ can be performed by varying the temperature, since in the Feynman theory the polaron radius, and thereby N_{Mott}, is strongly temperature (T)-dependent. The polaron size increases as T decreases [171], as shown schematically in **Figure 4.3a**. Correspondingly, the model predicts that the Mott polaron transition density will increase with T. **Figure 4.3b** shows the calculated N_{Mott} at different T for black γ-$CsPbI_3$. The calculated Mott polaron density increases by over a factor of 4, from 50 K to 300 K. To check the effect of T on the OPTP dynamics and critical density, **Figure 4.3c** shows the fluence-dependent OPTP measurement in black γ-$CsPbI_3$ at 286 K as an example (see more T-dependent OPTP measurement in **Figure 4.A.7**), and the inset displays the extraction of critical density. With increasing initial excitation density, the signal saturation happens at hundreds of ps at 286 K, instead of tens of ps at 78 K. The extracted critical density here is $(1.47 \pm 0.3)\times10^{18}$ cm^{-3} which is very close to the calculated Mott density of 1.67×10^{18} cm^{-3} at 286 K. In **Figure 4.3d**, we further show the inferred $N_{critical}$ at T varying from 78 K to 286 K, which correlates well with N_{Mott} obtained from calculations. Note that there is no phase transition [53] for black γ-$CsPbI_3$ below room T, and we observe nearly no change in photon-to-carrier conversion efficiency within this T range (see **Figure 4.A.8**). This T-dependent result further supports the existence of a Mott polaron transition in LHPs. This

delayed signal saturation at high *T* indicates a slower stabilization at the Mott polaron density, which may be due to increased thermal disorder (anharmonic phonon scattering) at elevated temperatures. The higher Mott density impedes thermal dissipation from hot polarons [171].

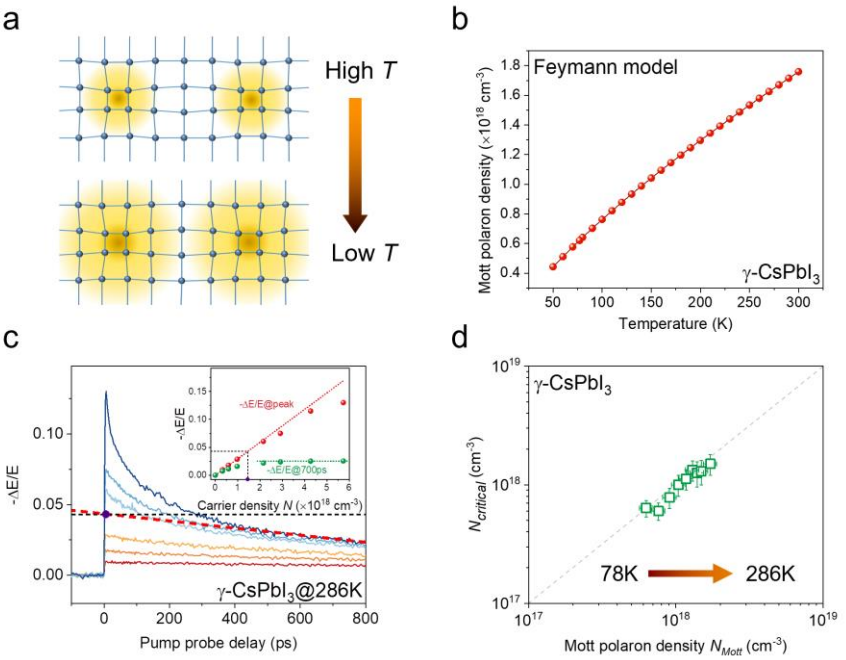

Figure 4.3 | Temperature-dependent critical density in LHPs. (a) Schematic illustration of polaron size evolution with lowering temperature. **(b)** The calculated Mott polaron density as a function of temperature based on the finite temperature Feynman polaron model for black γ-$CsPbI_3$. **(c)** Fluence-dependent OPTP dynamics at 286 K in black γ-$CsPbI_3$ with an excitation photon energy of 3.10 eV. Insets: the intensity of -ΔE/E at the peak and at t_P = 700 ps as a function of photoinjected carrier density. The dashed red line shows extrapolation back to zero pump-probe delay from data between 500 and 800 ps, at high excitation density, as in **Figure 4.1c**. **(d)** The comparison between the experimentally (OPTP) extracted critical density $N_{critical}$ and the calculated Mott polaron density at different temperatures for $CsPbI_3$. The dashed line indicates where $N_{critical}$ and N_{Mott} are the same.

After establishing the Mott polaron density, we characterize the charge transport properties below and above it. In **Figures 4.4a** and **4.4b**, we show two typical photoconductivity spectra of black γ-$CsPbI_3$ at 78 K following two excitation fluences, below and above the Mott density: 1×10^{17} cm^{-3} and 2.33×10^{18} cm^{-3}. Both measurements are conducted at 80 ps following optical excitations to ensure that Mott polaron states are established following exceeding-Mott density excitations. As we can see, both photoconductivity spectra share the same feature, with a positive, decreasing real part and a positive, increasing imaginary part with frequency. This is a clear signature of delocalized band transport and can be well fitted by Drude model (the solid

and dash lines in **Figures 4.4a and 4.4b**). **Figure 4.4c** summarizes the extracted scattering time τ and carrier density from Drude fitting at different fluences. With increasing incident fluence, the fitted carrier density grows rapidly and then saturates at a carrier density of ~6.4×10^{17} cm^{-3}, consistent with the inferred Mott density above in γ-$CsPbI_3$ at 78 K. On the other hand, the extracted scattering time shows a strong-fluence dependent transition, from an almost fluence-independent high scattering value of over 40 fs at low polaron density (for absorbed photon density below ~40% of Mott density) to less than 20 fs above the Mott density. This result indicates that even at the Mott polaron density, delocalized band transport still prevails in LHPs, but that some additional scattering pathway has activated. Most likely this is carrier-carrier scattering now that the polaron wavefunctions are overlapping. On the other hand, the enhanced carrier scattering interaction does reduce the charge mobility ($\mu = e\tau/m^*$, with m^* as the effective mass).

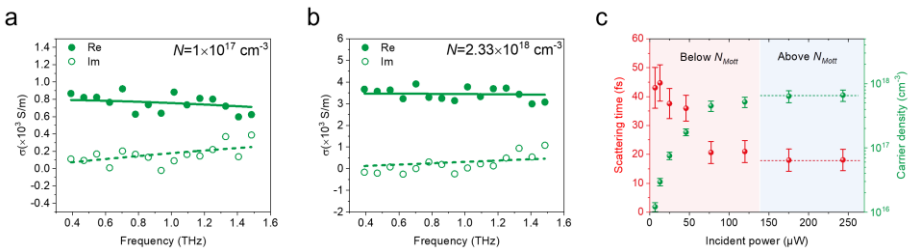

Figure 4.4 | Fluence-dependent complex photoconductivity for black γ-$CsPbI_3$ measured at t_P = 80 ps at a temperature of 78 K. (a, b) Frequency-resolved photoconductivity spectra (filled and empty circles) and Drude model fits (solid and dashed lines) at initial photogenerated carrier density of 1×10^{17} cm^{-3} and 2.33×10^{18} cm^{-3}. (c) The extracted scattering times and carrier densities from Drude fitting at different incident fluences.

The observation of Mott polaron density sets the upper limit on the available large polaron population that LHPs can host. Theoretically, Emin predicted an emerging repulsive interaction acting as an energy barrier between the oppositely charged large polarons when the polaron separation is small enough [175]. Such repulsive polaronic interactions are balanced by the electron-hole Coulomb attraction, determining the spatial energy landscape of polaron states. These balanced interactions underlie the formation of Mott polaron density in LHPs. Besides the low trapping rate (so-called "defect tolerance" effect) reported in LHPs linked to the dielectric screening that also drives large polaron formation, our discussion here can also explain the weak bimolecular recombination rate (i.e., free electron-hole recombination) and thus long carrier lifetime in LHPs in solar cell applications.

At high excitation densities (N >10^{18} cm^{-3}), unexpectedly strong Auger recombination in LHPs is often deduced from spectroscopic studies, including THz spectroscopy [144,166],

transient absorption spectroscopy [89,176]. The inferred Auger coefficient is almost two orders of magnitude higher in LHPs than in conventional semiconductors with similar bandgaps [169]. This strong Auger recombination leads to the efficiency roll-off in LEDs [170] and concentrator photovoltaics [168] when the carrier density is above ~10^{18} cm^{-3}. In addition, exceptionally accelerated dynamics decay is observed at lower temperatures [144,177]. Yet, the underlying mechanism for the strong Auger recombination in LHPs is still under debate. These observations can be rationalized by the Mott polaron picture. For densities exceeding N_{Mott}, the enforced overlap of polarons weakens the protection of the induced charge [178]. This results in enhanced electron-hole interaction and therefore a faster population annihilation rate [44]. At lower temperatures, the population reduces to the Mott polaron density faster, within tens of ps, in line with the enhanced Auger recombination at low *T*.

The observed Mott density may also be closely related to the carrier densities at which long hot carrier lifetimes have been reported in LHPs. Yang *et al.* reported lifetimes up to 100 ps in $MAPbI_3$ and $FAPbI_3$ at a carrier density of 6×10^{18} cm^{-3} and they attribute this observation to hot phonon bottleneck effect [43]. Frost *et al.* proposed this slowed hot carrier cooling at high fluence originates from the polaron overlap and shared phonon subpopulation [171]. Our results support the latter picture. Due to the destabilized polaron protection, the hot carrier-LO phonon interaction increases with fluence. However, polaron overlap impedes the phonon diffusion away from the polarons, which, in turn, reheats the hot carriers.

4.4 Conclusions

In summary, we observe the formation of a critical Mott polaron density in lead halide perovskites. The effect is found to be universal and independent of the constitute ion nature. Above the Mott polaron density, the photoinjected excess carriers annihilate during tens to hundreds of ps depending on the temperature. Quantitative agreement is found between the inferred transition density (from observed accelerated recombination) and the calculated transition density from the temperature-dependent Feynman variational polaron theory. Our results are crucial for understanding the intrinsic optoelectronic properties of LHPs and shed light on the performance of light-concentrated optoelectronic devices.

4.5 Appendix

Section 4.A.1: The UV-vis absorption spectrum and bandgap estimation

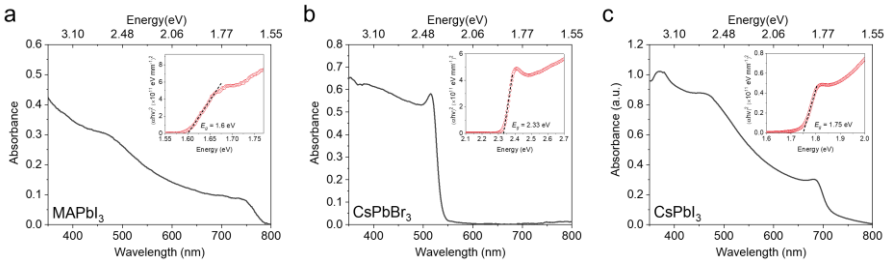

Figure 4.A.1 | The UV-vis absorption spectra for $MAPbI_3$, $CsPbBr_3$ and black γ-$CsPbI_3$ measured at room temperature. The insets are the Tauc plots for estimating the bandgaps. The absorption spectra and the inferred bandgaps are consistent with previous reports [166,179,180].

Section 4.A.2: Determination of photon-to-carrier quantum yield Φ

To assess the photon-to-carrier quantum yield, we conducted the THz-TDS to obtain the photoconductivity spectrum and then fitted it with Drude or Drude-Smith models, which are commonly used to characterize the charge transport in solids [91].

By fitting these models to the photoconductivity spectra, we can extract the carrier density and thus the photon-to-carrier quantum yield Φ.

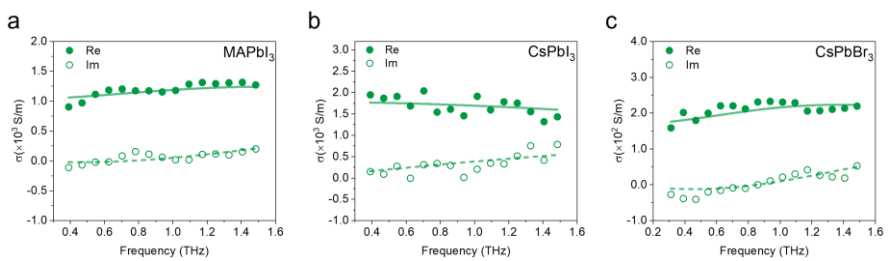

Figure 4.A.2 | The frequency-resolved photoconductivity spectra for $MAPbI_3$, $CsPbBr_3$ and black γ-$CsPbI_3$ measured at 78 K. The absorbed photon densities used for conducting these measurements are listed below in the Table 4.A.1.

Table 4.A.1 | The estimation of photon-to-carrier quantum yield Φ for three perovskites

Sample	$N_{Absorbed}$ (cm^{-3})	N_{Fitted} (cm^{-3})	Φ (%)
$MAPbI_3$	8.30×10^{17}	1.27×10^{17}	~15
$CsPbI_3$	5.87×10^{17}	1.75×10^{17}	~30
$CsPbBr_3$	6.30×10^{17}	0.51×10^{17}	~8

Here, $N_{Absorbed}$ is the absorbed photon density by taking into account the incident photon density and sample absorption, N_{Fitted} is the extracted carrier density from the fitting to the photoconductivity spectra.

Section 4.A.3: Lifetime estimation at low fluence for black γ-CsPbI$_3$

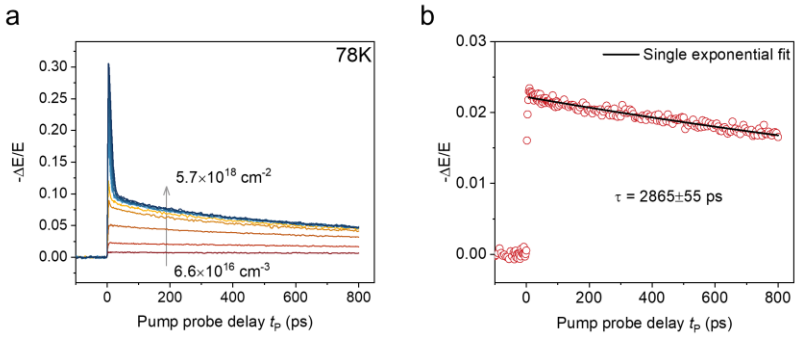

Figure 4.A.3 | OPTP dynamics at different fluences. (a) The fluence-dependent OPTP dynamics for black γ-CsPbI$_3$ at 78 K. **(b)** The OPTP dynamics at a carrier density of 1.58×10^{17} cm^{-3}. The black solid line is the single exponential fit with the inferred lifetime of around 2.9 ns.

Section 4.A.4: Discussion on the fast decay of OPTP dynamics

Here we take MAPbI$_3$ as an example for the discussion of fast decay in the fluence-dependent OPTP dynamics. We attribute the fast decay to Auger recombination with mobility changing at high fluences. At photoinjected carrier density higher than 10^{18} cm^{-3}, the effective mass of charge carriers will increase due to the band-filling effect [181]. At the same time, there is a reduced scattering time because of the enhanced carrier-carrier or carrier-phonon interaction [109,110]. Since the THz signal $-\Delta E/E(t)$ is proportional to the photoconductivity σ which is further related to the carrier density $N(t)$ and charge mobility $\mu(N) = e \cdot \tau(N)/m^*(N)$ (see the main text), the time-resolved THz signal can be expressed as following:

$$-\Delta E/E\,(t) = c \cdot N(t) \cdot e \cdot \mu(N) \qquad (4.1)$$

c is the proportionality factor which can be determined independently at the low carrier density regime where the mobility is a constant.

The Auger recombination follows the recombination rate equation:

$$dN(t)/dt = -k_3 \cdot N^3 \qquad (4.2)$$

k_3 is the Auger recombination constant. Solving the differential equation, we obtain the time-dependent expression of $N(t)$.

For the carrier density-dependent effective mass $m^*(N)$, we take the calculated result from Aron [181]. Putting $N(t)$ and $m^*(N)$ into Equation (4.3), and then we fit it globally to the fluence-dependent OPTP dynamics in **Figure 4.A.4a**. As we can see, the fitting is adequately fine, indicating the capture of the decay essence. From the fitting, we extract the carrier density-dependent mobility and scattering time. In **Figure 4.A.4c**, the carrier density-dependent scattering time is further fitted by the empirical Caughey-Thomas relation [110].

We conclude that the fast decay can be well described by Auger recombination with varied mobility. The signal variation with increasing charge carrier density is predominantly due to a reduction in the scattering time (factor of 5), in addition to a small contribution from an increase in effective mass (factor of 1.2).

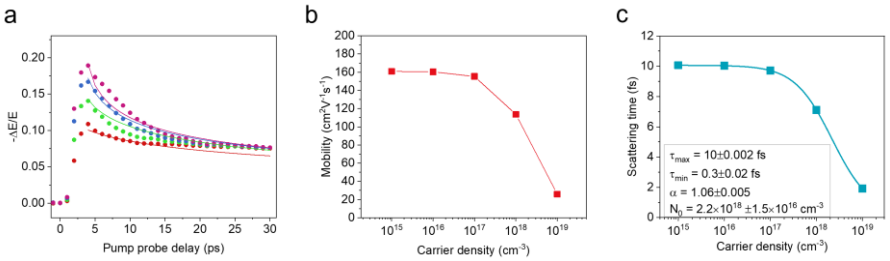

Figure 4.A.4 | Auger recombination fits to the OPTP dynamics of $MAPbI_3$. (a) The fluence-dependent OPTP dynamics for $MAPbI_3$ at 78K. The dots are the experimental data; the solid lines are fits, as discussed above. **(b)** The extracted charge mobility and **c,** scattering time from the fitting. The solid line in c is the fitting by Caughey-Thomas relation.

Section 4.A.5: The extraction of critical density by THz-TDS

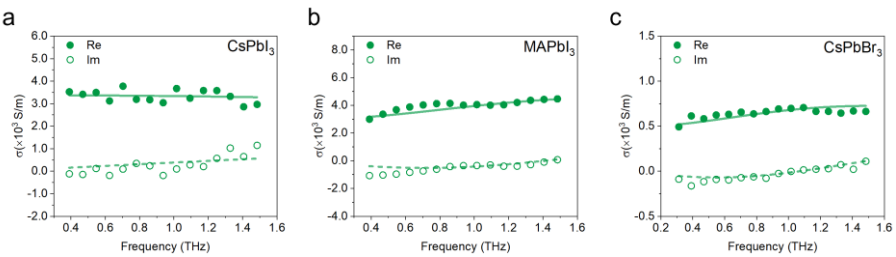

Figure 4.A.5 | Frequency-domain photoconductivities and the Drude (Drude-Smith) fits. The frequency-resolved complex photoconductivity spectra measured 80 ps after photoexcitations at 78 K for **(a)** $CsPbI_3$ at initially photoinjected carrier density of 9.35×10^{17} cm^{-3}, **(b)** $MAPbI_3$ at 5×10^{18} cm^{-3}, **(c)** $CsPbBr_3$ at 1.35×10^{18} cm^{-3}. The solid and dashed lines are the Drude model fit for $CsPbI_3$ and Drude-Smith model fit for $MAPbI_3$ and $CsPbBr_3$.

Table 4.A.2 | The extracted parameters from the above fitting

Sample	Scattering time (fs)	Carrier density (10^{17} cm^{-3})	Parameter *c*
$CsPbI_3$	18 ± 4	6.62 ± 1.35	0
$MAPbI_3$	64 ± 3	5.82 ± 0.31	-0.66 ± 0.02
$CsPbBr_3$	80 ± 5	6.14 ± 0.42	-0.65 ± 0.02

Section 4.A.6: Extracted critical densities at different pump wavelength

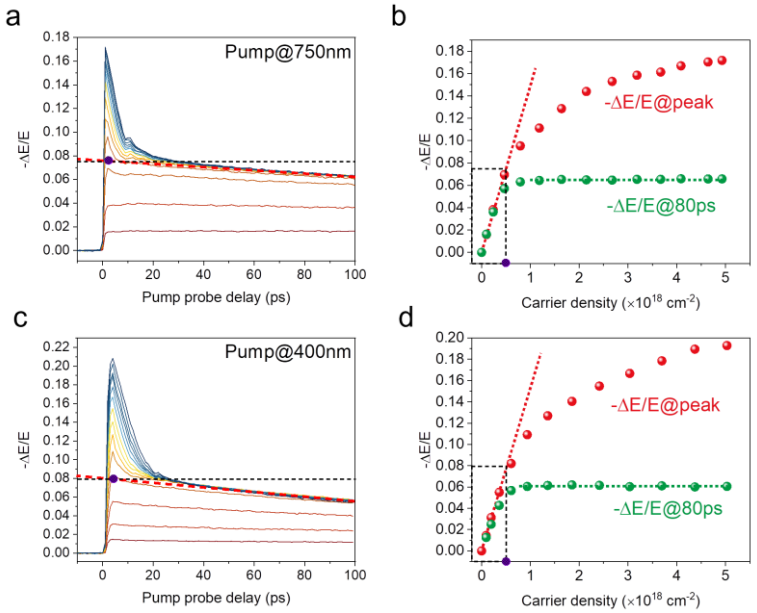

Figure 4.A.6 | OPTP dynamics of $MAPbI_3$ at different pump wavelengths. The fluence-dependent OPTP dynamics and the extraction of critical density for $MAPbI_3$ at 78K for excitation wavelengths of **(a, b)** 750 nm and **(c, d)** 400 nm. The extracted critical density for both wavelengths is around 5×10^{17} cm^{-3}, indicating the independence of the inferred critical density on the pump wavelength.

Section 4.A.7: Mott polaron density calculation based on Feynman polaron model

Table 4.A.3 | The material parameters utilized for calculating the Mott polaron density based on Feynman polaron model [72,74,76,149,173]

Sample	ε_0	ε_∞	υ_{LO} (THz)	m* (m_0)
$CsPbI_3$	18.10	6.1	2.57	0.10
$MAPbI_3$	33.5	5.0	3.38	0.10
$CsPbBr_3$	29.37	4.3	4.07	0.17

Here, ε_0 and ε_∞ are the static and optical dielectric functions in units of vacuum permittivity, υ_{LO} is the effective optical phonon frequency, m* is the effective mass in units of rest mass m_0.

Section 4.A.8: The extraction of critical density at different temperatures

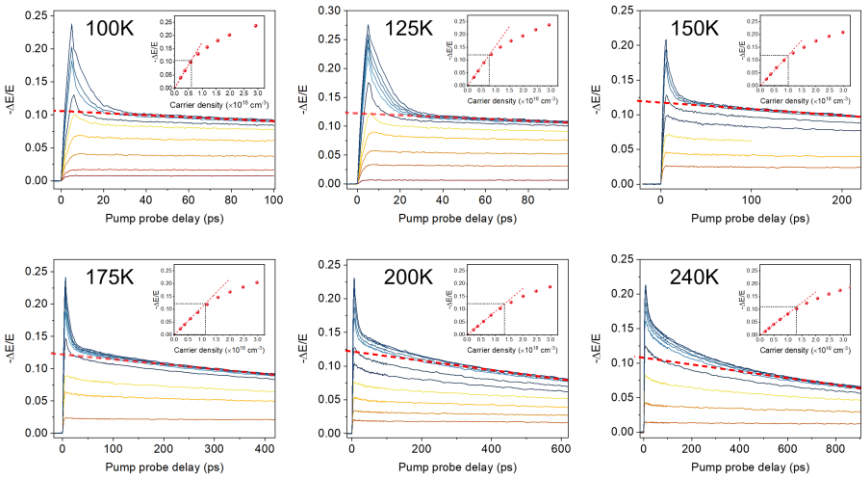

Figure 4.A.7 | Temperature-dependent OPTP dynamics of $CsPbI_3$. The fluence-dependent OPTP dynamics and the extraction of critical density at different temperatures for $CsPbI_3$.

Section 4.A.9: The photon-to-carrier conversion ratio at different temperature

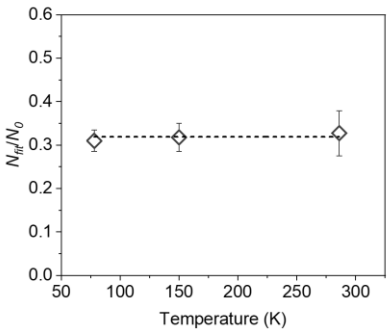

Figure 4.A.8 | Temperature-dependent photon-to-carrier conversion efficiency for $CsPbI_3$. The ratio of extracted carrier density N_{Fit} from Drude fitting to the incident photon density N_0 at different temperatures in black γ-$CsPbI_3$.

---

5 Highly mobile hot holes in $Cs_2AgBiBr_6$ double perovskite

Highly mobile hot charge carriers are a prerequisite for efficient hot-carrier optoelectronics requiring long-range hot carrier transport. Yet hot carriers are typically much less mobile than cold ones as a result of heightened carrier-phonon scattering. Here, we report enhanced hot carrier mobility in $Cs_2AgBiBr_6$ double perovskite. Following photo-excitation, hot carriers generated with excess energy exhibit boosted mobility, reaching a 4-fold enhancement compared to cold carriers at an excess energy of ~1.5 eV and a long-range hot-carrier transport length beyond 200 nm. By optical pump-IR push-Terahertz probe spectroscopy and frequency-resolved photoconductivity measurements, we provide experimental evidence that the conductivity enhancement originates primarily from hot holes which experience reduced momentum scattering compared to their cold states. We rationalize our observation by considering (quasi-)ballistic transport of thermalized hot holes with energies above an energetic threshold in $Cs_2AgBiBr_6$. Our findings render $Cs_2AgBiBr_6$ a fascinating platform for studying the fundamentals of hot carrier transport and its exploitation towards efficient hot carrier-based optoelectronic devices.

5.1 Introduction

Optical excitation of semiconductors by photons with energy ($h\nu$) exceeding their bandgap (E_g) creates energetic, "hot" carriers with an excess energy $E_{ex} = h\nu - E_g$. These initially non-thermalized hot carriers can reach thermalization with a defined electronic temperature following the Fermi-Dirac distribution via carrier-carrier interactions in tens to hundreds of femtoseconds (fs) [182,183,184]. The thermalized hot carriers can subsequently dissipate their excess energy to the lattice, becoming "cold" carriers at the band-edge within a few picoseconds (ps) in most conventional semiconductors [43,85]. The ultrafast energy loss during hot carrier cooling represents one of the major loss channels for solar cells, limiting the energy conversion efficiency to ~33.7% (so-called Shockley-Queisser limit) [6,80]. Harvesting hot carriers before their relaxation is a much sought-after goal for achieving efficient optoelectronics, specifically photovoltaics [185,186]. One of the main challenges is the relatively short transport length of hot carriers before dissipating their excess energy to the environment. This is due to the typically short hot-carrier lifetimes combined with significantly reduced mobilities of hot charge carriers resulting from the enhanced momentum scattering rates, as reported in

conventional semiconductors (e.g., Si and GaAs) [85,86,187].

Recent reports on remarkably long-lived hot carriers (with lifetimes over 100 ps) in lead halide perovskites have attracted enormous interest in exploiting hot carriers for fundamental research, as well as developing efficient hot carrier-based optoelectronic devices [43,44]. In addition to the lifetime, some recent ultrafast spectroscopic studies on perovskites have reported fascinating hot carrier transport properties on (sub-)ps timescales following light absorption and charge generation. For instance, Sung *et al*. [46] have reported that hot carriers can propagate over 150 nm within 20 fs upon photon absorption in a methylammonium lead iodide system applying transient absorption microscopy, providing experimental evidence for ballistic transport (i.e., charge transport without scattering) of hot carriers on a sub-20 fs time scale. For the transport of relatively long-lived hot carriers from sub-ps to tens of ps, different and even contradictory spectroscopic results have been reported. For instance, using the same techniques as Sung *et al.* [46] with however a lower time resolution (over 300 fs), Guo *et al*. [45] observed a quasi-ballistic transport in $MAPbI_3$ over 200 nm in the first 300 fs, followed by a diffusive transport regime of nonequilibrium hot carriers persisting for tens of ps over a distance of 600 nm. Such ultrafast, long-range transport seems to imply higher mobility for hot carriers than for cold ones. On the other hand, combining transient absorption (TA) and Terahertz (THz) spectroscopy, Monti *et al*. [188] reported that, while hot carriers indeed show a long lifetime over 100 ps in a mixed Pb-Sn halide perovskite as observed by TA, time-resolved THz spectroscopy shows no difference in photoconductivity between hot and cold carriers. This led to the conclusion that hot carriers display mobilities similar to cold carriers. Clearly, hot carrier transport properties in metal halide perovskites, especially the transient hot carrier mobility, have so far remained elusive and merit further investigation.

Among the metal halide perovskites, $Cs_2AgBiBr_6$ double perovskite has emerged as a promising alternative to toxic, unstable lead halide perovskites for various optoelectronic applications owing to its outstanding chemical stability, nontoxicity, and outstanding optoelectronic properties, e.g., long carrier lifetimes [59,189], and large carrier diffusion lengths [60,190]. In particular, $Cs_2AgBiBr_6$ double perovskite has shown exceptional performance for high-energy photon detection applications: for instance, it exhibits excellent X-ray detection with a low detection limit [58,140,189]. Therefore, a study of hot carrier transport in $Cs_2AgBiBr_6$ double perovskites following high-energy photo-excitations is of great fundamental interest and could provide insights into their further optoelectronic applications.

Here, employing optical pump-THz probe (OPTP) spectroscopy, we observe anomalously high transient mobility of hot carriers within the first ~3 ps after photo-injecting hot carriers in $Cs_2AgBiBr_6$ double perovskites. This contrasts with conventional semiconductors, where hot carriers possess lower mobilities than those of band-edge states due to enhanced electron-

phonon scattering. By optical pump-IR push-THz probe (PPP) spectroscopy, we provide further experimental evidence that highly mobile hot holes, rather than hot electrons, are primarily responsible for the observed high transient mobility in $Cs_2AgBiBr_6$ double perovskites. Furthermore, frequency-resolved photoconductivity measurements reveal that the high mobility of charge carriers in the hot states originates from reduced momentum scattering events, i.e., longer scattering time. We rationalize our observation by including (quasi-)ballistic transport of the thermalized hot holes with sufficient kinetic energy in $Cs_2AgBiBr_6$. Our results render $Cs_2AgBiBr_6$ double perovskites an interesting platform for hot-carrier studies for both fundamental physics and device applications, exploiting their high mobility.

5.2 Materials

Double perovskite $Cs_2AgBiBr_6$ preparation and characterization

$Cs_2AgBiBr_6$ single crystals were grown via controlled cooling. A mixture of 1.0 mmol of $BiBr_3$ (≥98%, Sigma-Aldrich) and 2.0 mmol of CsBr (99.9%, Sigma-Aldrich) in 10 mL of HBr (≥99.99%, 48 w%, Honeywell Fluka) in a 40 mL vial was sonicated for 5 min. After adding 1.0 mmol AgBr (≥99%, Chem-Lab), the suspension was sonicated for 5 min and then heated to 120 °C to obtain a supersaturated solution. The mixture was cooled according to the following protocol: First, it was kept at 120 °C for 3 h, then cooled by 2 °C h^{-1} to 100 °C, and further by a lower cooling rate of 1 °C h^{-1} to 50 °C. After that, mm-sized single crystals could be collected from the mixture by filtration. The crystals were washed with isopropanol (HPLC grade, Sigma-Aldrich) and then dried in a vacuum oven at 60 °C. The synthesis was performed under ambient atmospheric conditions. For the optical measurements, a 0.5 M solution of the crystals in dimethylsulfoxide (DMSO) was spin-coated on top of fused silica substrates (1 cm ×1 cm), resulting in uniform films with a thickness of ~200 nm. The samples are characterized by UV-vis spectroscopy, X-ray diffraction, and atomic force microscopy.

5.3 Results and Discussion

A schematic illustration of the $Cs_2AgBiBr_6$ double perovskite crystal structure is shown in **Figure 5.1a**. At room temperature, $Cs_2AgBiBr_6$ possesses a cubic phase, in which the monovalent Ag^+ and trivalent Bi^{3+} cations are centered alternately in each of the octahedra that consist of six monovalent Br^- anions [191]. The Cs^+ cations are situated in the corner-shared cuboctahedral cavities. **Figure 5.1b** illustrates the X-ray diffraction (XRD) pattern of the prepared $Cs_2AgBiBr_6$ double perovskite thin film. All peaks are in good agreement with theoretical calculations and previous experimental results for $Cs_2AgBiBr_6$, ruling out the presence of other phases and unreacted precursors in the synthesized sample [192,193].

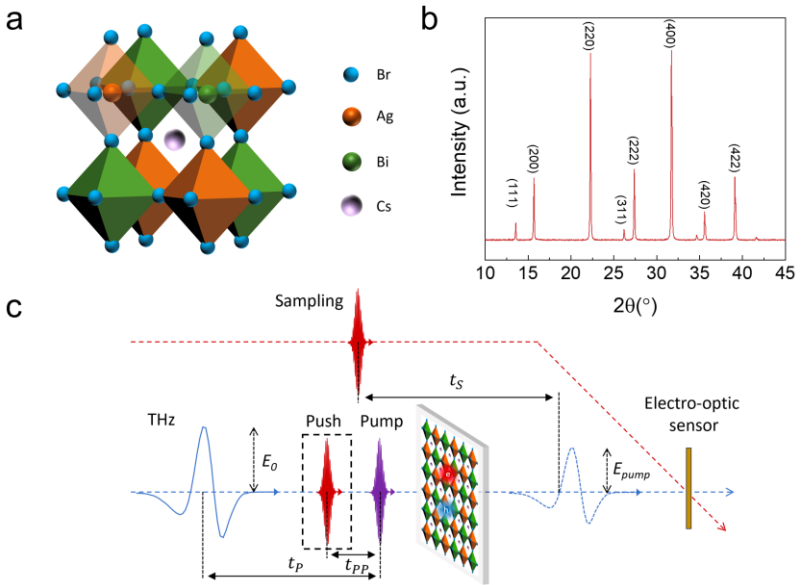

Figure 5.1 | Sample characterization and THz spectroscopy setup. (a) Atomic structure and **(b)** XRD pattern of the $Cs_2AgBiBr_6$ double perovskite; **(c)** Experimental layout for optical pump - THz probe (OPTP), or optical pump - IR push - THz probe (PPP) spectroscopy. The push pulse (marked in red in the dashed box) can be selectively switched on and off depending on the measurement mode. For the OPTP studies (by blocking the push pulse), the setup measures the pump (the purple pulse) induced THz field absorption to quantify the photoconductivity dynamics of the excited charge carriers by controlling the pump-probe delay t_P. The electric field of the transmitted THz pulse through the sample (the blue dashed pulse) is measured via free-space electro-optic sampling in a ZnTe crystal (the orange rectangle) by a third short pulse (~800 nm, with a duration of ~100 fs; the top red pulse), controlling the delay between the sampling and the transmitted THz pulse t_S. For the PPP studies, the push pulse (bottom red) is switched on at a controlled pump-push delay time t_{PP} to re-excite the system.

To investigate the dynamics and transport properties of hot carriers following optical excitation, we employ ultrafast, contact-free THz spectroscopy, as illustrated in **Figure 5.1c**, to directly monitor the photoconductivity of the charge carriers with ~200 fs time resolution. The setup can be operated in two measurement modes: the normal mode for OPTP spectroscopy, and a customized mode for PPP spectroscopy by introducing a second excitation beam (i.e., push) at a tunable pump-push delay t_{PP}. For the PPP experiment, a push pulse in the near-IR range (1.55 eV here) re-excites the charge carriers from the cold states at the band-edge to hot states, at a controlled pump-push delay time t_{PP}.

Observing highly conductive hot carriers by OPTP measurements

In **Figure 5.2a**, we show the UV-vis absorption spectrum of a $Cs_2AgBiBr_6$ crystalline thin film used for THz spectroscopy studies with a thickness of approximately 200 nm characterized

by atomic force microscopy (see **Figure 5.A.1**). $Cs_2AgBiBr_6$ is an indirect semiconductor with a band-edge absorption involving an *X*-*L* transition in the momentum space [62,194]. Using a Tauc plot, we infer an indirect bandgap of ~2.17 eV (see **Figure 5.A.2**), falling into the range of previously reported values (from 1.83 eV to 2.25 eV) [139,195]. The THz transmission through the unpumped sample is shown in **Figure 5.A.3**. The selected pump wavelengths for OPTP measurements are denoted with dashed lines in the absorption spectrum in **Figure 5.2a,** spanning from the near band-edge (with *hv* ~2.43 eV) to the high energetic states in the conduction/valence band (with *hv* up to ~3.65 eV). To avoid higher-order recombination processes (e.g., Auger recombination), we excite the sample with relatively low fluence (~10^{13} photons/cm^2). Within the applied range of fluences, the photoconductivity shows a linear dependence on the fluence, as shown in **Figure 5.A.4**.

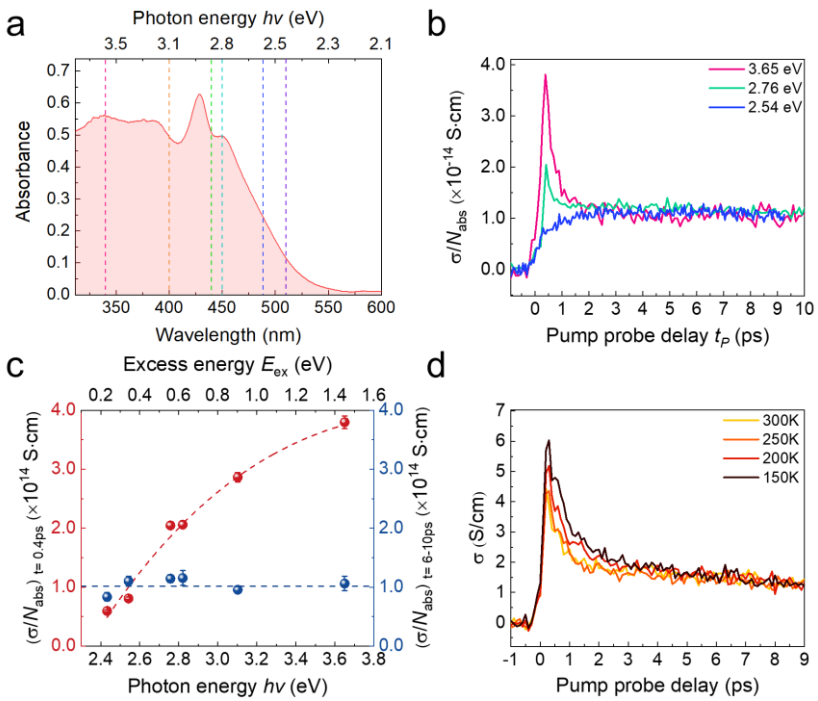

Figure 5.2 | Photon energy- and temperature-dependent photoconductivity dynamics. (a) Absorption spectrum of $Cs_2AgBiBr_6$. The vertical dashed lines indicate the pump wavelengths used in the OPTP measurements. **(b)** Pump photon energy (*hv*)-dependent photoconductivity σ, divided by the absorbed photon density, N_{abs}, as a function of pump-probe delay time t_P for three exemplary excitation energies. **(c)** The photoconductivity at t_P = 0.4 ps (at which the photoconductivity reaches a maximum for above-2.76 eV excitations in Figure 2b) (left axis and red data points) and the average value from 6 to 10 ps for each photon energy (right axis and blue data points), as a function of the pump photon energy (bottom axis) and excess energy (top axis). The dashed lines are guides to the eyes. The error bar represents the uncertainty in the fluence measurements for quantifying the absorbed photon density and the measurement noise level.

(d) Temperature-dependent photoconductivity dynamics, following excitation at 3.1 eV with a fluence of 2.91×10^{14} cm^{-2}.

To unveil the role of the excess energy on hot carrier dynamics, we compare the photoconductivity of $Cs_2AgBiBr_6$ divided by the absorbed photon density, N_{abs}, following optical excitations with different photon energies. Here the real part of the photoconductivity is measured by monitoring the pump-induced absorption at the peak of the THz field [106,196]. In principle, the time-resolved photoconductivity $\sigma(t_P)$ is determined by the product of the carrier density $n(t_P)$ (with $n(t_P = 0) \propto N_{abs}$) and charge mobility $\mu(t_P)$ in the sample: $\sigma(t_P) = \mathrm{e} \cdot n(t_P) \cdot \mu(t_P)$. As shown in **Figures 5.2b** and **5.2c**, we reveal an intriguing difference between dynamics for excitations with photon energies above and below 2.76 eV (see all the photo-excitations in **Figure 5.A.5**). When the pump photon energy, *hv,* is below ~2.7 eV (e.g., for excitations at 2.43 and 2.54 eV), the photoconductivity shows a gradual increase during the first 2-3 ps, followed by a plateau for 10s of ps. We note that the rise in photoconductivity is much slower than the time resolution of the setup (~ 200 fs). Similar photoconductivity dynamics in lead halide perovskites following close-to-band-edge excitations have previously been assigned to polaron formation [142,166], during which the charge scattering rate is reduced. In line with such assignment, recent studies have also reported polaron formation in $Cs_2AgBiBr_6$ double perovskites in the first few ps [192,193]. During polaron formation, the effective mass of charge carriers is expected to increase, lowering the charge mobility. Simultaneously, the momentum scattering time of the charge carrier can be, however, substantially increased due to the screening protection of the polaron states, balancing out the effect of the enhanced effective mass on the charge carrier mobility [44,63,197]. The slow rise of the photoconductivity indicates that the formed polarons are more mobile than the nascent carriers near the band-edge, primarily due to the substantially reduced scattering rate. On the other hand, for hv > 2.7 eV, the photoconductivity exhibits a swift rise within a few hundred of fs, dropping in the following ~2-3 ps to a constant conductivity. In **Figure 5.2c**, we summarize the photoconductivity amplitude at ~ 0.4 ps (at which photoconductivities with hv > 2.7 eV show a peak), and the averaged plateau value from 6-10 ps, as a function of photon energy hv and excess energy E_{ex}. Remarkably, despite the distinctive dynamics in the first 3 ps, the photoconductivity ultimately reaches, within experimental uncertainty, the same value for all excitation wavelengths. The identical $\frac{\sigma}{N_{abs}}$ value ($\propto n(t_P) \cdot \mu(t_P)$) from 3 to 10 ps suggests that photo-excited charge carriers do not recombine in the first 3 ps via, e.g., charge trapping. Instead, the result indicates that (i) the photon-to-charge conversion efficiency, i.e., the quantum efficiency of charge generation, is independent of excitation wavelength; (ii) the charge carriers reach the same final polaron states ~3 ps after excitation; (iii) above a photon energy threshold

of ~2.7 eV, a short-lived enhanced photoconductivity is observed, increasing in amplitude with increasing photon energy. The intriguing charge carrier dynamics transition at ~2.7 eV is drastically different from previously reported photoconductivity dynamics for lead-based halide perovskites, in which the charge carrier dynamics are consistently characterized by a fast, sub-ps to ps rise followed by a long-lived photoconductivity plateau [142,166] (similar to the dynamics following 2.54 eV excitation as shown in **Figure 5.2b**).

After establishing that polarons are formed independent of the excitation pathways, we now turn to the initially enhanced photoconductivity decaying within 3 ps. As the charge population remains unchanged in this time window, our result suggests a higher mobility of hot carriers than that of the final polaron states. As plotted in **Figure 5.2c**, the peak mobility of hot carriers increases with the pump excess energy, indicating a correlation between high energy states and the high mobility of hot carriers. For $h\nu$ = 3.65 eV (excess energy of ~1.5 eV), the peak mobility of the hot carriers reaches an almost 4 times higher value than that of cold carriers. In conventional semiconductors, hot carriers experience enhanced momentum scattering and thus possess a lower mobility [85,86,187]. To further confirm the conductive nature of hot carriers in $Cs_2AgBiBr_6$ double perovskite, we conduct temperature-dependent photoconductivity measurements as shown in **Figure 5.2d**. Here we limit the measurement range from 150 to 300 K, to avoid the phase transition of $Cs_2AgBiBr_6$ at 122 K [191]. At low temperature, we observe a higher peak photoconductivity due to a slowdown of hot carrier thermalization and cooling (quantified in **Figure 5.A.6**). We can rule out the temperature-induced absorption changes as the primary origin for the observed enhanced photoconductivity at low temperature, as previous studies reported minor changes in the bandgap of double perovskites while lowering the temperature down to cryogenic temperatures. Furthermore, to provide direct support for such a claim, we measure and analyze frequency-resolved photoconductivity at 5 ps following optical excitation, as shown in **Figure 5.A.8**. The charge carrier density is found to be nearly identical based on Drude-Smith analysis for both 300 and 150 K (manifested by the identical plasma frequency in **Table 5.A.1**). From the long-time (~10 ps) signal, it is evident that the conductivity of equilibrated polarons is temperature-independent over the employed temperature range, possibly due to impurity scattering.

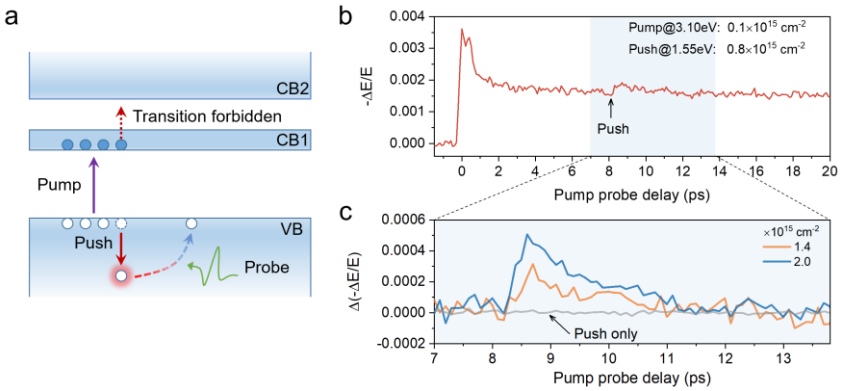

Figure 5.3 | PPP spectroscopy. (a) Schematic illustration of PPP measurements. The photon energies for pump and push pulses are 3.1 eV and 1.55 eV, respectively. **(b)** Pump-push induced photoconductivity transient with the corresponding incident photon density of 0.1×10^{15} cm^{-2} and 0.8×10^{15} cm^{-2}. The push pulse arrives ~8.2 ps after the pump pulse. **(c)** The push-fluence-dependent double-differential photoconductivity with a fixed incident pump photon density of 0.1×10^{15} cm^{-2}. The grey line shows the push-only photoconductivity transient without a pump but with a push photon density of 1.6×10^{15} cm^{-2}.

Highly mobile hot holes revealed by the PPP spectroscopy

To unambiguously confirm the high mobility of hot carriers with photon energy above 2.76 eV and to further disentangle the conductivity contributions from hot electrons and holes, we conduct optical pump-IR push-THz probe (PPP) experiments [198]. In these experiments, we photo-generate charge carriers following 3.1 eV excitations. After the hot carrier cooling and relaxation into the polaron states (within 3 ps), we re-excite the cold carriers by an IR pulse with a photon energy below the bandgap of $Cs_2AgBiBr_6$ (2.17 eV). Based on the previously reported band structure, the conduction band possesses a gigantic band splitting (over 1.8 eV at the *L* point, the conduction band minimum), due to strong spin-orbit coupling in $Cs_2AgBiBr_6$, while no such splitting is observed in the valence band. Furthermore, the density of electronic states in the valence band is much higher and more extended than that of the conduction band [62,199]. Here, we select 1.55 eV excitation as the push pulse to selectively re-excite only cold holes, as shown schematically in **Figure 5.3a**. In **Figure 5.3b**, following the push excitation at ~8.2 ps after the pump pulse, we observe a transient increase of photoconductivity. The conductivity enhancement by the push increases with the fluence of push pulses, at a constant incident pump fluence of 1×10^{14} cm^{-2}, as illustrated in **Figure 5.3c**. The lifetime of the increased photoconductivity is consistent with the hot carrier cooling time following the first excitation. We exclude the contribution of two-photon absorption to the photoconductivity in our study by blocking the first 3.1 eV pump: with only the push pulse as the excitation, we do not observe any photoconductivity signal (with a fluence of ~ 1.6×10^{15} cm^{-2}), as seen in **Figure 5.3c**. As

only cold holes can be re-excited by the push pulse, we conclude that hot holes have higher mobility than the corresponding cold ones. Combined with the band structure, this result can explain the observed photoconductivity transition at $h\nu > 2.7$ eV. The first direct band transition (at the X symmetry point) in double perovskites is around 2.8 eV [194,200,201]. When exciting the sample with $h\nu = 2.43$ eV and 2.54 eV, the excess energy of the photons will primarily end up in the hot electrons due to the relatively flat first conduction band. The observed slow rise of the photoconductivity implies that (with a relatively low excess energy of ~ 0.4 eV), hot charge carriers are less mobile than the cold ones. For $h\nu > 2.7$ eV, due to the continuous, high density of hole states in the valence band, excess energy in pump photons will predominantly go into hot holes. This leads to a transient enhancement of photoconductivity due to the highly mobile hot holes.

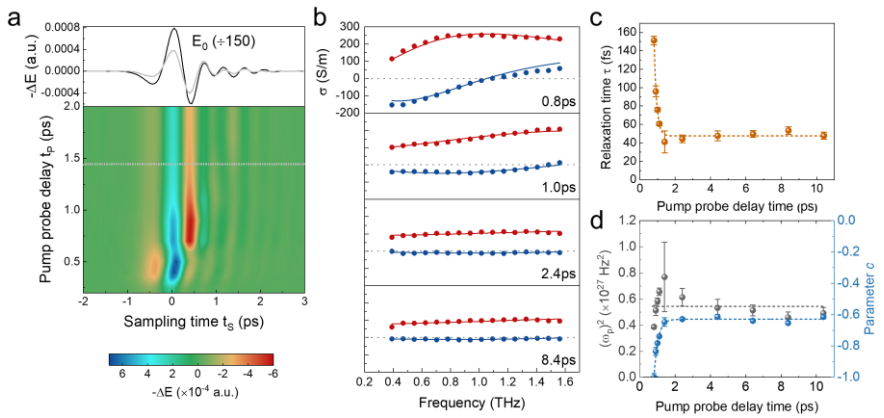

Figure 5.4 | Frequency-resolved THz photoconductivity spectra. (a) Pseudocolor representation of the two-time resolved THz electric field change $-\Delta E$, with a pump excitation wavelength of 400 nm, and an absorbed photon density of ~1.02×10^{14} cm^{-2}. All data are measured at a fixed pump-sampling delay time by moving the pump and sampling stages simultaneously (See supplementary material for more details). The grey line in the upper panel shows an example of $-\Delta E$ at a fixed t_P, corresponding to the grey dotted line in the bottom panel. The black line is the transmitted THz electric field through the unexcited sample. **(b)** The complex frequency-resolved photoconductivity measured at various pump-probe delay times t_P (at 0.8 ps, 1.0 ps, 2.4 ps, and 8.4 ps, respectively). The red and blue dots represent the real and imaginary components, respectively, of the measured complex photoconductivity; the corresponding solid lines represent the Drude-Smith description as discussed in the main text. **(c, d)** The inferred charge relaxation time τ and square of the plasma frequency and parameter c, respectively, from the Drude-Smith model as a function of t_P. The dashed lines serve as a guide to the eye.

Significantly reduced scattering rate of hot carriers demonstrated by frequency-resolved photoconductivity spectra

To gain more insight into the highly mobile hot carriers in double perovskites, we further

analyze the time evolution of hot carrier transport properties by recording photoconductivity spectra at various delay times (see **Section 5.A.7** in Appendix). Since the photoconductivity change is faster than the THz pulse duration in our case, extra care needs to be taken to track the pump-induced THz changes in the time domain [106,114]. Here to conduct time-domain spectroscopy (TDS) in our rapidly decaying photoconductivity dynamics (in the first 2-3 ps), we record the time evolution of the probing THz pulse by moving the pump and sampling stages simultaneously, at a given pump-probe delay. In this way, one can ensure that different parts of the terahertz pulse 'see' the same transient photoconductivity. In the Appendix, we detail this measurement protocol and discuss its pros and cons over the TDS measurement protocol in which only the sampling pulse delay stage is moved. **Figure 5.4a** shows the early time evolution of the time-resolved THz electric field change $-\Delta E$ induced by 3.1 eV photo-excitation with an absorbed photon density of ~1.02×10^{14} cm^{-2}. The buildup of the ps free carrier conductivity is stabilized in phase at ~0.7 ps, while changing only in intensity afterward. As a representative example, **Figure 5.4b** shows a series of real and imaginary components of the complex photoconductivity at different pump-probe delay times. One potential limitation of our TDS measurement protocol is that the sample conductivity should not be strongly dispersed, to ensure that the response can be approximated by a delta-function in the time domain [202]. For highly dispersive photoconductivity, the THz pulse passing through the photo-excited samples may become distorted, i.e., different frequency components will be delayed in time relative to one another. For this reason, we constrain our data analysis from 0.8 ps onwards, where the dispersion in the photoconductivity is limited. In the Appendix, we further justify our choice of the time range for data analysis with extended discussions. The frequency-resolved photoconductivity can be well parameterized by the Drude-Smith (DS) model.

As demonstrated in **Figure 5.4b**, the photoconductivity dispersion evolves between 1-3 ps. The Drude-Smith parameterization allows quantifying this trend by displaying the parameter c and the DS relaxation time τ in **Figures 5.4c-d**. The dispersion of the conductivity changes strongly from $c \approx -1$ and $\tau \approx 150$ fs for hot carriers at 0.8 ps following the excitation to $c \approx -0.63$ and $\tau \approx 50$ fs for cold carriers (established after ~2 ps). Note that the DS relaxation time τ is different from the momentum scattering time τ_D following the Drude model [117]. On the other hand, τ and τ_D are positively correlated [117], so that τ reflects the trend of the time evolution of the charge momentum scattering time. Clearly, the higher mobility of hot carriers is primarily due to the overall longer scattering time of the charged species. Interestingly, we observe that the value of parameter c is close to -1 for initial hot carriers exhibiting a long charge scattering time. This observation can be understood as follows: hot carriers can traverse, between scattering events, a relatively long distance comparable to or exceeding the grain size or film thickness (both around 200 nm). As such, the probability for preferential backscattering

of hot carriers is larger than that of cold ones, explaining the variation in the *c* parameter. This also indicates that the hot carrier transport length can be larger than 200 nm. The inferred plasma frequency ω_p is constant within experimental uncertainty, indicating no substantial time-dependent variation in effective mass. Describing the conductivity with a fixed $\omega_p{}'$ yields no change in the general trend for τ (see **Figure 5.A.8**). The ratio of charge relaxation times between hot and cold carriers coincides with the ~3-fold higher mobility of hot carriers than cold ones, as shown in **Figure 5.2c** for a pump wavelength of 400 nm, i.e., photon energy of 3.1 eV. Therefore, both the amplitude and dispersion of the hot carrier conductivity indicate higher mobility of hot carriers compared to cold ones in this double perovskite due to a reduced scattering rate experienced by hot carriers. Assuming $\tau_D \approx \tau = 150$ fs and $m^* = 0.35m_0$ [140], we estimate a remarkably high transient hot carrier mobility of 750 $cm^2V^{-1}s^{-1}$.

The observation of highly mobile hot carriers with reduced scattering rates in double perovskites can be accounted for by (quasi-)ballistic transport of thermalized hot carriers with sufficiently high kinetic energies. Hot carrier thermalization in Pb-based organic-inorganic perovskites has been reported to occur in an ultrafast, sub-150 fs time scale due to efficient carrier-carrier scattering [184]. In principle, the thermalization process in perovskites is governed by efficient carrier-carrier scattering, and its scattering rate is expected to scale with $1/\varepsilon^2$ (with ε as the optical dielectric constant). As ε for both conventional Pb-based organic-inorganic perovskites and $Cs_2AgBiBr_6$ falls into a similar range (~5-7) [184,192], no substantial difference in thermalization time for both systems is expected. Therefore, one might expect a photoconductivity peak following the thermalization process 100-200 fs after optical excitations. In our THz studies, we probe the averaged photoconductivity, scattering, and thus mobility of charge carrier ensembles (including both electron and hole contributions) during the cooling process. For electrons, we expect the same photoconductivity rise as observed for other classes of perovskites [142,188]. The slightly delayed "apparent" photoconductivity peak at 400 fs may be rationalized by taking into account the time-dependent photoconductivity contributions from both hot electrons and holes. The high conductivity of the early charge species following excitation and internal carrier thermalization, originates from a highly energetic hot carrier population with sufficiently high kinetic energy, which can undergo (quasi-)ballistic transport [45,46]. With increasing pump photon energy, for a given absorbed photon density as shown in **Figure 5.2b**, the fraction of hot carriers above an excess energy "threshold" for (quasi-)ballistic transport increases, leading to an increase in the transient hot carrier conductivity. Such a photoconductivity enhancement gradually reaches saturation (as shown in **Figure 5.2c**), which may be attributed to the saturation in the electron temperature by increasing the pump photon energies (See section **5.A.10** in the Appendix). During the cooling process (within 2-3 ps), the density of highly energetic hot carriers for ballistic transport

decreases, and the photoconductivity drops correspondingly from the peak toward the cold carrier conductivity. Our discussion is also in line with Guo's work on excess energy-dependent long-range hot-carrier transport in $MAPbI_3$ studied by TA microscopy within the first few ps [45]. By directly measuring the terahertz photoconductivity, we are further able to provide mechanistic insights into the process: it is reduced charge scattering, rather than reduced effective mass that gives rise to the high mobility. Moreover, we identify the dominant contribution of hot holes to their enhanced mobility. In principle, both electrons and holes with sufficiently high excess energy can undergo ballistic transport. The dominant role of hot holes in governing the hot carrier mobility in $Cs_2AgBiBr_6$ may lie in a peculiar feature in the band structure: the narrow energy range in the first conduction band of double perovskites limits the energetics of hot electrons following light absorption. As such, for photo-excitation, in particular with photons with energies beyond direct band excitation (at ~ 2.8 eV), the excess energies of hot carriers distribute asymmetrically with much more energy into holes, leading to favorable (quasi-)ballistic transport conditions for hot holes.

5.4 Conclusions

To conclude, we observe an excess energy-dependent hot carrier mobility in $Cs_2AgBiBr_6$ double perovskite employing THz spectroscopy. Upon excitation by photons with an excess energy beyond ~0.5 eV, hot carriers exhibit higher mobility than cold carriers. Employing pump-push-probe spectroscopy and frequency-resolved photoconductivity measurements, we provide experimental evidence that such a mobility enhancement originates primarily from hot holes that experience reduced momentum scattering compared to their cold states. We rationalize our observation by (quasi-)ballistic transport of thermalized hot holes above an energetic threshold in $Cs_2AgBiBr_6$. Our findings render $Cs_2AgBiBr_6$ double perovskite as a fascinating platform for studying the fundamentals of hot carrier transport and its exploitation towards efficient hot carrier-based optoelectronic devices.

5.5 Appendix

Section 5.A.1: AFM characterization

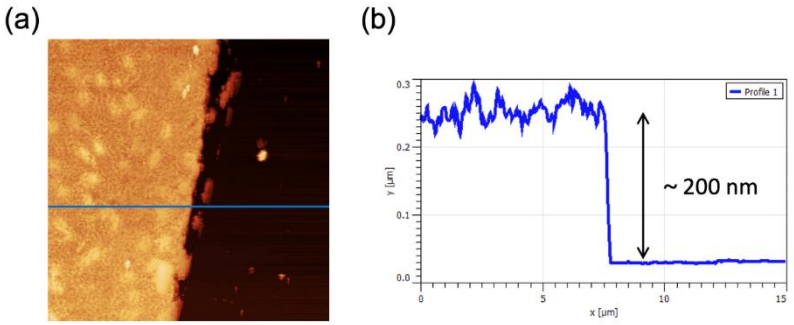

Figure 5.A.1 | AFM characterization on the $Cs_2AgBiBr_6$ double perovskite thin film. (a) AFM image on $Cs_2AgBiBr_6$ double perovskite film and **(b)** corresponding thickness measurement along the blue line in **Figure 5.A.1a**.

Section 5.A.2: Bandgap estimation

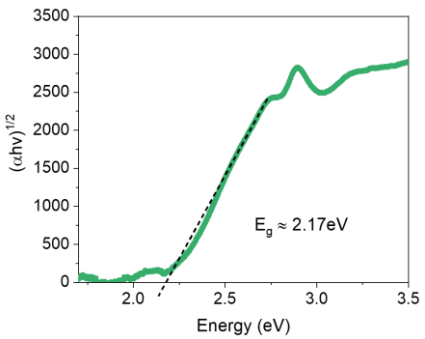

Figure 5.A.2 | Estimation of the $Cs_2AgBiBr_6$ double perovskite bandgap. Bandgap of $Cs_2AgBiBr_6$ double perovskite estimated by Tauc plot.

Section 5.A.3: THz transmission through unpumped $Cs_2AgBiBr_6$

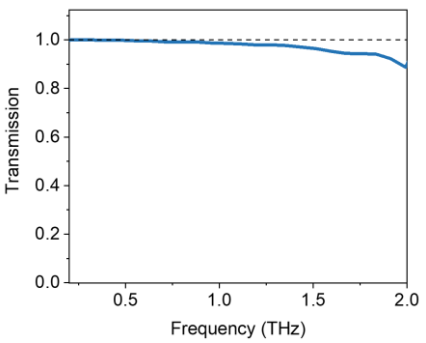

Figure 5.A.3 | Static THz transmission. THz transmission through unpumped $Cs_2AgBiBr_6$ double perovskite.

Section 5.A.4: Fluence-dependent OPTP dynamics in $Cs_2AgBiBr_6$

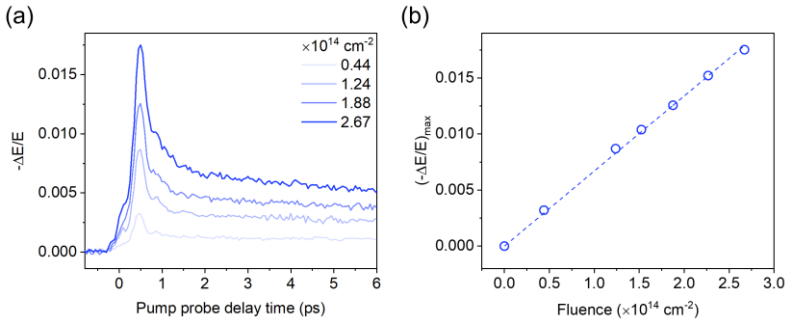

Figure 5.A.4 | Fluence-dependent OPTP dynamics. (a) Fluence-dependent OPTP dynamics measured for a pump wavelength of 400 nm (3.10 eV photon energy). **(b)** Peak intensity as a function of fluence.

Section 5.A.5: Pump photon energy-dependent OPTP dynamics normalized to the absorbed photon density

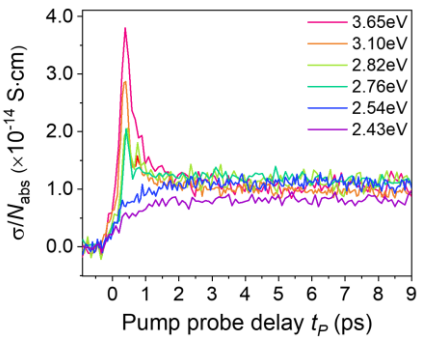

Figure 5.A.5 | Photon energy-dependent OPTP dynamics. Pump photon energy-dependent photoconductivity dynamics normalized to the absorbed photon density

---

Section 5.A.6: Temperature-dependent hot carrier lifetime

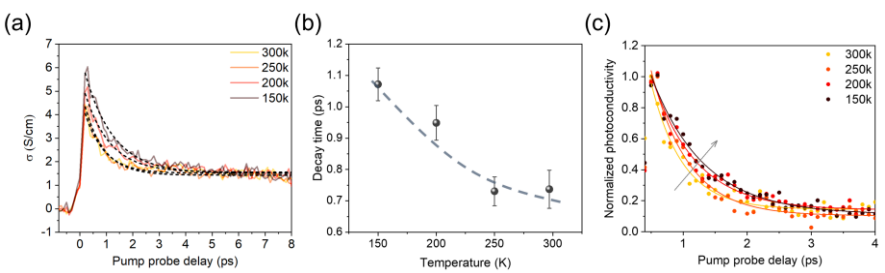

Figure 5.A.6 | Temperature-dependent photoconductivity dynamics and inferred hot carrier lifetime. (a) Single exponential fitting to the temperature-dependent hot carrier photoconductivity decay (with a constant offset). **(b)** Extracted decay time as a function of temperature. The dashed line is a guide to the

eye. **(c)** Normalized temperature-dependent fast decay dynamics and its fitting to a single exponential function. To clearly demonstrate the change in the early time, we have normalized and then fitted to the dynamics (as shown in **Figure 5.A.6a**), subtracting the long-lived offset.

Section 5.A.7: Frequency-domain THz spectra

Since the photoconductivity change is faster than the THz pulse duration in our case, extra care needs to be taken to track the pump-induced THz changes in the time domain [106,107]. Conventionally, THz time-domain spectroscopy (THz-TDS) is performed by moving only the delay stage of the sampling beam. The validity of this approach requires that the charge carriers reach a steady state in which the photoconductivity remains constant on the timescale of the THz pulse duration. For rapidly decaying photoconductivity dynamics due to charge recombination, this way of measurement may still be valid, but the extraction of frequency-resolved photoconductivity becomes more complicated, as the leading part and trailing part of a probing THz pulse interact with different amounts of charge carriers. One can ensure that different parts of the terahertz pulse 'see' the same transient photoconductivity by conducting the THz spectroscopy in such a way that the sampling pulse (the one used for electro-optic detection) and the pump pulse (the one used for the photoexcitation) are at a fixed time delay: i.e., the delay stages for pump pulse and sampling pulse move simultaneously. As there are three beams involved in the setup (THz pulse, pump pulse, and sampling pulse), this way of detection is equivalent to delaying only the THz pulse, so that the time delay between the pump and sampling pulses is fixed, for any given optical pump - THz probe delay.

There are, however, two distinct limitations in this way of performing THz-TDS measurements. Firstly, the approach only works for a temporally constant, or monotonously decreasing carrier density. When the density increases during the sampling period, the approach is no longer valid, and one cannot unambiguously infer the sample response from the recorded THz time traces [203,204]. A second requirement is that the sample conductivity should be dispersionless, so that the response can be approximated by a delta-function in the time domain [202]. For highly dispersive photoconductivity, the THz pulse passing through the photoexcited samples will become distorted: i.e., different frequency components will be delayed in time relative to one another, so that our approach (by sampling at a fixed pump-probe delay time) may fail. In our case, the photoconductivity spectra in **Figure 5.4b** show very limited dispersion, in particular for the time scale after 1.0 ps. The dynamics at 0.8 ps might, to some extent, be affected due to some dispersion shown in the spectra. On the other hand, its impact may be limited. Such a claim is partially supported by the observation that the inferred Drude-Smith relaxation time shows a very similar scaling (~3-4 times) as the photoconductivity ratio between the peak (at ~0.8 ps) and plateau (at ~3 ps) in the OPTP dynamics in **Figures 5.2b and 5.2c**.

Section 5.A.8: Comparison of plasma frequency between 300K and 150K

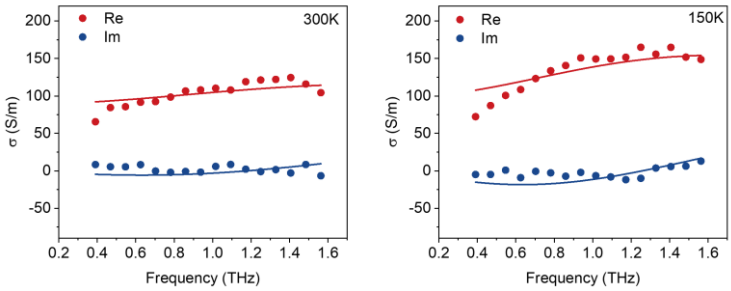

Figure 5.A.7 | Frequency-domain photoconductivity and Drude-Smith model fitting at different temperatures. Frequency-resolved photoconductivity for 300 K and 150 K measured 5 ps after the photoexcitation (400 nm). The lines are fits based on the Drude-Smith model.

Table 5.A.1 | Inferred parameters based on the Drude-Smith model.

Temperature (K)	Plasma frequency (Hz)	Scattering time (fs)	Parameter c
300	$(2.07\pm0.16)\times10^{13}$	57±9	-(0.59±0.03)
150	$(2.04\pm0.11)\times10^{13}$	73±7	-(0.67±0.02)

Section 5.A.9: Comparison of Drude-Smith fitting with and without fixing the plasma frequency

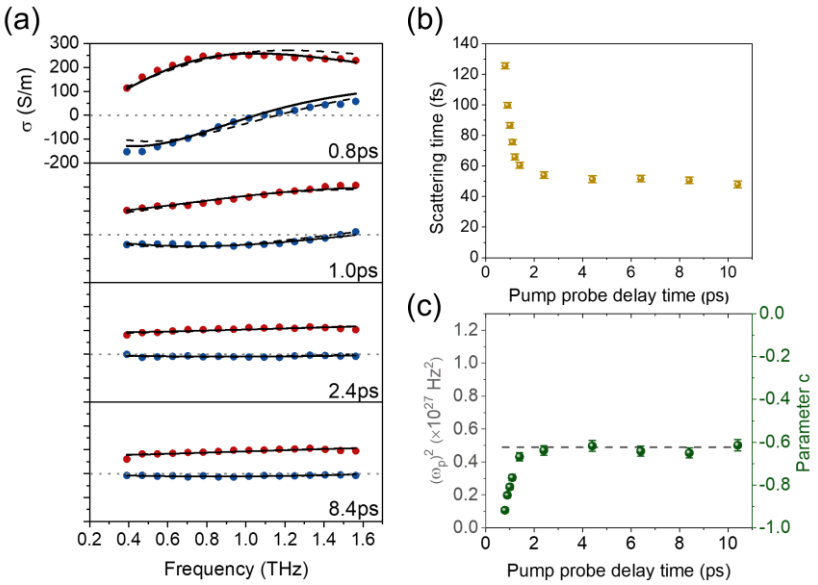

Figure 5.A.8 | Drude-Smith fitting to the frequency-domain photoconductivity and extracted parameters at different pump-probe delay times. (a) Comparison of Drude-Smith fitting to the frequency-domain conductivity measured at pump-probe delay times of 0.8ps, 1.0ps, 2.4ps and 8.4ps with (black dashed line) and without (black solid line) fixing the plasma frequency. Plots of the extracted **(b)** scattering time and **(c)** parameter c from the fitting with fixing the plasma frequency (black dashed line).

Section 5.A.10: Extended discussions on the photoconductivity saturation effect

In **Figure 5.2c** in the manuscript, the peak mobility of the hot carriers increases by increasing photon energy and seems to saturate at high enough photon energies. We attribute the saturation effect in the peak mobility to the saturation of the electronic temperature of hot carriers with increasing pump photon energy. Note that the energy relaxation rate of hot carriers critically depends on, and scales nonlinearly with the excess energy of hot carriers: the higher the excess energy, the faster the energy dissipation due to (1) enhanced density of charge states, and (2) efficient optical phonon emissions before hot carriers reach full thermalization. This effect limits the effective electronic temperature in thermalized hot carriers by increasing the pump photon energy and thus the peak hot carrier conductivity.

6 Optical switching of hole transfer in double perovskite/graphene heterostructure

Synergically combining the ultrahigh charge mobility and strong light absorption, graphene (Gr)/semiconductor heterostructures are promising building blocks for efficient optoelectronics, in particular photodetectors. Charge transfer (CT) across the heterostructure interface plays a key role in determining device efficiency and functionality. Here we report that hole transfer processes dominate the ultrafast CT across strongly coupled double perovskite $Cs_2AgBiBr_6$/graphene (DP/Gr) heterostructures following optical excitations. While holes are the primary charges flowing across interfaces, their transfer direction, as well as efficiency, shows a remarkable dependence on the excitation wavelength. For excitation with photon energy below the bandgap of DPs, the photoexcited hot holes in graphene can compete with the thermalization process and inject into the in-gap defect states in DPs. In contrast, for excitations beyond the bandgap of DP, the hole transfer direction is reversed, leading to hole transfer from the valence band of DPs to Gr. We further provide solid experimental evidence that the hot holes enhance CT transfer efficiency for both below- and above-bandgap photoexcitation regimes. The possibility of switching the hole transfer direction and thus the interfacial photogating field by photoexcitations provides a novel knob to control the interfacial charge flow across a DP/Gr heterojunction for novel optoelectronics.

6.1 Introduction

Graphene (Gr)/semiconductor heterostructures have emerged as promising building blocks for optoelectronics due to the unique combination of ultrahigh charge mobility $>10^5$ $cm^2V^{-1}s^{-1}$ [205,206] in Gr and strong optical absorption of semiconductors [207]. In particular, efficient conversion of light to electrical signals for, e.g., photodetectors, has been experimentally demonstrated in Gr-based heterostructures with various types of semiconductors as the light absorbers, including colloidal quantum dots [208,209], two-dimensional transition metal dichalcogenides (TMDs) [210] and bulk crystals [211]. Fundamentally, the device performance critically relies on both the interfacial charge transfer (CT) and recombination processes across the hybrid interfaces. While the former determines the population of charge carriers across the interfaces (i.e., the CT efficiency), the latter impacts the duration of the interfacial electrical field induced by the charge separation that gates or modulates the conductivity of Gr: the longer the charge separation, the higher the photoconductive gain for the light detection (so-called

'photogating' mechanism) [208].

From this perspective, understanding and eventually achieving complete control of interfacial charge carrier dynamics, e.g., the charge separation pathways and efficiency, the direction of the interfacial gating field, as well as the lifetime of charge separation, is of fundamental significance for improving the photodetection capabilities of Gr-based heterostructures. Combining THz and transient absorption spectroscopies, Fu *et al.* investigated the ultrafast CT process across Gr/WS_2 heterostructures by varying the excitation photon energies [212]. The authors showed that both the CT rate and mechanism can be controlled by the excitation energy of laser pulses: when only Gr is photoexcited, the energetic thermalized hot electrons can be emitted over the interfacial energy barriers and injected into WS_2 (so-called photo-thermionic emission). On the other hand, a direct excitation to the WS_2 layer results in the transfer of 'cold' electrons from the valence band of Gr to the photogenerated hole states in the valence band of WS_2 (which is equivalent to a hole transfer process from WS_2 to Gr). Such an interfacial charge transfer mechanism has also been reported by previous work based on Gr/WSe_2/Gr van der Waals (vdW) heterostructures [213], and a recent study by Trovatello *et al.* employing transient absorption spectroscopy [214]. While the excitation conditions can modulate the CT pathway and efficiency, the direction of photoexcited charge transfer is usually fixed. In the case of the Gr/WS_2 interface above, Gr loses electrons to WS_2 throughout the entire excitation energy range. Realization of switching of the CT direction by external stimuli (e.g., light or electrical gating) can provide a novel degree of freedom to tune both the CT efficiency, as well as the direction of the local gating field for light detection applications. Up to now, external switching of CT and photogating field direction has not been reported and remains to be developed.

In the last decade, the world has witnessed the rapid rise of low-temperature solution-processed lead halide perovskites (LHPs) as one of the most cost-effective optical absorbers for photovoltaics with the record light-to-electricity power conversion efficiency of more than 25% for single-junction solar cells [18]. Gr/LHP heterostructures have also been explored and have shown superior photodetection performance with an ultra-broadband photoresponse [215,216] and ultrahigh photoresponsivity [215,216]. However, the lead toxicity and chemical instability of LHPs have largely impeded their practical application and commercialization. By alternatively substituting two bivalent lead cations Pb^{2+} with mono- ($[B']^{+}$) and trivalent ($[B'']^{3+}$) metal cations, the so-called double perovskite (DP) with the chemical formula $A_2B'B''X_6$ has been successfully synthesized with extraordinary chemical stability and optoelectronic properties. Among them, one of the most promising DPs is the all-inorganic $Cs_2AgBiBr_6$ featuring strong optical absorption (from the UV-vis to the X-ray spectrum range) [58,189,199], long carrier lifetime [59,140,217] and large carrier diffusion length [60]. Characterization of

interfacial electronic coupling and charge transfer dynamics in DP/Gr heterostructures is crucial to provide the fundamentals for realizing high-performance optoelectronics (e.g., broadband photodetectors from the infrared (IR) to the UV range) and exploring new functionalities, e.g., new device schemes for X-ray detection.

In this work, we investigate the interlayer electronic coupling and photoinduced charge transfer processes in a DP/Gr heterostructure combining Raman spectroscopy, kelvin probe force microscopy (KPFM), and ultrafast time-resolved terahertz (THz) spectroscopy. We report that hole transfer across the interfaces dominates the CT mechanisms following photoexcitations, but its direction critically relies on the excitation photon energies. As illustrated schematically in **Figure 6.1**, when the photon energy is below the bandgap of DP (i.e., only the Gr layer is excited), the photoexcited hot holes are transferred from Gr to the DP. On the other hand, when the heterostructure is excited by photons with energy higher than the bandgap of DP, the hole transfer direction is reversed, taking place from the valence band of DP to Gr. The transition in the hole transfer direction results in switching the photogating field direction as well as in a change of the interlayer charge carrier recombination time. We further provide experimental evidence that by increasing the energetics of the photogenerated holes, the hole transfer efficiency is enhanced in both below- and above-bandgap photoexcitation regimes. The unique directional switching of hole transfer and its efficiency modulation by varying the optical excitation provides a novel knob to control the interfacial charge flow across a DP/Gr heterojunction for novel optoelectronics.

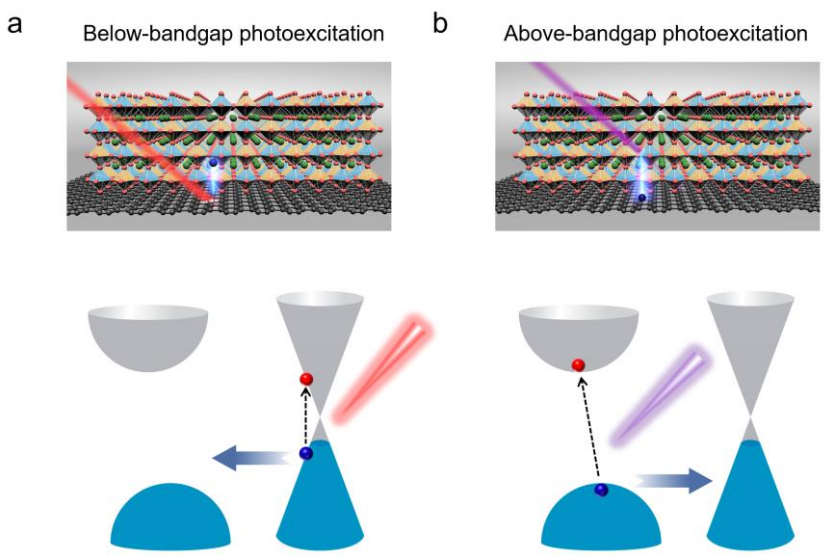

Figure 6.1 | Schematic illustration of optically controlled hole transfer dynamics in a DP/Gr heterostructure in both real (upper panel) and momentum (lower panel) spaces. (a) For the photoexcitation with photon energies below the bandgap of DP, the photoexcited hot holes in Gr are

transferred to the DP. **(b)** For the photoexcitation with photon energies above the bandgap of DP, hole transfer from DP to Gr dominates the transfer process.

6.2 Materials

Sample preparation

The DP/Gr heterostructure is prepared by first wet-transferring a chemical vapor-deposited (CVD) monolayer Gr onto fused silica, and then the Gr surface is treated by UV-Ozone for 30 minutes. We will show later that the UV-Ozone treatment is critical to realize the strong coupling and charge transfer between DP and Gr layers. Finally, we spin-coat the double perovskite solution on Gr to construct the DP/Gr heterostructures. The double perovskite sample is prepared similarly as shown in Chapter 5. A 0.5 M solution of mm-sized $Cs_2AgBiBr_6$ single crystals [140,218] in dimethylsulfoxide (DMSO) was spin-coated on top of the graphene layer on the fused silica substrate resulting in a uniform coverage with a thickness of ~200 nm.

6.3 Results and Discussion

Strong DP/Gr interlayer coupling revealed by Raman and KPFM characterizations

To achieve highly efficient CT across the hybrid interface following optical excitation, strong interlayer electronic coupling is required. We first characterize the electronic coupling between Gr and DP layers by monitoring their static charge equilibrium across interfaces (i.e., without photoexcitation) by complimentarily combining Raman spectroscopy and KPFM. While the Fermi energy E_F in Gr can be readily monitored by Raman spectroscopy, the surface potential and thus the work function of the DP can be tracked by KPFM measurements.

As shown in **Figure 6.2a**, two characteristic Raman modes centered at around 1580 cm^{-1} and 2650 cm^{-1} in bare Gr are assigned to the G-band and 2D-band [219,220]. The absence of layer-breathing modes at around 1500 cm^{-1} and 1740 cm^{-1} is indicative of monolayer Gr [219]. In addition, there is no defect-activated D-band (~1350 cm^{-1}) observed in the Gr layer before and after the DP deposition [219], suggesting the high-quality of Gr monolayer following the UV-Ozone treatment and DP deposition. Upon the deposition of DP onto Gr, both the G-band and 2D-band of Gr are blue-shifted relative to pure Gr, which is confirmed in **Figures 6.2b and 6.2c** by scanning over 36 spots within an area of 1 mm ×1 mm. G-band and 2D-band positions are reported to be sensitive to the carrier density and charge species (i.e., electron or hole) in Gr [219,220]. While the blue-shifted G-band position implies an increase in the total charge carrier density, the blue shift in the 2D-band indicates a hole population increase in Gr [220]. Given the initial p-doping nature of CVD-grown Gr transferred onto fused silica (FS) substrates [212,221], the Raman results indicate that the Fermi level E_F of Gr shifts further away from

the Dirac point, by losing electrons to the DPs. Employing the empirical relation between G-band position and Fermi energy E_F [220]: $\omega_G - 1580\ cm^{-1} = 42\ cm^{-1}eV^{-1} \cdot |E_F|$, we estimate the E_F shifts downwards substantially over 330 meV (or a total electron loss of ~8.47×10^{12} cm^{-2}) from -50 meV (corresponding to a free hole density of 1.24×10^{11} cm^{-2}) to -380 meV (equivalent to a hole density of 8.59×10^{12} cm^{-2}) below the Dirac point. The electron flow from Gr to the DP inferred from Raman spectroscopy is further captured by KPFM studies. **Figures 6.2d-6.2f** show the mapping and distribution of the surface potential of DP deposited on either fused silica (DP/FS) or Graphene (DP/Gr). As we can see, in both cases the value obtained for the area covered by the perovskite film is lower than in the case of the bare substrate. The topography of the sample was registered simultaneously to the mapping of the surface potential (**Figure 6.A.1** in the Appendix), showing a thickness of around 100-200 nm for both films. In **Figure 6.2f** we can observe the distribution for the surface potential on DP/Gr (red) and DP/FS samples (orange). As it can be seen, the surface potential for the DP/Gr samples are shifted to lower values when compared to the DP/FS samples. Based on this result, we conclude that the surface potential and thus the work function of DP on Gr is reduced in comparison to the DP on insulating silica substrates: i.e., the electron density in DP increases following interfacial charge equilibrium. Given the large amount of charge flow across the DP/Gr interface, the combined Raman and KPFM data indicate a strong interfacial electronic coupling.

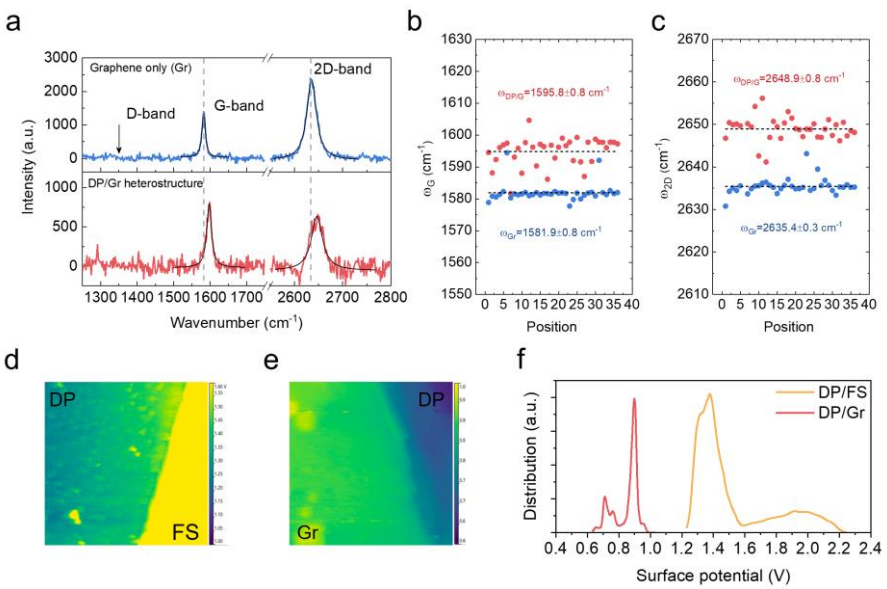

Figure 6.2 | Characterization of the interlayer Gr-DP electronic coupling by Raman spectroscopy and KPFM. (a) Raman spectra of pure Gr (upper panel) and DP/Gr heterostructure (lower panel). The solid black lines represent the Lorentz peak fittings. Spatial mapping of the **(b)** G-band and **(c)** 2D-band within

an area of 1 mm ×1 mm for pure Gr and DP/Gr. The dashed lines represent the average value for each data set. Surface potential images of **(d)** DP on fused silica substrate (DP/FS) and **(e)** DP on Gr (DP/Gr). **(f)** Distribution of the surface potential of DP/FS and DP/Gr.

Optical switching of hole transfer processes across DP/Gr interfaces

To unveil the photo-induced charge transfer dynamics in DP/Gr heterostructures, we employ contact-free, optical pump-THz probe spectroscopy as depicted in **Figure 6.3a** with sub-picosecond (ps) time resolution. The strength of OPTP spectroscopy for tracking the CT across Gr-based heterostructures relies on the extremely high charge carrier mobility μ of Gr. This leads to a substantial change in conductivity upon electron gain or loss (ΔN) in Gr following CT [209,212,222].

We first characterize the photoconductivity response from individual layers under the same pump photon energy of 3.10 eV (higher than the indirect bandgap E_g~2.1 eV of DP) and the same pump fluence of 60.9 μJ cm^{-2}. As shown in **Figure 6.3b**, photoexcitation of Gr results in a transient reduction in photoconductivity, i.e., negative photoconductivity. Such observation has been well demonstrated previously for doped Gr [223,224], and the reduced conductivity is assigned to the decrease of charge mobility. In this scenario, hot carriers generated by photoexcitation are subject to a much-enhanced momentum scattering effect in comparison to cold carriers due to the reduced screening to the scattering centers (e.g., defects) [225]. Following the cooling process of hot carriers in several ps [226], the system goes back to the initial equilibrium condition. On the other hand, excitation into the DP results in the generation of free carriers and thus positive photoconductivity. In line with our results, the long-lived carrier lifetime of more than 1 μs in $Cs_2AgBiBr_6$ has been previously reported [59]. Note here, owing to the much higher charge carrier mobility, the absolute value of photoconductivity in bare Gr is almost an order of magnitude larger than that for the bare DP upon the same pump fluence. For the same reason, the Gr's photoconductivity change following optical excitation and interfacial CT is expected to dominate the photoresponse of the system, and thus can be used as a sensitive probe to track the CT process across the DP/Gr interface.

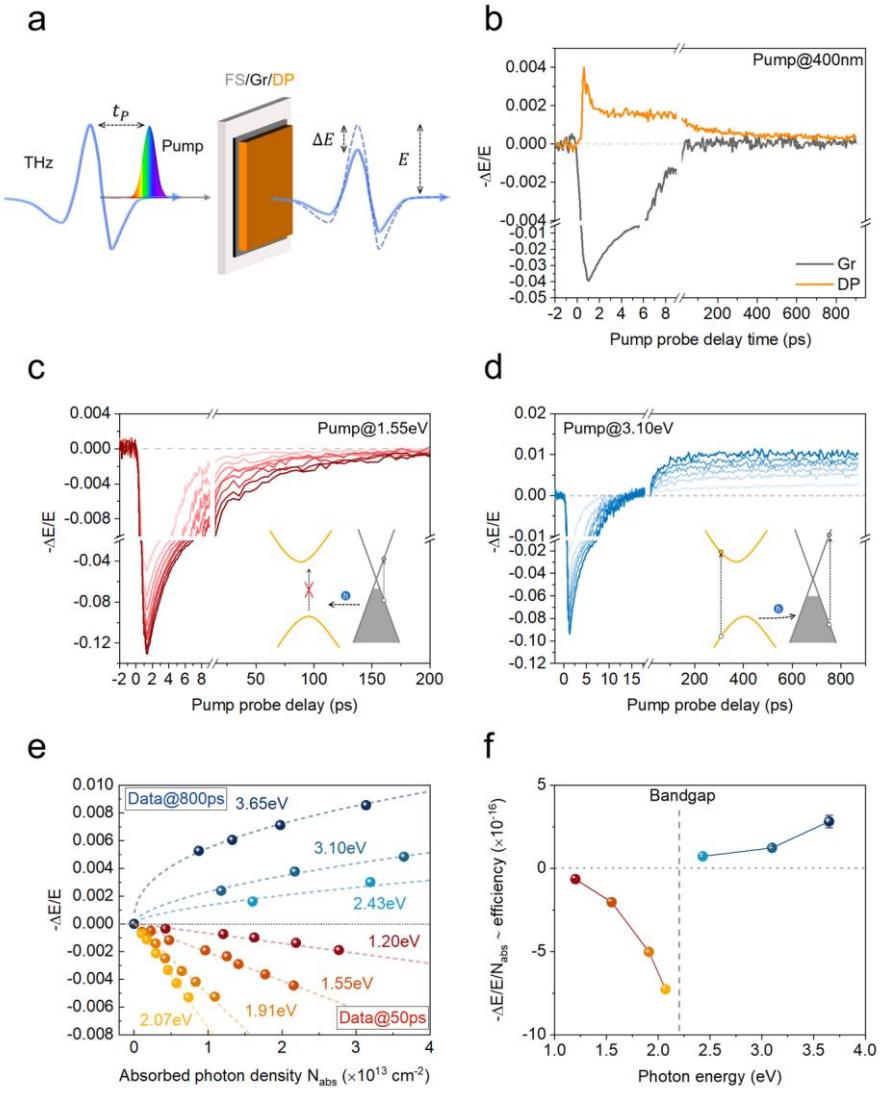

Figure 6.3 | Photoinduced charge transfer in DP/Gr heterostructures with varying incident pump photon energies. (a) Schematic of OPTP measurements. **(b)** The OPTP dynamics for pure Graphene (Gr, grey line) and double perovskite (DP, yellow line), pumped with a 400 nm (photon energy of 3.10 eV) laser pulse at a fixed fluence of 60.9 μJ cm^{-2}. **(c)** Fluence-dependent OPTP dynamics for the DP/Gr heterostructure upon 800 nm photoexcitation. The fluence increases from 24.5 μJ cm^{-2} to 233 μJ cm^{-2}. **(d)** Fluence-dependent OPTP dynamics for the DP/Gr heterostructure upon 400 nm photoexcitation. The fluence increases from 9.8 μJ cm^{-2} to 147 μJ cm^{-2}. **(e)** OPTP signal as a function of absorbed photon density for different pump photon energies. For photon energies below the bandgap of DP (~2.17 eV), the OPTP data are extracted at 50 ps after photoexcitation; for photon energies above the bandgap of DP, the OPTP data are taken at a pump-probe delay time of 800 ps. The dashed lines are guides to the eye. **(f)** The relative CT efficiency (proportional to $-\Delta E/E/N_{abs}$) as a function of pump photon energy. The vertical dashed line

indicates the bandgap of DP.

To unveil the CT pathways and mechanisms, we conduct pump photon energy-dependent and fluence-dependent OPTP measurements to the strongly coupled Gr-DP hybrids. In **Figures 6.3c-6.3d**, we present the fluence-dependent OPTP dynamics upon 1.55 eV and 3.10 eV photoexcitation as two exemplary studies. These two excitation energies are judiciously chosen to represent and compare the dynamics below and above the bandgap E_g of the DP. In both cases, the photoresponse of Gr dominates at the short time scale (i.e., the short-lived negative photoconductivity in the first few ps). On the other hand, the sign of the long-lived photoconductivity (10 ps after excitation and beyond) induced by CT critically depends on the pump-photon energy: for below-E_g excitation in **Figure 6.3c**, i.e., when only Gr is excited, we observe a negative photoconductivity with a decay time of over 100 ps, substantially longer than the sub-10 ps hot carrier cooling time in bare Gr. Considering the initial strong p-doping of Gr in contact with DP (with an E_F of -380 meV), the long-lived negative photoconductivity indicates a hole loss (e.g., electron gain) in the Gr layer, in other words, a hole transfer process from Gr to DP. In stark contrast, above-E_g excitation results in a long-lived positive photoconductivity of which the intensity increases with increasing excitation fluence as shown in **Figure 6.3d**. Due to the increased lifetime and much higher intensity compared to the signal of bare DP (see **Figure 6.A.2** in the Appendix for the direct comparison of OPTP dynamics at the same fluence for DP, Gr and DP/Gr), we confirm the long-lived positive photoconductivity stems mainly from the CT-induced conductivity changes. Furthermore, the positive photoconductivity implies a hole gain process in Gr, i.e., photogenerated hole transfer from the valence band of the DP to the valence band of Gr. Therefore, the result presented in **Figures 6.3c-6.3d** unveils a remarkable transition in the hole transfer direction, from a Gr-to-DP hole transfer for below-E_g excitations to a DP-to-Gr hole transfer for above-E_g excitations.

To further corroborate the switching in the hole-transfer direction by exciting the heterostructure across the E_g of the DP and shed light on the states involved in the CT mechanism, we conducted fluence-dependent measurements for five additional photon energies covering a wide range from 1.20 to 3.65 eV (see **Figure 6.A.3** in the Appendix). We summarize the fluence-dependent CT-induced photoconductivities in **Figure 6.3e**. For the long-lived negative photoconductivity (below-E_g photoexcitations), we take the value at 50 ps to ensure there is no contribution from the intrinsic hot carrier dynamics from Gr (which should have decayed within 10 ps). For long-lived positive photoconductivity (above-E_g photoexcitations), we extract the value at 800 ps. As we can see, these data fully support our claim of hole transfer direction switching by exciting the heterostructure across the bandgap of the DP. To the best of our knowledge, this observation represents the first control in CT direction in 2D hybrids by

external stimuli, e.g., excitation by photons of different energy in this study. More importantly, the switching of the hole transfer direction results in a photogating field flipping at interfaces by tuning pump photon energies, which could profoundly impact the photodetection mechanism in DP/Gr. Along with the switching in the hole transfer direction, we find a clear fluence dependence transition from linear to sublinear for below- and above-E_g pumps. This observation further supports the transition in the CT mechanism while tuning the excitation energy.

In this section, we discuss the states involved in the two hole-transfer regimes. For above-E_g excitations, as the holes are mainly photogenerated in the valence band of the DP, it is obvious that hole transfer takes place from the valence band of DP to the valence band of Gr. A recent spectroscopic study of a Gr/WS_2 heterojunction has proposed a similar hole transfer mechanism by time- and angle-resolved photoemission spectroscopy [227] and by a combined THz/transient absorption spectroscopic study [212]. On the other hand, for the hole transfer from Gr to DP, there is no clear indication of the nature of the accepting states in the DP (the valence band or defect states), and if thermalized (e.g. via photo-thermionic emission [213]) or non-thermalized (hot) holes are involved in the donor states. First, we can rule out the injection of thermalized hot holes from Gr to DP as the main CT mechanism. In that case, the energetic thermalized hot carriers (following the Fermi-Dirac distribution) with energies beyond the Shockley barrier can be emitted from Gr to DP. A superlinear dependence between the CT efficiency and excitation fluence is expected for such a 'photo-thermionic emission' picture [212,213] which is in contrast to the observed linear dependence here. As such, we conclude that in the below-E_g excitation regime, transfer of non-thermalized hot holes dominates the CT process. For this scenario, the CT can take place only when the excess energy of 'nascent' hot holes in Gr goes beyond the interfacial Schottky barrier, and the final efficiency of the hot hole transfer is governed by the competition between the hot hole injection rate and carrier thermalization rate. Based on the energetics of the DP and Gr, the Schottky barrier of hole injection from Gr to DPs is estimated to be ~1.0 eV (e.g., the difference between the Fermi level of graphene and the valence band maximum of DPs; see discussion in the Appendix). This indicates that no hot hole injection is expected for pump photon energies below 2.8 eV, which contrasts our observation. As such, in-gap defect states with much lower injection barriers are expected to play a critical role as the hole acceptors for below-E_g excitation. This conclusion comes as no surprise: in our combined static Raman and KPFM studies, we revealed as much as ~8.5×10^{12} cm^{-2} electrons have been injected to initially p-doped DP following static charge equilibrium, leading to a reduction in the surface potential (and thus rise in Fermi level) in the DP. These filled defects following interfacial charge equilibrium and other initial shallow defects (filled defect states close to the valence band, if any) can serve as hole acceptors for the

CT.

We further note that the switched hole injection direction by exciting the heterostructure across the E_g also leads to different charge recombination pathways and, therefore, lifetimes. A clear recombination time jumps from ~100 ps for below-E_g excitations to over 1 ns for above-E_g excitations is clearly observed. In each excitation and hole transfer regime, the recombination time is found to be pump energy and fluence independent. This observation is in clear contrast to the CT dynamics in Gr/TMDs interfaces. There, although the CT efficiency and pathways are modulated by excitation energies (photo-thermionic emission from Gr to TMDs for sub-bandgap excitation and direct hole transfer from TMDs to Gr for above-bandgap excitation), the final charge separation state and thus the recombination lifetime is observed to be identical throughout the whole excitation range.

The energetics of the hot holes impact the hole transfer efficiency

After establishing the optical switching of the hole transfer process (and thus the photogating field direction and interlayer recombination lifetime) at DP/Gr interfaces, we investigate the effect of pump photon energy, or the energetics of hot carriers, in dictating the hole transfer efficiency. Here we define the efficiency by the slope in the fluence-dependent photoconductivity plot as shown in **Figure 6.3e**, and summarize the data in **Figure 6.3f** (we keep the sign of the slope to distinguish the hole transfer direction). For above-E_g excitation, we observe a sublinear dependence of the photoconductivity on fluence, and we define the efficiency by a linear fit to the first 3 data points in the low fluence regime. Based on **Figures 6.3e and 6.3f**, it is clear that the hole transfer efficiency is much enhanced as the photon energy increases for both below- and above-E_g photoexcitation. This result provides strong evidence of a hot carrier-involved CT process. For below-E_g excitation, by increasing the pump photon energy from 1.20 to 2.07 eV, the hole transfer efficiency is boosted by almost an order of magnitude. The enhanced hot hole transfer efficiency with increasing hot hole energetics can be qualitatively understood as a combined consequence of the enhanced hot hole transfer rate (due to the enhanced driving force and the coupling strength for CT) [228], and the reduced hot carrier relaxation rate from the initial energetics to below the CT energy barrier. For above-E_g excitation (i.e., when the holes are mainly generated in the DP), besides the favorable rate competition for hot hole injection, the recently reported much enhanced hot hole transport properties (e.g., enhanced mobility) [218] could favor the hot carrier diffusion towards the interface for charge separation at DP/Gr interfaces.

Finally, to quantitatively assess the CT efficiency for both below- and above-bandgap photoexcitations, we conduct time-domain THz spectroscopy at the time scale where the charge separation reaches a quasi-equilibrium state following CT (see details in the Appendix). Based

on this measurement, we extract the frequency-resolved photoconductivity which is dominated by the Gr's free carrier response. Fitting the data by Drude model, we extract the carrier density change n in Gr with and without photoexcitation (or CT). The absolute CT efficiency, defined as the ratio of the transferred carrier density ($\Delta N = N_{pump} - N_0$) to the absorbed photon density n_{abs}: $\eta = \Delta N / n_{abs}$, is therefore obtained. For 3.10 eV excitation, we estimate a ~1% hole transfer efficiency from DP to Gr. Based on the first-order approximation (that the CT quantum yield is proportional to the relative CT efficiency shown in **Figure 3f**), we can estimate the highest CT efficiency for below-bandgap excitation at ~2 eV to be around 6%.

6.4 Conclusions

In summary, full optical control of the hole transfer mechanism and recombination processes has been achieved in strongly coupled DP/Gr heterostructures by simply tuning the excitation photon energy. We unveiled the important role of in-gap defect states and pump photon energy in tuning the interfacial hole transfer processes: we find that the nascent hot holes in Gr can be injected into in-gap defects of DP for below-E_g excitations while hole transfer from the valence band of the DP to the valence band of Gr occurs for above-E_g excitation. We provide experimental evidence that increasing the hot hole energetics facilitates interfacial hole transfer efficiency for both below- and above-E_g excitation regimes. Our results not only unveil fundamental photophysics governing interfacial CT, but also provide a new knob for controlling CT across DP/Gr heterostructures in optoelectronic applications (e.g., broadband photodetectors covering the THz up to the X-ray spectral range). In addition, the intriguing optical switching of hole transfer endows DP/Gr heterostructures a new degree of freedom for, e.g., manipulating the local gating field for new functionalities such as an optical pump-induced memory effect in Gr.

6.5 Appendix

Section 6.A.1: Topographic and surface potential images

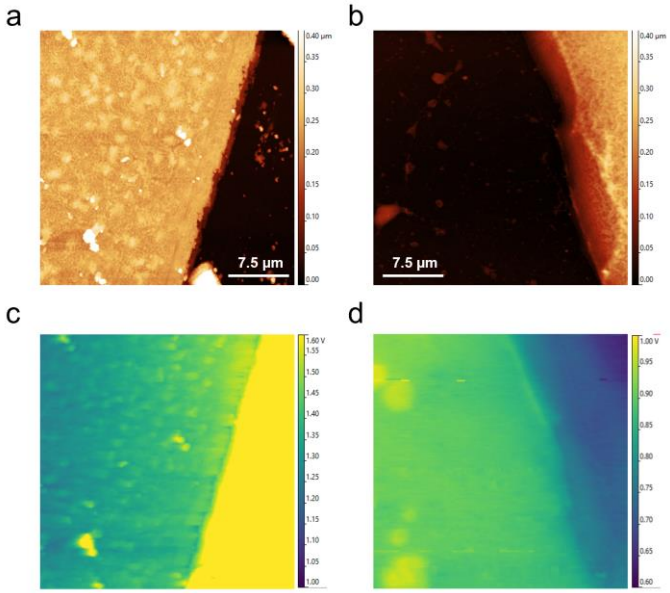

Figure 6.A.1 | Topographic and surface potential images. Large topographic images for **(a)** DP/FS and **(b)** DP/Gr. The surface-potential images for **(c)** DP/FS and **(d)** DP/Gr.

Section 6.A.2: Comparison of OPTP dynamics

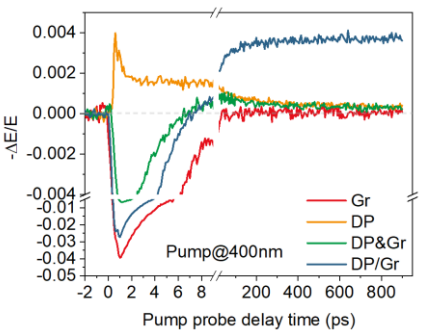

Figure 6.A.2 | Comparison of OPTP dynamics. OPTP dynamics for graphene (Gr, red line), double perovskite (DP, yellow line), double perovskite on Gr without UV-Ozone treatment (DP&Gr, green line) and double perovskite on Gr with UV-Ozone treatment (DP/Gr, blue line). All measurements are conducted in dry N_2 atmosphere, and the samples are pumped with 400 nm (photon energy of 3.10 eV) laser under the same incident photon density of 1.23×10^{14} cm^{-2}.

Note here, that the OPTP dynamics of DP&Gr is simply a superposition of pure DP and pure Gr, which indicates there is no charge transfer at the interface. This data demonstrates the importance of a clean interface between DP and Gr to realize CT in this heterostructure.

Section 6.A.3: Fluence-dependent OPTP dynamics for DP/Gr heterostructure upon different pump photon energies

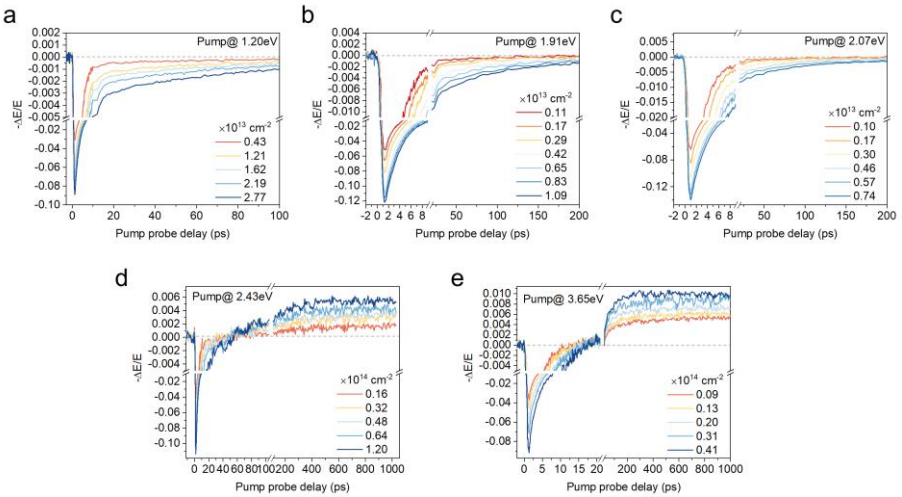

Figure 6.A.3 | Fluence-dependent OPTP dynamics for DP/Gr heterostructure upon different pump photon energies. Photoexcitations with photon energies **(a-c)** below the bandgap of DP, and **(d-e)** above the bandgap of DP.

Section 6.A.4: Band alignment of DP and Gr

From previous measurements, the conduction band minimum and valence band maximum of double perovskite $Cs_2AgBiBr_6$ lie at ~4 eV and ~6 eV [217,229,230] as schematically shown below in **Figure 6.A.4**. The Dirac point of graphene has been measured to be around -4.6 eV [231]. After the construction of DP/Gr heterostructure, we have observed by Raman spectroscopy that the Fermi level of graphene shifts downwards to 380 meV below the Dirac point.

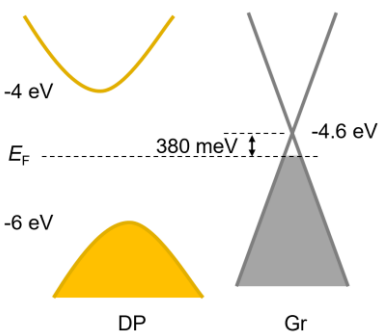

Figure 6.A.4 | Equilibrium band alignment of DP and Gr.

Section 6.A.5: Quantifying CT efficiency

To quantify the CT efficiency at the quasi-equilibrium condition after CT, we conducted THz time-domain spectroscopy for DP/Gr heterostructure at 600 ps after photoexcitation with pump wavelength of 400 nm and absorbed photon density of 7.32×10^{13} cm^{-2}. As shown in **Figure 6.A.2**, the photoresponse at 600 ps is dominated by the Fermi level shift in Gr with negligible contributions from DP. By Fourier transformation, we obtain the frequency-resolved photoconductivity as shown below in **Figure 6.A.5**. We fit the photoconductivity spectra by Drude model [212,223] to extract the transferred carrier density. The Drude response of free carriers in Gr is often formulated in the form of Equation (6.1):

$$\sigma = \frac{D}{\pi}\frac{1}{(\Gamma - i\omega)} \tag{6.1}$$

Here, Γ is the scattering rate. D is the Drude weight that characterizes the magnitude of Drude response. Specifically, $D = (v_F e^2/\hbar)(\pi|N|)^{1/2}$ where v_F is the Fermi velocity, N is the carrier density. By taking the differential of Equation (6.1), one obtains the photoconductivity of Gr. From this fitting, we extract the transferred carrier density of about 1×12 cm^{-2}. Therefore, we estimate the CT efficiency to be ~1.4%.

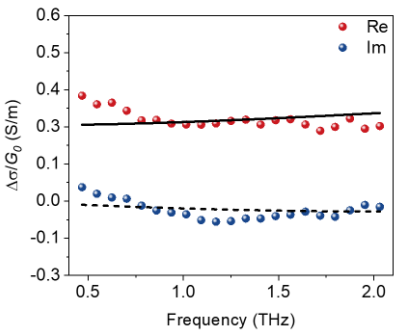

Figure 6.A.5 | The frequency-resolved photoconductivity and Drude fitting for DP/Gr heterostructure. The red and blue dots are the real part and imaginary part of frequency-resolved photoconductivity for DP/Gr pumped at 400 nm with absorbed photon density of 7.32×10^{13} cm^{-2}. The black solid and dashed lines are the Drude fitting. $G_0 = 2e^2/h$ is the quantum conductance.

Summary

In the last decade, low-temperature solution-processed, organic-inorganic hybrid lead halide perovskites (LHPs) have emerged as promising building blocks for efficient optoelectronics (e.g., solar cells and light-emitting diodes) thanks to their exceptional properties such as strong optical absorption, long carrier lifetime, large charge diffusion length, and high defect tolerance. Yet, the chemical instability and lead toxicity of hybrid LHPs impose substantial limitations on the commercialization of perovskite-based optoelectronic devices. Chemically more stable all-inorganic lead halide perovskites and newly developed lead-free double perovskites (DPs) promise to overcome these limitations. To assess the potential of their optoelectronic properties and further optimize the device performance, a fundamental understanding of photo-injected charge carrier dynamics and charge transport properties is crucial. In this thesis, I employ ultrafast Terahertz (THz) spectroscopy to shed light on the formation, transport properties and many-body interactions of large polarons, energetic hot carrier transport, and charge transfer across the relevant interfaces in all-inorganic LHP $CsPbI_3$ or lead-free DP $Cs_2AgBiBr_6$.

The thesis starts by introducing crystal structures and basic optoelectronic properties of most investigated hybrid LHPs, including strong light absorption, high defect tolerance, long carrier diffusion length, low recombination rate, and modest carrier mobility. This is followed by a discussion of stability and toxicity issues of hybrid LHPs and an introduction of materials used in this thesis: all-inorganic orthorhombic phase $CsPbI_3$ (i.e., black γ-$CsPbI_3$) and lead-free double perovskite $Cs_2AgBiBr_6$. We then provide the fundamentals of solid-state physics and literature investigations, focusing on polarons, hot carriers, and charge transfer effects as necessary background information for the remainder of this thesis.

Chapter 2 presents the theoretical basis of THz spectroscopy regarding both THz generation and detection. The THz spectrometer utilized for conducting the thesis works is discussed in detail. Furthermore, the data analysis for extracting the static and photo-induced conductivity is present. At last, we introduce theoretical models to fit the conductivity spectrum, from which we infer fundamental charge transport parameters such as free carrier scattering time, exciton binding energy, etc.

In **Chapter 3**, we study the charge transport in black γ-$CsPbI_3$ where we observe Drude-like band transport of photoexcited charge carriers. The band transport nature has been further corroborated by temperature-dependent measurement in which the photoconductivity is found to decrease drastically with increasing temperature. We show that the observed temperature-dependent photoconductivity can be well described by the formation and transport of large

polarons following the Feynman polaron model. The estimated polaron mobility of 270 ± 44 $cm^2V^{-1}s^{-1}$ in black γ-$CsPbI_3$ is nearly one order of magnitude higher than in hybrid counterparts. Besides, this value approaches the theoretical limit by considering the polaron scattering with longitudinal optical phonons. This work unambiguously unveils the high mobility in γ-$CsPbI_3$, and sheds light on the underlying transport mechanism (i.e., large polaron formation and conduction).

After establishing the large polaron nature in black γ-$CsPbI_3$, **Chapter 4** investigates the charge carrier dynamics and transport following high photoexcitations across the Mott polaron density at which the polaron wavefunction is expected to start overlapping. By ultrafast THz spectroscopy, we observe the photoconductivity saturation effect above the Mott polaron density in black γ-$CsPbI_3$. The Mott polaron density is quantified to be around ~10^{18} cm^{-3} which agrees very well with the theoretical calculations based on the Feynman polaron model. The signature of Mott polaron density is further found in $MAPbI_3$ and $CsPbBr_3$, suggesting that this effect is universal and independent of the constituted ions. Above the Mott polaron density, excess photoinjected charge carriers annihilate quickly within tens to hundreds of picoseconds, depending on the temperature. Besides, we reveal the delocalized band transport even at Mott polaron density with however much-reduced scattering time (~20 fs) compared to the polaron transport at low densities (~40 fs). Our results establish a remarkably stable Mott polaron density in lead halide perovskites with implications for the exotic phenomenon observed in LHPs such as strong Auger recombination and long hot carrier lifetimes.

In **Chapter 5**, we study the hot carrier dynamics in double perovskite $Cs_2AgBiBr_6$, a typical lead-free alternative to LHPs. By varying the incident photon energy, we observe distinct hot carrier dynamics across photon energy of ~2.8 eV. Normalizing the photoconductivity to the absorbed carrier density, our data indicate that the hot carriers are more conductive than cold carriers, reaching a 4-fold enhancement when the photon energy is 1.5 eV above the bandgap. This boosted hot carrier mobility results in a long-range hot carrier transport of more than 200 nm. By further employing optical pump - infrared push - THz probe technique and frequency-resolved photoconductivity measurement, we infer the enhanced mobility originates mainly from the hot holes with much-reduced momentum scattering rate. This conclusion can be rationalized by considering the (quasi-)ballistic transport of energetic hot holes above a certain energy threshold.

In **Chapter 6**, we investigate the charge transfer (CT) process at the interface of $Cs_2AgBiBr_6$ double perovskite/Graphene (DP/Gr) heterostructure relevant for broadband photodetection from THz to X-ray. Here we report a full optical control of hole transfer in strongly coupled DP/Gr heterostructure by readily modulating excitation photon energies. For excitations below the bandgap of DP, we observe hole transfer from photoexcited Gr to DP (very likely to in-gap

defect states in DP). On the other hand, following excitations exceeding the bandgap of DP, a reversed hole transfer from the valence band of DP to the valance band of graphene occurs. Furthermore, we show that increasing photon energies further enhances the transfer efficiency of photoexcited holes in both excitation regimes. These results unveil fundamental photophysics governing interfacial CT at the interface of DP/Gr and provide new insights into controlling CT efficiency and direction across DP/Gr heterostructures in optoelectronic applications.

All in all, our studies disclose key aspects of the carrier dynamics and charge transport properties in metal halide perovskites, particularly the chemically stable all-inorganic lead halide perovskite $CsPbI_3$ and the newly developed lead-free double perovskite $Cs_2AgBiBr_6$. These results establish black γ-$CsPbI_3$ and $Cs_2AgBiBr_6$ as promising building blocks for optoelectronic devices, while simultaneously provide new insights into the photophysics in metal halide perovskites.

Samenvatting

In het laatste decennium zijn in-oplossing-verwerkte organisch-anorganische hybride loodhalogenide perovskieten (LHPs) naar voren gekomen als veelbelovende bouwstenen voor efficiënte opto-elektronica (bijv. zonnecellen en lichtemitterende diodes) dankzij hun uitzonderlijke eigenschappen, zoals sterke optische absorptie, lange levensduur van de ladingsdragers, grote ladingsdiffusielengte, en hoge defecttolerantie. De chemische instabiliteit en het giftige karakter van lood van hybride LHP's leggen echter aanzienlijke beperkingen op aan de commercialisering van op perovskiet gebaseerde opto-elektronische componenten. Chemisch stabielere volledig anorganische loodhalogenide perovskieten en nieuw ontwikkelde loodvrije dubbele perovskieten (DPs) kunnen deze beperkingen overkomen. Om de potentie van hun opto-elektronische eigenschappen te beoordelen en de prestaties van perovskieten verder te optimaliseren, is een fundamenteel begrip van foto-geïnjecteerde ladingsdragers en hun dynamische transporteigenschappen van cruciaal belang. In dit proefschrift maak ik gebruik van ultrasnelle Terahertz (THz) spectroscopie om licht te werpen op de vorming, transporteigenschappen en zgn. many-body interacties van grote polaronen, energetisch ladingstransport van hete ladingen, en lading soverdracht over relevante interfaces in anorganische LHP $CsPbI_3$ of loodvrije DP $Cs_2AgBiBr_6$.

Het proefschrift begint met de introductie van kristalstructuren en opto-elektronische eigenschappen van de meeste onderzochte hybride LHP's, waaronder sterke lichtabsorptie, hoge defecttolerantie, lange ladings diffusielengtes, lage recombinatiesnelheid, en bescheiden ladings mobiliteit. Dit wordt gevolgd door een bespreking van stabiliteits- en toxiciteitsproblemen van hybride LHP's en een introductie van de materialen die in dit proefschrift worden gebruikt: de anorganische orthorhombische fase $CsPbI_3$ (zgn. zwarte γ-$CsPbI_3$) en de loodvrije dubbele perovskiet $Cs_2AgBiBr_6$. Vervolgens bespreken we de grondslagen van de vastestoffysica en een literatuurstudie, met de nadruk op polaronen, hete ladingen, en ladings-overdrachts effecten als achtergrondinformatie voor de rest van dit proefschrift.

Hoofdstuk 2 presenteert de theoretische basis van THz spectroscopie met betrekking tot zowel THz generatie als detectie. De THz spectrometer die gebruikt wordt voor het uitvoeren van het proefschrift wordt in detail besproken. Verder wordt de data-analyse voor de extractie van de statische en foto-geïnduceerde geleidbaarheid gepresenteerd. Tenslotte introduceren we theoretische modellen om het geleidbaarheidsspectrum te passen, waaruit we fundamentele ladingstransportparameters afleiden, zoals de verstrooiingstijd van vrije ladingen, de exciton bindingsenergie, enz.

In **hoofdstuk 3** bestuderen we het ladingstransport in zwarte γ-$CsPbI_3$ waar we Drude-achtig bandtransport waarnemen van fotoexciteerde ladingsdragers. Het type bandtransport is verder bevestigd door temperatuurafhankelijke metingen waarbij de fotogeleidbaarheid drastisch blijkt af te nemen met toenemende temperatuur. Wij tonen aan dat de waargenomen temperatuurafhankelijke fotogeleidbaarheid goed kan worden beschreven door de vorming en het transport van grote polaronen volgens het Feynman polaronenmodel. De geschatte polaronenmobiliteit van 270 ± 44 $cm^2V^{-1}s^{-1}$ in zwarte γ-$CsPbI_3$ is bijna een orde van grootte hoger dan in hybride tegenhangers. Bovendien benadert deze waarde de theoretische limiet door de verstrooiing van polaronen met longitudinale optische fononen aan te nemen. Dit werk onthult ondubbelzinnig de hoge mobiliteit in γ-$CsPbI_3$, en werpt licht op het onderliggende transportmechanisme (d.w.z., grote polaronvorming en geleiding).

Na het vaststellen van de grote polaronen in zwarte γ-$CsPbI_3$, beschrijft **Hoofdstuk 4** de ladingsdrager dynamiek en transport bij hoge fotoexcitatie dichtheden. We beschrijven de Mott polaron dichtheid waarbij de polaron golffunctie begint te overlappen. Met ultrasnelle THz spectroscopie observeren we het verzadigingseffect van de fotogeleidbaarheid boven de Mott polarendichtheid in zwarte γ-$CsPbI_3$. De Mott polaron dichtheid is ongeveer ~10^{18} cm^{-3}, wat zeer goed overeenkomt met de theoretische berekeningen op basis van de Feynman polaron model. Mott polaron dichtheden worden verder gevonden in $MAPbI_3$ en $CsPbBr_3$, wat suggereert dat dit effect universeel is en onafhankelijk van de ionen die het rooster opmaken. Boven de Mott polaron dichtheid annihileren overtollige foto-geïnjecteerde ladingsdragers snel, binnen tientallen tot honderden picoseconden, afhankelijk van de temperatuur. Bovendien laten we gedelokaliseerd bandtransport zien, zelfs bij Mott polarendichtheden met veel kortere verstrooiingstijden (~20 fs) vergeleken met het polarontransport bij lagere dichtheden (~40 fs). Onze resultaten stellen een opmerkelijk stabiele Mott polaronen dichtheid vast in loodhalide perovskieten met implicaties voor de exotische fenomenen waargenomen in LHP's zoals sterke Auger recombinatie en lange hete ladings levensduren.

In **hoofdstuk 5** bestuderen we de dynamica van hete ladingsdragers in dubbel perovskiet $Cs_2AgBiBr_6$, een typisch loodvrij alternatief voor LHP's. Door de inkomende fotonenergie te variëren, zien we een overgang in de dynamiek van de warme ladingen bij een fotonenergie van ~2.8 eV. Normalisatie van de fotogeleidbaarheid naar de geabsorbeerde ladingsdichtheid, laat zien dat de warme ladingen meer geleidend zijn dan koude dragers; tot 4-keer sneller wanneer de foton energie 1.5 eV boven de bandgap is. Deze verhoogde mobiliteit van warme ladingen resulteert in transport van warme dragers over afstanden van meer dan 200 nm. Door verder gebruik te maken van optische-pomp – infrarood-duw – THz-probe techniek en frequentie-opgeloste fotogeleidingsmeting, leiden we af dat de verhoogde mobiliteit voornamelijk afkomstig is van de hete gaten met verminderde momentum-verstrooiingssnelheid. We zien het

(quasi-)ballistische transport van energetische hete gaten boven een bepaalde energiedrempel.

In **hoofdstuk 6** onderzoeken we het ladingsoverdracht (CT) proces aan het grensvlak in een $Cs_2AgBiBr_6$ dubbele perovskiet/Grafeen (DP/Gr) heterostructuur. Zo'n heterostructuur is relevant is voor breedband fotodetectie, van THz tot Röntgenenergieën. Hier rapporteren wij volledige optische controle over gatenoverdracht in een sterk gekoppelde DP/Gr heterostructuur door de excitatie-fotonenergie te variëren. Voor excitaties onder de bandgap van DP, observeren wij gatenoverdracht van fotoexciteerd Gr naar DP (zeer waarschijnlijk naar defecttoestanden in de bandgap van DP). Anderzijds treedt er na excitaties die de bandgap van DP overschrijden een omgekeerde gatenoverdracht op van de valentieband van DP naar de valantieband van grafeen. We tonen bovendien aan dat het verhogen van de fotonenergie de overdrachtsefficiëntie van fotoexciteerde gaten in beide excitatieregimes verder verhoogt. Deze resultaten onthullen fundamentele fotofysica die ladingsoverdracht regelt op het grensvlak van DP/Gr en verschaffen nieuwe inzichten in het controleren van ladingsoverdracht-efficiënties en -richting in DP/Gr heterostructuren voor opto-elektronische toepassingen.

Al met al onthullen onze studies belangrijke aspecten van de ladingsdynamiek en ladingstransporteigenschappen in metaalhalogenide-perovskieten, in het bijzonder in de chemisch stabiele, volledig anorganische loodhalogenide-perovskiet $CsPbI_3$ en de nieuw ontwikkelde loodvrije dubbele perovskiet $Cs_2AgBiBr_6$. Deze resultaten bevestigen zwarte $CsPbI_3$ en $Cs_2AgBiBr_6$ als veelbelovende bouwstenen voor opto-elektronische apparaten, en verschaffen tegelijkertijd nieuwe inzichten in de fotofysica van metaalhalogenide-perovskieten.

Bibliography

[1] International Energy Agency (IEA). *Key world energy statistics 2020*, https://www.iea.org/reports/key-world-energy-statistics-2020 (2022).

[2] Becquerel, A. E. *Recherches sur les effets de la radiation chimique de la lumiere solaire au moyen des courants electriques*. CR Acad. Sci **9**, 1 (1839).

[3] Adams, W. G. & Day, R. E. *V. The action of light on selenium*. Proc. R. Soc. London **25**, 113-117 (1877).

[4] Fritts, C. E. *On a new form of selenium cell, and some electrical discoveries made by its use*. Am. J. Sci. **3**, 465-472 (1883).

[5] Green, M., Dunlop, E., Hohl‐Ebinger, J., Yoshita, M., Kopidakis, N. & Hao, X. *Solar cell efficiency tables (version 57)*. Progress in photovoltaics: research and applications **29**, 3-15 (2021).

[6] Shockley, W. & Queisser, H. J. *Detailed balance limit of efficiency of p‐n junction solar cells*. J. Appl. Phys. **32**, 510-519 (1961).

[7] Wikipedia. *Growth of photovoltaics*, https://en.wikipedia.org/wiki/Growth_of_photovoltaics (2022).

[8] Burschka, J., Pellet, N., Moon, S. J., Humphry-Baker, R., Gao, P., Nazeeruddin, M. K. & Gratzel, M. *Sequential deposition as a route to high-performance perovskite-sensitized solar cells*. Nature **499**, 316-319 (2013).

[9] Zhu, L., Zhang, M., Xu, J., Li, C., Yan, J., Zhou, G., Zhong, W., Hao, T., Song, J., Xue, X., Zhou, Z., Zeng, R., Zhu, H., Chen, C. C., MacKenzie, R. C. I., Zou, Y., Nelson, J., Zhang, Y., Sun, Y. & Liu, F. *Single-junction organic solar cells with over 19% efficiency enabled by a refined double-fibril network morphology*. Nat. Mater. **21**, 656-663 (2022).

[10] Duan, L. & Uddin, A. *Progress in stability of organic solar cells*. Adv. Sci. **7**, 1903259 (2020).

[11] National Renewable Energy Laboratory (NREL). *Nrel solar cell efficiency chart*, https://www.nrel.gov/pv/cell-efficiency.html (2022).

[12] Kojima, A., Teshima, K., Shirai, Y. & Miyasaka, T. *Organometal halide perovskites as visible-light sensitizers for photovoltaic cells*. J. Am. Chem. Soc. **131**, 6050-6051 (2009).

[13] Kim, H. S., Lee, C. R., Im, J. H., Lee, K. B., Moehl, T., Marchioro, A., Moon, S. J., Humphry-Baker, R., Yum, J. H., Moser, J. E., Gratzel, M. & Park, N. G. *Lead iodide perovskite sensitized all-solid-state submicron thin film mesoscopic solar cell with efficiency exceeding 9%*. Sci. Rep. **2**, 591 (2012).

[14] Lee, M. M., Teuscher, J., Miyasaka, T., Murakami, T. N. & Snaith, H. J. *Efficient hybrid solar cells based on meso-superstructured organometal halide perovskites*. Science **338**, 643-647 (2012).

[15] Liu, M., Johnston, M. B. & Snaith, H. J. *Efficient planar heterojunction perovskite solar cells by vapour deposition*. Nature **501**, 395-398 (2013).

[16] Zhou, H., Chen, Q., Li, G., Luo, S., Song, T.-b., Duan, H.-S., Hong, Z., You, J., Liu, Y. & Yang, Y. *Interface engineering of highly efficient perovskite solar cells*. Science **345**, 542-546 (2014).

[17] Docampo, P., Ball, J. M., Darwich, M., Eperon, G. E. & Snaith, H. J. *Efficient*

organometal trihalide perovskite planar-heterojunction solar cells on flexible polymer substrates. Nat. Commun. **4**, 2761 (2013).

[18] Jeong, J., Kim, M., Seo, J., Lu, H., Ahlawat, P., Mishra, A., Yang, Y., Hope, M. A., Eickemeyer, F. T., Kim, M., Yoon, Y. J., Choi, I. W., Darwich, B. P., Choi, S. J., Jo, Y., Lee, J. H., Walker, B., Zakeeruddin, S. M., Emsley, L., Rothlisberger, U., Hagfeldt, A., Kim, D. S., Gratzel, M. & Kim, J. Y. *Pseudo-halide anion engineering for α-$FAPbI_3$ perovskite solar cells*. Nature **592**, 381-385 (2021).

[19] Min, H., Lee, D. Y., Kim, J., Kim, G., Lee, K. S., Kim, J., Paik, M. J., Kim, Y. K., Kim, K. S., Kim, M. G., Shin, T. J. & Il Seok, S. *Perovskite solar cells with atomically coherent interlayers on SnO_2 electrodes*. Nature **598**, 444-450 (2021).

[20] Li, Z., Klein, T. R., Kim, D. H., Yang, M., Berry, J. J., van Hest, M. F. A. M. & Zhu, K. *Scalable fabrication of perovskite solar cells*. Nat. Rev. Mater. **3** (2018).

[21] Liu, X. K., Xu, W., Bai, S., Jin, Y., Wang, J., Friend, R. H. & Gao, F. *Metal halide perovskites for light-emitting diodes*. Nat. Mater. **20**, 10-21 (2021).

[22] Zhu, H., Fu, Y., Meng, F., Wu, X., Gong, Z., Ding, Q., Gustafsson, M. V., Trinh, M. T., Jin, S. & Zhu, X. Y. *Lead halide perovskite nanowire lasers with low lasing thresholds and high quality factors*. Nat. Mater. **14**, 636-642 (2015).

[23] Wei, H., Fang, Y., Mulligan, P., Chuirazzi, W., Fang, H.-H., Wang, C., Ecker, B. R., Gao, Y., Loi, M. A., Cao, L. & Huang, J. *Sensitive X-ray detectors made of methylammonium lead tribromide perovskite single crystals*. Nat. Photonics **10**, 333-339 (2016).

[24] Joshi, P. P., Maehrlein, S. F. & Zhu, X. *Dynamic screening and slow cooling of hot carriers in lead halide perovskites*. Adv. Mater., e1803054 (2019).

[25] Herz, L. M. *Charge-carrier mobilities in metal halide perovskites: Fundamental mechanisms and limits*. ACS Energy Lett. **2**, 1539-1548 (2017).

[26] Li, Z., Yang, M., Park, J.-S., Wei, S.-H., Berry, J. J. & Zhu, K. *Stabilizing perovskite structures by tuning tolerance factor: Formation of formamidinium and cesium lead iodide solid-state alloys*. Chem. Mater. **28**, 284-292 (2016).

[27] Leijtens, T., Eperon, G. E., Noel, N. K., Habisreutinger, S. N., Petrozza, A. & Snaith, H. J. *Stability of metal halide perovskite solar cells*. Adv. Energy Mater. **5**, 1500963 (2015).

[28] Kato, M., Fujiseki, T., Miyadera, T., Sugita, T., Fujimoto, S., Tamakoshi, M., Chikamatsu, M. & Fujiwara, H. *Universal rules for visible-light absorption in hybrid perovskite materials*. J. Appl. Phys. **121**, 115501 (2017).

[29] Saba, M., Quochi, F., Mura, A. & Bongiovanni, G. *Excited state properties of hybrid perovskites*. Acc. Chem. Res. **49**, 166-173 (2016).

[30] Beal, R. E., Slotcavage, D. J., Leijtens, T., Bowring, A. R., Belisle, R. A., Nguyen, W. H., Burkhard, G. F., Hoke, E. T. & McGehee, M. D. *Cesium lead halide perovskites with improved stability for tandem solar cells*. J. Phys. Chem. Lett. **7**, 746-751 (2016).

[31] Protesescu, L., Yakunin, S., Bodnarchuk, M. I., Krieg, F., Caputo, R., Hendon, C. H., Yang, R. X., Walsh, A. & Kovalenko, M. V. *Nanocrystals of cesium lead halide perovskites ($CsPbX_3$, X = Cl, Br, and I): Novel optoelectronic materials showing bright emission with wide color gamut*. Nano Lett. **15**, 3692-3696 (2015).

[32] Huang, J., Yuan, Y., Shao, Y. & Yan, Y. *Understanding the physical properties of hybrid perovskites for photovoltaic applications*. Nat. Rev. Mater. **2** (2017).

[33] Yin, W. J., Shi, T. & Yan, Y. *Unique properties of halide perovskites as possible origins of the superior solar cell performance*. Adv. Mater. **26**, 4653-4658 (2014).

[34] Sun, S., Salim, T., Mathews, N., Duchamp, M., Boothroyd, C., Xing, G., Sum, T. C. & Lam, Y. M. *The origin of high efficiency in low-temperature solution-processable bilayer organometal halide hybrid solar cells*. Energy Environ. Sci. **7**, 399-407 (2014).

[35] Green, M. A., Ho-Baillie, A. & Snaith, H. J. *The emergence of perovskite solar cells*. Nat. Photonics **8**, 506-514 (2014).

[36] Ponseca, C. S., Jr., Savenije, T. J., Abdellah, M., Zheng, K., Yartsev, A., Pascher, T., Harlang, T., Chabera, P., Pullerits, T., Stepanov, A., Wolf, J. P. & Sundstrom, V. *Organometal halide perovskite solar cell materials rationalized: Ultrafast charge generation, high and microsecond-long balanced mobilities, and slow recombination*. J. Am. Chem. Soc. **136**, 5189-5192 (2014).

[37] Valverde-Chávez, D. A., Ponseca, C. S., Stoumpos, C. C., Yartsev, A., Kanatzidis, M. G., Sundström, V. & Cooke, D. G. *Intrinsic femtosecond charge generation dynamics in single crystal $CH_3NH_3PbI_3$*. Energy Environ. Sci. **8**, 3700-3707 (2015).

[38] Chen, Y., Yi, H. T., Wu, X., Haroldson, R., Gartstein, Y. N., Rodionov, Y. I., Tikhonov, K. S., Zakhidov, A., Zhu, X. Y. & Podzorov, V. *Extended carrier lifetimes and diffusion in hybrid perovskites revealed by Hall effect and photoconductivity measurements*. Nat. Commun. **7**, 12253 (2016).

[39] Wehrenfennig, C., Eperon, G. E., Johnston, M. B., Snaith, H. J. & Herz, L. M. *High charge carrier mobilities and lifetimes in organolead trihalide perovskites*. Adv. Mater. **26**, 1584-1589 (2014).

[40] Stranks, S. D., Eperon, G. E., Grancini, G., Menelaou, C., Alcocer, M. J., Leijtens, T., Herz, L. M., Petrozza, A. & Snaith, H. J. *Electron-hole diffusion lengths exceeding 1 micrometer in an organometal trihalide perovskite absorber*. Science **342**, 341-344 (2013).

[41] Dong, Q., Fang, Y., Shao, Y., Mulligan, P., Qiu, J., Cao, L. & Huang, J. *Electron-hole diffusion lengths >175 μm in solution-grown $CH_3NH_3PbI_3$ single crystals*. Science **347**, 967-970 (2015).

[42] Xing, G., Mathews, N., Sun, S., Lim, S. S., Lam, Y. M., Grätzel, M., Mhaisalkar, S. & Sum, T. C. *Long-range balanced electron-and hole-transport lengths in organic-inorganic $CH_3NH_3PbI_3$*. Science **342**, 344-347 (2013).

[43] Yang, Y., Ostrowski, D. P., France, R. M., Zhu, K., van de Lagemaat, J., Luther, J. M. & Beard, M. C. *Observation of a hot-phonon bottleneck in lead-iodide perovskites*. Nat. Photonics **10**, 53-59 (2015).

[44] Zhu, H., Miyata, K., Fu, Y., Wang, J., Joshi, P. P., Niesner, D., Williams, K. W., Jin, S. & Zhu, X.-Y. *Screening in crystalline liquids protects energetic carriers in hybrid perovskites*. Science **353**, 1409-1413 (2016).

[45] Zhi Guo, Y. W., Mengjin Yang, Jordan Snaider, Kai Zhu, Libai Huang. *Long-range hot-carrier transport in hybrid perovskites visualized by ultrafast microscopy*. Science **356**, 59-62 (2017).

[46] Sung, J., Schnedermann, C., Ni, L., Sadhanala, A., Chen, R. Y. S., Cho, C., Priest, L., Lim, J. M., Kim, H.-K., Monserrat, B., Kukura, P. & Rao, A. *Long-range ballistic propagation of carriers in methylammonium lead iodide perovskite thin films*. Nat. Phys. **16**, 171-176 (2019).

[47] Xiao, Z., Song, Z. & Yan, Y. *From lead halide perovskites to lead-free metal halide perovskites and perovskite derivatives*. Adv. Mater. **31**, e1803792 (2019).

[48] Li, N., Niu, X., Chen, Q. & Zhou, H. *Towards commercialization: The operational stability of perovskite solar cells*. Chem Soc Rev **49**, 8235-8286

(2020).
[49] Habisreutinger, S. N., Leijtens, T., Eperon, G. E., Stranks, S. D., Nicholas, R. J. & Snaith, H. J. *Carbon nanotube/polymer composites as a highly stable hole collection layer in perovskite solar cells*. Nano Lett. **14**, 5561-5568 (2014).
[50] You, J., Meng, L., Song, T. B., Guo, T. F., Yang, Y. M., Chang, W. H., Hong, Z., Chen, H., Zhou, H., Chen, Q., Liu, Y., De Marco, N. & Yang, Y. *Improved air stability of perovskite solar cells via solution-processed metal oxide transport layers*. Nat. Nanotechnol. **11**, 75-81 (2016).
[51] Dai, Z., Yadavalli, S. K., Chen, M., Abbaspourtamijani, A., Qi, Y. & Padture, N. P. *Interfacial toughening with self-assembled monolayers enhances perovskite solar cell reliability*. Science **372**, 618-622 (2021).
[52] Liang, J., Wang, C., Wang, Y., Xu, Z., Lu, Z., Ma, Y., Zhu, H., Hu, Y., Xiao, C., Yi, X., Zhu, G., Lv, H., Ma, L., Chen, T., Tie, Z., Jin, Z. & Liu, J. *All-inorganic perovskite solar cells*. J. Am. Chem. Soc. **138**, 15829-15832 (2016).
[53] Steele, J. A., Jin, H., Dovgaliuk, I., Berger, R. F., Braeckevelt, T., Yuan, H., Martin, C., Solano, E., Lejaeghere, K., Rogge, S. M. J., Notebaert, C., Vandezande, W., Janssen, K. P. F., Goderis, B., Debroye, E., Wang, Y. K., Dong, Y., Ma, D., Saidaminov, M., Tan, H., Lu, Z., Dyadkin, V., Chernyshov, D., Van Speybroeck, V., Sargent, E. H., Hofkens, J. & Roeffaers, M. B. J. *Thermal unequilibrium of strained black $CsPbI_3$ thin films*. Science **365**, 679-684 (2019).
[54] Wang, Y., Chen, Y., Zhang, T., Wang, X. & Zhao, Y. *Chemically stable black phase $CsPbI_3$ inorganic perovskites for high-efficiency photovoltaics*. Adv. Mater. **n/a**, 2001025 (2020).
[55] Wang, Y., Dar, M. I., Ono, L. K., Zhang, T., Kan, M., Li, Y., Zhang, L., Wang, X., Yang, Y. & Gao, X. *Thermodynamically stabilized β-$CsPbI_3$–based perovskite solar cells with efficiencies >18%*. Science **365**, 591-595 (2019).
[56] Kim, H.-S., An, Y.-J., Kwak, J. I., Kim, H. J., Jung, H. S. & Park, N.-G. *Sustainable green process for environmentally viable perovskite solar cells*. ACS Energy Lett., 1154-1177 (2022).
[57] Li, M., Li, F., Gong, J., Zhang, T., Gao, F., Zhang, W.-H. & Liu, M. *Advances in tin(II) - based perovskite solar cells: From material physics to device performance*. Small Structures **3** (2021).
[58] Pan, W., Wu, H., Luo, J., Deng, Z., Ge, C., Chen, C., Jiang, X., Yin, W.-J., Niu, G., Zhu, L., Yin, L., Zhou, Y., Xie, Q., Ke, X., Sui, M. & Tang, J. *$Cs_2AgBiBr_6$ single-crystal X-ray detectors with a low detection limit*. Nat. Photonics **11**, 726-732 (2017).
[59] Hoye, R. L. Z., Eyre, L., Wei, F., Brivio, F., Sadhanala, A., Sun, S., Li, W., Zhang, K. H. L., MacManus-Driscoll, J. L., Bristowe, P. D., Friend, R. H., Cheetham, A. K. & Deschler, F. *Fundamental carrier lifetime exceeding 1 μs in $Cs_2AgBiBr_6$ double perovskite*. Adv. Mater. Interfaces. **5**, 1800464 (2018).
[60] Delor, M., Slavney, A. H., Wolf, N. R., Filip, M. R., Neaton, J. B., Karunadasa, H. I. & Ginsberg, N. S. *Carrier diffusion lengths exceeding 1 μm despite trap-limited transport in halide double perovskites*. ACS Energy Lett. **5**, 1337-1345 (2020).
[61] Yang, X., Wang, W., Ran, R., Zhou, W. & Shao, Z. *Recent advances in $Cs_2AgBiBr_6$-based halide double perovskites as lead-free and inorganic light absorbers for perovskite solar cells*. Energy & Fuels (2020).
[62] Xiao, Z., Meng, W., Wang, J. & Yan, Y. *Thermodynamic stability and defect chemistry of bismuth-based lead-free double perovskites*. ChemSusChem **9**,

2628-2633 (2016).
[63] Zhu, X. Y. & Podzorov, V. *Charge carriers in hybrid organic-inorganic lead halide perovskites might be protected as large polarons*. J. Phys. Chem. Lett. **6**, 4758-4761 (2015).
[64] Giustino, F. *Electron-phonon interactions from first principles*. Rev. Mod. Phys. **89** (2017).
[65] Landau, L. *Über die bewegung der elektronen in kristalgitter*. Phys. Z. Sowjetunion **3**, 644-645 (1933).
[66] Franchini, C., Reticcioli, M., Setvin, M. & Diebold, U. *Polarons in materials*. Nat. Rev. Mater. (2021).
[67] Alexandrov, A. S. & Devreese, J. T. *Advances in polaron physics*. Vol. 159 (Springer, 2010).
[68] Fröhlich, H. *Electrons in lattice fields*. Advances in Physics **3**, 325-361 (1954).
[69] Holstein, T. *Studies of polaron motion: Part II. The "small" polaron*. AnPhy **8**, 343-389 (1959).
[70] Feynman, R. P. *Slow electrons in a polar crystal*. Phys. Rev. **97**, 660-665 (1955).
[71] Ōsaka, Y. *Polaron state at a finite temperature*. Prog. Theor. Phys. **22**, 437-446 (1959).
[72] Frost, J. M. *Calculating polaron mobility in halide perovskites*. Phys. Rev. B **96** (2017).
[73] Herz, L. M. *How lattice dynamics moderate the electronic properties of metal-halide perovskites*. J. Phys. Chem. Lett. **9**, 6853-6863 (2018).
[74] Miyata, K., Meggiolaro, D., Trinh, M. T., Joshi, P. P., Mosconi, E., Jones, S. C., De Angelis, F. & Zhu, X.-Y. *Large polarons in lead halide perovskites*. Sci. Adv. **3**, e1701217 (2017).
[75] Guzelturk, B., Winkler, T., Van de Goor, T. W. J., Smith, M. D., Bourelle, S. A., Feldmann, S., Trigo, M., Teitelbaum, S. W., Steinruck, H. G., de la Pena, G. A., Alonso-Mori, R., Zhu, D., Sato, T., Karunadasa, H. I., Toney, M. F., Deschler, F. & Lindenberg, A. M. *Visualization of dynamic polaronic strain fields in hybrid lead halide perovskites*. Nat. Mater. (2021).
[76] Puppin, M., Polishchuk, S., Colonna, N., Crepaldi, A., Dirin, D. N., Nazarenko, O., De Gennaro, R., Gatti, G., Roth, S., Barillot, T., Poletto, L., Xian, R. P., Rettig, L., Wolf, M., Ernstorfer, R., Kovalenko, M. V., Marzari, N., Grioni, M. & Chergui, M. *Evidence of large polarons in photoemission band mapping of the perovskite semiconductor $CsPbBr_3$*. Phys. Rev. Lett. **124**, 206402 (2020).
[77] Feynman, R. P., Hellwarth, R. W., Iddings, C. K. & Platzman, P. M. *Mobility of slow electrons in a polar crystal*. Phys. Rev. **127**, 1004-1017 (1962).
[78] Kadanoff, L. P. *Boltzmann equation for polarons*. Phys. Rev. **130**, 1364-1369 (1963).
[79] Hellwarth, R. W. & Biaggio, I. *Mobility of an electron in a multimode polar lattice*. Phys. Rev. B **60**, 299 (1999).
[80] Ross, R. T. & Nozik, A. J. *Efficiency of hot-carrier solar energy converters*. J. Appl. Phys. **53**, 3813-3818 (1982).
[81] König, D., Casalenuovo, K., Takeda, Y., Conibeer, G., Guillemoles, J., Patterson, R., Huang, L. & Green, M. *Hot carrier solar cells: Principles, materials and design*. Physica E: Low-dimensional Systems and Nanostructures **42**, 2862-2866 (2010).
[82] Brongersma, M. L., Halas, N. J. & Nordlander, P. *Plasmon-induced hot carrier science and technology*. Nat. Nanotechnol. **10**, 25-34 (2015).

[83] Shah, J. *Ultrafast spectroscopy of semiconductors and semiconductor nanostructures*. Vol. 115 (Springer Science & Business Media, 2013).
[84] Doany, F. & Grischkowsky, D. *Measurement of ultrafast hot-carrier relaxation in silicon by thin-film-enhanced, time-resolved reflectivity*. Appl. Phys. Lett. **52**, 36-38 (1988).
[85] Bernardi, M., Vigil-Fowler, D., Lischner, J., Neaton, J. B. & Louie, S. G. *Ab initio study of hot carriers in the first picosecond after sunlight absorption in silicon*. Phys. Rev. Lett. **112**, 257402 (2014).
[86] Bernardi, M., Vigil-Fowler, D., Ong, C. S., Neaton, J. B. & Louie, S. G. *Ab initio study of hot electrons in GaAs*. Proc. Natl. Acad. Sci. U.S.A. **112**, 5291-5296 (2015).
[87] Heiblum, M., Nathan, M. I., Thomas, D. C. & Knoedler, C. M. *Direct observation of ballistic transport in GaAs*. Phys. Rev. Lett. **55**, 2200-2203 (1985).
[88] Sivan, U., Heiblum, M. & Umbach, C. P. *Hot ballistic transport and phonon emission in a two-dimensional electron gas*. Phys. Rev. Lett. **63**, 992-995 (1989).
[89] Fu, J., Xu, Q., Han, G., Wu, B., Huan, C. H. A., Leek, M. L. & Sum, T. C. *Hot carrier cooling mechanisms in halide perovskites*. Nat. Commun. **8**, 1300 (2017).
[90] Zhang, Z., Wang, S., Liu, X., Chen, Y., Su, C., Tang, Z., Li, Y. & Xing, G. *Metal halide perovskite/2d material heterostructures: Syntheses and applications*. Small Methods **5** (2021).
[91] Ulbricht, R., Hendry, E., Shan, J., Heinz, T. F. & Bonn, M. *Carrier dynamics in semiconductors studied with time-resolved terahertz spectroscopy*. Rev. Mod. Phys. **83**, 543-586 (2011).
[92] Yang, K. H., Richards, P. L. & Shen, Y. R. *Generation of far-infrared radiation by picosecond light pulses in $LiNbO_3$*. Appl. Phys. Lett. **19**, 320-323 (1971).
[93] Kaindl, R. A., Eickemeyer, F., Woerner, M. & Elsaesser, T. *Broadband phase-matched difference frequency mixing of femtosecond pulses in GaSe: Experiment and theory*. Appl. Phys. Lett. **75**, 1060-1062 (1999).
[94] Huber, R., Brodschelm, A., Tauser, F. & Leitenstorfer, A. *Generation and field-resolved detection of femtosecond electromagnetic pulses tunable up to 41 THz*. Appl. Phys. Lett. **76**, 3191-3193 (2000).
[95] Auston, D. H., Cheung, K. P. & Smith, P. R. *Picosecond photoconducting hertzian dipoles*. Appl. Phys. Lett. **45**, 284-286 (1984).
[96] Wu, Q. & Zhang, X. C. *Ultrafast electro-optic field sensors*. Appl. Phys. Lett. **68**, 1604-1606 (1996).
[97] Gürtler, A., Winnewisser, C., Helm, H. & Jepsen, P. U. *Terahertz pulse propagation in the near field and the far field*. J. Opt. Soc. Am. **17**, 74-83 (2000).
[98] Benicewicz, P., Roberts, J. & Taylor, A. *Scaling of terahertz radiation from large-aperture biased photoconductors*. J. Opt. Soc. Am. B **11**, 2533-2546 (1994).
[99] Taylor, A., Benicewicz, P. & Young, S. *Modeling of femtosecond electromagnetic pulses from large-aperture photoconductors*. Opt. Lett. **18**, 1340-1342 (1993).
[100] Darrow, J. T., Zhang, X.-C., Auston, D. H. & Morse, J. D. *Saturation properties of large-aperture photoconducting antennas*. IEEE J. Quantum Electron. **28**, 1607-1616 (1992).
[101] Wu, Q., Litz, M. & Zhang, X. C. *Broadband detection capability of ZnTe electro-optic field detectors*. Appl. Phys. Lett. **68**, 2924-2926 (1996).
[102] Turchinovich, D. *Study of ultrafast polarization and carrier dynamics in semiconductor nanostructures: A THz spectroscopy approach*. The University of

Freiburg (2004).
[103] Marple, D. *Refractive index of ZnSe, ZnTe, and CdTe*. J. Appl. Phys. **35**, 539-542 (1964).
[104] Cingolani, A., Ferrara, M. & Lugarà, M. *Dispersion of the linear electrooptic coefficient and of the non-linear susceptibility in ZnTe*. Solid State Commun. **38**, 819-821 (1981).
[105] Ivanov, I. *Terahertz spectroscopy of graphene and graphene nanostructures*, Johannes Gutenberg-Universität Mainz, (2018).
[106] Matthew C. Beard, G. M. T., and Charles A. Schmuttenmaer. *Transient photoconductivity in GaAs as measured by time-resolved terahertz spectroscopy*. Phys. Rev. B **62**, 14 (2000).
[107] Nienhuys, H.-K. & Sundström, V. *Intrinsic complications in the analysis of optical-pump, terahertz probe experiments*. Phys. Rev. B **71** (2005).
[108] Kuzel, P., Kadlec, F. & Nemec, H. *Propagation of terahertz pulses in photoexcited media: Analytical theory for layered systems*. J. Chem. Phys. **127**, 024506 (2007).
[109] Hendry, E., Koeberg, M., Pijpers, J. & Bonn, M. *Reduction of carrier mobility in semiconductors caused by charge-charge interactions*. Phys. Rev. B **75** (2007).
[110] Mics, Z., D'Angio, A., Jensen, S. A., Bonn, M. & Turchinovich, D. *Density-dependent electron scattering in photoexcited GaAs in strongly diffusive regime*. Appl. Phys. Lett. **102** (2013).
[111]Drude, P. *Zur elektronentheorie der metalle*. Ann. Phys. **306**, 566-613 (1900).
[112] Drude, P. *Zur elektronentheorie der metalle; II. Teil. Galvanomagnetische und thermomagnetische effecte*. Ann. Phys. **308**, 369-402 (1900).
[113] Dressel, M. & Scheffler, M. *Verifying the Drude response*. Ann. Phys. **15**, 535-544 (2006).
[114] Ivanov, I., Hu, Y., Osella, S., Beser, U., Wang, H. I., Beljonne, D., Narita, A., Mullen, K., Turchinovich, D. & Bonn, M. *Role of edge engineering in photoconductivity of graphene nanoribbons*. J. Am. Chem. Soc. **139**, 7982-7988 (2017).
[115] Baxter, J. B. & Schmuttenmaer, C. A. *Conductivity of ZnO nanowires, nanoparticles, and thin films using time-resolved terahertz spectroscopy*. J. Phys. Chem. B **110**, 25229-25239 (2006).
[116] Smith, N. *Drude theory and the optical properties of liquid mercury*. Phys. Lett. A **26**, 126-127 (1968).
[117] Cocker, T. L., Baillie, D., Buruma, M., Titova, L. V., Sydora, R. D., Marsiglio, F. & Hegmann, F. A. *Microscopic origin of the Drude-smith model*. Phys. Rev. B **96**, 205439 (2017).
[118] Green, M. A., Dunlop, E. D., Hohl‐Ebinger, J., Yoshita, M., Kopidakis, N. & Ho‐Baillie, A. W. Y. *Solar cell efficiency tables (version 55)*. Progress in Photovoltaics: Research and Applications **28**, 3-15 (2019).
[119] Kang, J. & Wang, L. W. *High defect tolerance in lead halide perovskite $CsPbBr_3$*. J. Phys. Chem. Lett. **8**, 489-493 (2017).
[120] Conings, B., Drijkoningen, J., Gauquelin, N., Babayigit, A., D'Haen, J., D'Olieslaeger, L., Ethirajan, A., Verbeeck, J., Manca, J., Mosconi, E., Angelis, F. D. & Boyen, H.-G. *Intrinsic thermal instability of methylammonium lead trihalide perovskite*. Adv. Energy Mater. **5** (2015).
[121] Christians, J. A., Miranda Herrera, P. A. & Kamat, P. V. *Transformation of*

the excited state and photovoltaic efficiency of $CH_3NH_3PbI_3$ perovskite upon controlled exposure to humidified air. J. Am. Chem. Soc. **137**, 1530-1538 (2015).

[122] Eperon, G. E., Stranks, S. D., Menelaou, C., Johnston, M. B., Herz, L. M. & Snaith, H. J. *Formamidinium lead trihalide: A broadly tunable perovskite for efficient planar heterojunction solar cells*. Energy Environ. Sci. **7** (2014).

[123] Kulbak, M., Gupta, S., Kedem, N., Levine, I., Bendikov, T., Hodes, G. & Cahen, D. *Cesium enhances long-term stability of lead bromide perovskite-based solar cells*. J. Phys. Chem. Lett. **7**, 167-172 (2016).

[124] Eperon, G. E., Paternò, G. M., Sutton, R. J., Zampetti, A., Haghighirad, A. A., Cacialli, F. & Snaith, H. J. *Inorganic caesium lead iodide perovskite solar cells*. J. Mater. Chem. A **3**, 19688-19695 (2015).

[125] Wang, Y., Dar, M. I., Ono, L. K., Zhang, T., Kan, M., Li, Y., Zhang, L., Wang, X., Yang, Y. & Gao, X. *Thermodynamically stabilized β-CsPbI3–based perovskite solar cells with efficiencies> 18%*. Science **365**, 591-595 (2019).

[126] Swarnkar, A., Marshall, A. R., Sanehira, E. M., Chernomordik, B. D., Moore, D. T., Christians, J. A., Chakrabarti, T. & Luther, J. M. *Quantum dot–induced phase stabilization of α-$CsPbI_3$ perovskite for high-efficiency photovoltaics*. Science **354**, 92-95 (2016).

[127] Li, B., Zhang, Y., Fu, L., Yu, T., Zhou, S., Zhang, L. & Yin, L. *Surface passivation engineering strategy to fully-inorganic cubic $CsPbI_3$ perovskites for high-performance solar cells*. Nat. Commun. **9**, 1076 (2018).

[128] Wang, K., Jin, Z., Liang, L., Bian, H., Bai, D., Wang, H., Zhang, J., Wang, Q. & Liu, S. *All-inorganic cesium lead iodide perovskite solar cells with stabilized efficiency beyond 15%*. Nat. Commun. **9**, 4544 (2018).

[129] Wang, P., Zhang, X., Zhou, Y., Jiang, Q., Ye, Q., Chu, Z., Li, X., Yang, X., Yin, Z. & You, J. *Solvent-controlled growth of inorganic perovskite films in dry environment for efficient and stable solar cells*. Nat. Commun. **9**, 2225 (2018).

[130] Wang, Y., Zhang, T., Kan, M. & Zhao, Y. *Bifunctional stabilization of all-inorganic α-$CsPbI_3$ perovskite for 17% efficiency photovoltaics*. J. Am. Chem. Soc. **140**, 12345-12348 (2018).

[131] Shang, Q., Piercy, B. D., Losego, M. D. & Lian, T. *Effect of surface ligand on charge separation and recombination at $CsPbI_3$ perovskite quantum dot/TiO_2 interfaces*. J Phys Chem C **123**, 21415-21421 (2019).

[132] Liu, F., Zhang, Y., Ding, C., Toyoda, T., Ogomi, Y., Ripolles, T. S., Hayase, S., Minemoto, T., Yoshino, K., Dai, S. & Shen, Q. *Ultrafast electron injection from photoexcited perovskite $CsPbI_3$ QDs into TiO_2 nanoparticles with injection efficiency near 99%*. J. Phys. Chem. Lett. **9**, 294-297 (2018).

[133] Cong, M., Yang, B., Chen, J., Hong, F., Yang, S., Deng, W. & Han, K. *Carrier multiplication and hot-carrier cooling dynamics in quantum-confined $CsPbI_3$ perovskite nanocrystals*. J. Phys. Chem. Lett. **11**, 1921-1926 (2020).

[134] de Weerd, C., Gomez, L., Capretti, A., Lebrun, D. M., Matsubara, E., Lin, J., Ashida, M., Spoor, F. C. M., Siebbeles, L. D. A., Houtepen, A. J., Suenaga, K., Fujiwara, Y. & Gregorkiewicz, T. *Efficient carrier multiplication in $CsPbI_3$ perovskite nanocrystals*. Nat. Commun. **9**, 4199 (2018).

[135] Zheng, F. & Wang, L.-w. *Large polaron formation and its effect on electron transport in hybrid perovskites*. Energy Environ. Sci. **12**, 1219-1230 (2019).

[136] Emin, D. *Optical properties of large and small polarons and bipolarons*. Phys. Rev. B **48**, 13691-13702 (1993).

[137] Ghosh, T., Aharon, S., Etgar, L. & Ruhman, S. *Free carrier emergence and*

onset of electron-phonon coupling in methylammonium lead halide perovskite films. J. Am. Chem. Soc. **139**, 18262-18270 (2017).

[138] Batignani, G., Fumero, G., Srimath Kandada, A. R., Cerullo, G., Gandini, M., Ferrante, C., Petrozza, A. & Scopigno, T. *Probing femtosecond lattice displacement upon photo-carrier generation in lead halide perovskite*. Nat. Commun. **9**, 1971 (2018).

[139] Steele, J. A., Puech, P., Keshavarz, M., Yang, R., Banerjee, S., Debroye, E., Kim, C. W., Yuan, H., Heo, N. H., Vanacken, J., Walsh, A., Hofkens, J. & Roeffaers, M. B. J. *Giant electron-phonon coupling and deep conduction band resonance in metal halide double perovskite*. ACS Nano **12**, 8081-8090 (2018).

[140] Keshavarz, M., Debroye, E., Ottesen, M., Martin, C., Zhang, H., Fron, E., Küchler, R., Steele, J. A., Bremholm, M., Van de Vondel, J., Wang, H. I., Bonn, M., Roeffaers, M. B. J., Wiedmann, S. & Hofkens, J. *Tuning the structural and optoelectronic properties of $Cs_2AgBiBr_6$ double-perovskite single crystals through alkali-metal substitution*. Adv. Mater. **32**, 2001878 (2020).

[141] Steele, J. A., Puech, P., Monserrat, B., Wu, B., Yang, R. X., Kirchartz, T., Yuan, H., Fleury, G., Giovanni, D., Fron, E., Keshavarz, M., Debroye, E., Zhou, G., Sum, T. C., Walsh, A., Hofkens, J. & Roeffaers, M. B. J. *Role of electron–phonon coupling in the thermal evolution of bulk rashba-like spin-split lead halide perovskites exhibiting dual-band photoluminescence*. ACS Energy Lett. **4**, 2205-2212 (2019).

[142] Bretschneider, S. A., Ivanov, I., Wang, H. I., Miyata, K., Zhu, X. & Bonn, M. *Quantifying polaron formation and charge carrier cooling in lead-iodide perovskites*. Adv. Mater., e1707312 (2018).

[143] Karakus, M., Jensen, S. A., D'Angelo, F., Turchinovich, D., Bonn, M. & Canovas, E. *Phonon-electron scattering limits free charge mobility in methylammonium lead iodide perovskites*. J. Phys. Chem. Lett. **6**, 4991-4996 (2015).

[144] Milot, R. L., Eperon, G. E., Snaith, H. J., Johnston, M. B. & Herz, L. M. *Temperature-dependent charge-carrier dynamics in $CH_3NH_3PbI_3$ perovskite thin films*. Adv. Funct. Mater. **25**, 6218-6227 (2015).

[145] Savenije, T. J., Ponseca, C. S., Jr., Kunneman, L., Abdellah, M., Zheng, K., Tian, Y., Zhu, Q., Canton, S. E., Scheblykin, I. G., Pullerits, T., Yartsev, A. & Sundstrom, V. *Thermally activated exciton dissociation and recombination control the carrier dynamics in organometal halide perovskite*. J. Phys. Chem. Lett. **5**, 2189-2194 (2014).

[146] Keshavarz, M., Wiedmann, S., Yuan, H., Debroye, E., Roeffaers, M. & Hofkens, J. *Light- and temperature-modulated magneto-transport in organic–inorganic lead halide perovskites*. ACS Energy Lett. **3**, 39-45 (2017).

[147] Cinquanta, E., Meggiolaro, D., Motti, S. G., Gandini, M., Alcocer, M. J. P., Akkerman, Q. A., Vozzi, C., Manna, L., De Angelis, F., Petrozza, A. & Stagira, S. *Ultrafast THz probe of photoinduced polarons in lead-halide perovskites*. Phys. Rev. Lett. **122**, 166601 (2019).

[148] Even, J., Pedesseau, L., Jancu, J.-M. & Katan, C. *Importance of spin–orbit coupling in hybrid organic/inorganic perovskites for photovoltaic applications*. J. Phys. Chem. Lett. **4**, 2999-3005 (2013).

[149] Kang, Y. & Han, S. *Intrinsic carrier mobility of cesium lead halide perovskites*. Phys. Rev. Appl. **10** (2018).

[150] Singh, R. K., Kumar, R., Jain, N., Dash, S. R., Singh, J. & Srivastava, A.

Investigation of optical and dielectric properties of $CsPbI_3$ inorganic lead iodide perovskite thin film. J. Taiwan Inst. Chem. Eng. **96**, 538-542 (2019).

[151] Andrianov, A. V., Aleshin, A. N. & Matyushkin, L. B. *Terahertz vibrational modes in $CH_3NH_3PbI_3$ and $CsPbI_3$ perovskite films*. JETP Lett. **109**, 28-32 (2019).

[152] Bonn, M., Miyata, K., Hendry, E. & Zhu, X. Y. *Role of dielectric drag in polaron mobility in lead halide perovskites*. ACS Energy Lett. **2**, 2555-2562 (2017).

[153] Sutton, R. J., Filip, M. R., Haghighirad, A. A., Sakai, N., Wenger, B., Giustino, F. & Snaith, H. J. *Cubic or orthorhombic? Revealing the crystal structure of metastable black-phase $CsPbI_3$ by theory and experiment*. ACS Energy Lett. **3**, 1787-1794 (2018).

[154] Yang, Z., Surrente, A., Galkowski, K., Miyata, A., Portugall, O., Sutton, R. J., Haghighirad, A. A., Snaith, H. J., Maude, D. K., Plochocka, P. & Nicholas, R. J. *Impact of the halide cage on the electronic properties of fully inorganic cesium lead halide perovskites*. ACS Energy Lett. **2**, 1621-1627 (2017).

[155] Oga, H., Saeki, A., Ogomi, Y., Hayase, S. & Seki, S. *Improved understanding of the electronic and energetic landscapes of perovskite solar cells: High local charge carrier mobility, reduced recombination, and extremely shallow traps*. J. Am. Chem. Soc. **136**, 13818-13825 (2014).

[156] Piatkowski, P., Cohen, B., Ponseca, C. S., Jr., Salado, M., Kazim, S., Ahmad, S., Sundstrom, V. & Douhal, A. *Unraveling charge carriers generation, diffusion, and recombination in formamidinium lead triiodide perovskite polycrystalline thin film*. J. Phys. Chem. Lett. **7**, 204-210 (2016).

[157] Rehman, W., Milot, R. L., Eperon, G. E., Wehrenfennig, C., Boland, J. L., Snaith, H. J., Johnston, M. B. & Herz, L. M. *Charge-carrier dynamics and mobilities in formamidinium lead mixed-halide perovskites*. Adv. Mater. **27**, 7938-7944 (2015).

[158] Beattie, A. & Landsberg, P. *Auger effect in semiconductors*. Proc. R. Soc. London, Ser. A **249**, 16-29 (1959).

[159] Motti, S. G., Krieg, F., Ramadan, A. J., Patel, J. B., Snaith, H. J., Kovalenko, M. V., Johnston, M. B. & Herz, L. M. *$CsPbBr_3$ nanocrystal films: Deviations from bulk vibrational and optoelectronic properties*. Adv. Funct. Mater. **30** (2020).

[160] Kennedy, C. L., Hill, A. H., Massaro, E. S. & Grumstrup, E. M. *Ultrafast excited-state transport and decay dynamics in cesium lead mixed halide perovskites*. ACS Energy Lett. **2**, 1501-1506 (2017).

[161] Manser, J. S. & Kamat, P. V. *Band filling with free charge carriers in organometal halide perovskites*. Nat. Photonics **8**, 737-743 (2014).

[162] Yamada, Y., Nakamura, T., Endo, M., Wakamiya, A. & Kanemitsu, Y. *Photocarrier recombination dynamics in perovskite $CH_3NH_3PbI_3$ for solar cell applications*. J. Am. Chem. Soc. **136**, 11610-11613 (2014).

[163] Ulatowski, A. M., Wright, A. D., Wenger, B., Buizza, L. R. V., Motti, S. G., Eggimann, H. J., Savill, K. J., Borchert, J., Snaith, H. J., Johnston, M. B. & Herz, L. M. *Charge-carrier trapping dynamics in bismuth-doped thin films of $MAPbBr_3$ perovskite*. J. Phys. Chem. Lett. **11**, 3681-3688 (2020).

[164] Jiang, Q., Zhao, Y., Zhang, X., Yang, X., Chen, Y., Chu, Z., Ye, Q., Li, X., Yin, Z. & You, J. *Surface passivation of perovskite film for efficient solar cells*. Nat. Photonics **13**, 460-466 (2019).

[165] Lin, K., Xing, J., Quan, L. N., de Arquer, F. P. G., Gong, X., Lu, J., Xie, L.,

Zhao, W., Zhang, D., Yan, C., Li, W., Liu, X., Lu, Y., Kirman, J., Sargent, E. H., Xiong, Q. & Wei, Z. *Perovskite light-emitting diodes with external quantum efficiency exceeding 20 per cent*. Nature **562**, 245-248 (2018).

[166] Zhang, H., Debroye, E., Steele, J. A., Roeffaers, M. B. J., Hofkens, J., Wang, H. I. & Bonn, M. *Highly mobile large polarons in black phase $CsPbI_3$*. ACS Energy Lett. **6**, 568-573 (2021).

[167] Brenner, P., Bar-On, O., Jakoby, M., Allegro, I., Richards, B. S., Paetzold, U. W., Howard, I. A., Scheuer, J. & Lemmer, U. *Continuous wave amplified spontaneous emission in phase-stable lead halide perovskites*. Nat. Commun. **10**, 988 (2019).

[168] Wang, Z., Lin, Q., Wenger, B., Christoforo, M. G., Lin, Y.-H., Klug, M. T., Johnston, M. B., Herz, L. M. & Snaith, H. J. *High irradiance performance of metal halide perovskites for concentrator photovoltaics*. Nat. Energy **3**, 855-861 (2018).

[169] Shen, J.-X., Zhang, X., Das, S., Kioupakis, E. & Van de Walle, C. G. *Unexpectedly strong auger recombination in halide perovskites*. Adv. Energy Mater. **8** (2018).

[170] Jiang, Y., Cui, M., Li, S., Sun, C., Huang, Y., Wei, J., Zhang, L., Lv, M., Qin, C., Liu, Y. & Yuan, M. *Reducing the impact of auger recombination in quasi-2d perovskite light-emitting diodes*. Nat. Commun. **12**, 336 (2021).

[171] Frost, J. M., Whalley, L. D. & Walsh, A. *Slow cooling of hot polarons in halide perovskite solar cells*. ACS Energy Lett. **2**, 2647-2652 (2017).

[172] Edwards, P. P. & Sienko, M. J. *Universality aspects of the metal-nonmetal transition in condensed media*. Phys. Rev. B **17**, 2575-2581 (1978).

[173] Sendner, M., Nayak, P. K., Egger, D. A., Beck, S., Müller, C., Epding, B., Kowalsky, W., Kronik, L., Snaith, H. J., Pucci, A. & Lovrinčić, R. *Optical phonons in methylammonium lead halide perovskites and implications for charge transport*. Mater. Horiz. **3**, 613-620 (2016).

[174] Schultz, T. D. *Slow electrons in polar crystals: Self-energy, mass, and mobility*. Phys. Rev. **116**, 526-543 (1959).

[175] Emin, D. *Barrier to recombination of oppositely charged large polarons*. J. Appl. Phys. **123** (2018).

[176] Yang, Y., Yang, M., Li, Z., Crisp, R., Zhu, K. & Beard, M. C. *Comparison of recombination dynamics in $CH_3NH_3PbBr_3$ and $CH_3NH_3PbI_3$ perovskite films: Influence of exciton binding energy*. J. Phys. Chem. Lett. **6**, 4688-4692 (2015).

[177] La, O. V. C., Salim, T., Kadro, J., Khuc, M. T., Haselsberger, R., Cheng, L., Xia, H., Gurzadyan, G. G., Su, H., Lam, Y. M., Marcus, R. A., Michel-Beyerle, M. E. & Chia, E. E. *Elucidating the role of disorder and free-carrier recombination kinetics in $CH_3NH_3PbI_3$ perovskite films*. Nat. Commun. **6**, 7903 (2015).

[178] Emin, D. *Polarons*. (Cambridge University Press, 2013).

[179] Yin, Y., Fu, S., Zhou, S., Song, Y., Li, L., Zhang, M., Wang, J., Mariyappan, P., Alshehri, S. M., Ahamad, T. & Yamauchi, Y. *Efficient and stable ideal bandgap perovskite solar cell achieved by a small amount of tin substituted methylammonium lead iodide*. Electron. Mater. Lett. **16**, 224-230 (2020).

[180] Leguy, A. M., Azarhoosh, P., Alonso, M. I., Campoy-Quiles, M., Weber, O. J., Yao, J., Bryant, D., Weller, M. T., Nelson, J., Walsh, A., van Schilfgaarde, M. & Barnes, P. R. *Experimental and theoretical optical properties of methylammonium lead halide perovskites*. Nanoscale **8**, 6317-6327 (2016).

[181] Whalley, L. D., Frost, J. M., Morgan, B. J. & Walsh, A. *Impact of nonparabolic electronic band structure on the optical and transport properties of photovoltaic materials*. Phys. Rev. B **99** (2019).

[182] Oudar, J. L., Hulin, D., Migus, A., Antonetti, A. & Alexandre, F. *Subpicosecond spectral hole burning due to nonthermalized photoexcited carriers in GaAs*. Phys. Rev. Lett. **55**, 2074-2077 (1985).

[183] Hunsche, S., Heesel, H., Ewertz, A., Kurz, H. & Collet, J. H. *Spectral-hole burning and carrier thermalization in GaAs at room temperature*. Phys. Rev. B **48**, 17818-17826 (1993).

[184] Richter, J. M., Branchi, F., Valduga de Almeida Camargo, F., Zhao, B., Friend, R. H., Cerullo, G. & Deschler, F. *Ultrafast carrier thermalization in lead iodide perovskite probed with two-dimensional electronic spectroscopy*. Nat. Commun. **8**, 376 (2017).

[185] Nguyen, D.-T., Lombez, L., Gibelli, F., Boyer-Richard, S., Le Corre, A., Durand, O. & Guillemoles, J.-F. *Quantitative experimental assessment of hot carrier-enhanced solar cells at room temperature*. Nat. Energy **3**, 236-242 (2018).

[186] Esmaielpour, H., Dorman, K. R., Ferry, D. K., Mishima, T. D., Santos, M. B., Whiteside, V. R. & Sellers, I. R. *Exploiting intervalley scattering to harness hot carriers in III–V solar cells*. Nat. Energy **5**, 336-343 (2020).

[187] Turchinovich, D., D'Angelo, F. & Bonn, M. *Femtosecond-timescale buildup of electron mobility in GaAs observed via ultrabroadband transient terahertz spectroscopy*. Appl. Phys. Lett. **110** (2017).

[188] Monti, M., Jayawardena, K. D. G. I., Butler-Caddle, E., Bandara, R. M. I., Woolley, J. M., Staniforth, M., Silva, S. R. P. & Lloyd-Hughes, J. *Hot carriers in mixed Pb-Sn halide perovskite semiconductors cool slowly while retaining their electrical mobility* Phys. Rev. B **102**, 245204 (2020).

[189] Steele, J. A., Pan, W., Martin, C., Keshavarz, M., Debroye, E., Yuan, H., Banerjee, S., Fron, E., Jonckheere, D., Kim, C. W., Baekelant, W., Niu, G., Tang, J., Vanacken, J., Van der Auweraer, M., Hofkens, J. & Roeffaers, M. B. J. *Photophysical pathways in highly sensitive $Cs_2AgBiBr_6$ double-perovskite single-crystal X-ray detectors*. Adv. Mater. **30**, e1804450 (2018).

[190] Ning, W., Wang, F., Wu, B., Lu, J., Yan, Z., Liu, X., Tao, Y., Liu, J. M., Huang, W., Fahlman, M., Hultman, L., Sum, T. C. & Gao, F. *Long electron-hole diffusion length in high-quality lead-free double perovskite films*. Adv. Mater. **30**, e1706246 (2018).

[191] Schade, L., Wright, A. D., Johnson, R. D., Dollmann, M., Wenger, B., Nayak, P. K., Prabhakaran, D., Herz, L. M., Nicholas, R., Snaith, H. J. & Radaelli, P. G. *Structural and optical properties of $Cs_2AgBiBr_6$ double perovskite*. ACS Energy Lett. **4**, 299-305 (2018).

[192] Wu, B., Ning, W., Xu, Q., Manjappa, M., Feng, M., Ye, S., Fu, J., Lie, S., Yin, T. & Wang, F. *Strong self-trapping by deformation potential limits photovoltaic performance in bismuth double perovskite*. Sci. Adv. **7**, eabd3160 (2021).

[193] Wright, A. D., Buizza, L. R. V., Savill, K. J., Longo, G., Snaith, H. J., Johnston, M. B. & Herz, L. M. *Ultrafast excited-state localization in $Cs_2AgBiBr_6$ double perovskite*. J. Phys. Chem. Lett., 3352-3360 (2021).

[194] Schmitz, A., Schaberg, L. L., Sirotinskaya, S., Pantaler, M., Lupascu, D. C., Benson, N. & Bacher, G. *Fine structure of the optical absorption resonance in $Cs_2AgBiBr_6$ double perovskite thin films*. ACS Energy Lett. **5**, 559-565 (2020).

[195] Longo, G., Mahesh, S., Buizza, L. R. V., Wright, A. D., Ramadan, A. J., Abdi-Jalebi, M., Nayak, P. K., Herz, L. M. & Snaith, H. J. *Understanding the performance-limiting factors of $Cs_2AgBiBr_6$ double-perovskite solar cells*. ACS Energy Lett., 2200-2207 (2020).

[196] Uhd Jepsen, P., Schairer, W., Libon, I. H., Lemmer, U., Hecker, N. E., Birkholz, M., Lips, K. & Schall, M. *Ultrafast carrier trapping in microcrystalline silicon observed in optical pump–terahertz probe measurements*. Appl. Phys. Lett. **79**, 1291-1293 (2001).

[197] Maehrlein, S. F., Joshi, P. P., Huber, L., Wang, F., Cherasse, M., Liu, Y., Juraschek, D. M., Mosconi, E., Meggiolaro, D., De Angelis, F. & Zhu, X. Y. *Decoding ultrafast polarization responses in lead halide perovskites by the two-dimensional optical Kerr effect*. Proc. Natl. Acad. Sci. U.S.A. **118** (2021).

[198] Bakulin, A. A., Rao, A., Pavelyev, V. G., van Loosdrecht, P. H., Pshenichnikov, M. S., Niedzialek, D., Cornil, J., Beljonne, D. & Friend, R. H. *The role of driving energy and delocalized states for charge separation in organic semiconductors*. Science **335**, 1340-1344 (2012).

[199] McClure, E. T., Ball, M. R., Windl, W. & Woodward, P. M. *Cs_2AgBiX_6 (X = Br, Cl): New visible light absorbing, lead-free halide perovskite semiconductors*. Chem. Mater. **28**, 1348-1354 (2016).

[200] Du, K. Z., Meng, W., Wang, X., Yan, Y. & Mitzi, D. B. *Bandgap engineering of lead-free double perovskite $Cs_2AgBiBr_6$ through trivalent metal alloying*. Angew. Chem. Int. Ed. Engl. **56**, 8158-8162 (2017).

[201] Palummo, M., Berrios, E., Varsano, D. & Giorgi, G. *Optical properties of lead-free double perovskites by ab initio excited-state methods*. ACS Energy Lett. **5**, 457-463 (2020).

[202] Hendry, E., Koeberg, M., Wang, F., Zhang, H., de Mello Donega, C., Vanmaekelbergh, D. & Bonn, M. *Direct observation of electron-to-hole energy transfer in CdSe quantum dots*. Phys. Rev. Lett. **96**, 057408 (2006).

[203] Schins, J. M., Hendry, E., Bonn, M. & Muller, H. G. *Retrieving the susceptibility from time-resolved terahertz experiments*. J. Chem. Phys. **127**, 094308 (2007).

[204] Hendry, E. *Charge dynamics in novel semiconductors*. University of Amsterdam (2005).

[205] Banszerus, L., Schmitz, M., Engels, S., Goldsche, M., Watanabe, K., Taniguchi, T., Beschoten, B. & Stampfer, C. *Ballistic transport exceeding 28 um in CVD grown graphene*. Nano Lett. **16**, 1387-1391 (2016).

[206] Du, X., Skachko, I., Barker, A. & Andrei, E. Y. *Approaching ballistic transport in suspended graphene*. Nat. Nanotechnol. **3**, 491-495 (2008).

[207] Koppens, F. H., Mueller, T., Avouris, P., Ferrari, A. C., Vitiello, M. S. & Polini, M. *Photodetectors based on graphene, other two-dimensional materials and hybrid systems*. Nat. Nanotechnol. **9**, 780-793 (2014).

[208] Konstantatos, G., Badioli, M., Gaudreau, L., Osmond, J., Bernechea, M., Garcia de Arquer, F. P., Gatti, F. & Koppens, F. H. *Hybrid graphene-quantum dot phototransistors with ultrahigh gain*. Nat. Nanotechnol. **7**, 363-368 (2012).

[209] Liu, Z., Qiu, H., Fu, S., Wang, C., Yao, X., Dixon, A. G., Campidelli, S., Pavlica, E., Bratina, G., Zhao, S., Rondin, L., Lauret, J. S., Narita, A., Bonn, M., Mullen, K., Ciesielski, A., Wang, H. I. & Samori, P. *Solution-processed graphene-nanographene van der waals heterostructures for photodetectors with efficient and ultralong charge separation*. J. Am. Chem. Soc. (2021).

[210] Zhang, W., Chuu, C. P., Huang, J. K., Chen, C. H., Tsai, M. L., Chang, Y. H., Liang, C. T., Chen, Y. Z., Chueh, Y. L., He, J. H., Chou, M. Y. & Li, L. J. *Ultrahigh-gain photodetectors based on atomically thin graphene-MoS_2 heterostructures*. Sci. Rep. **4**, 3826 (2014).

[211] Wang, X., Cheng, Z., Xu, K., Tsang, H. K. & Xu, J.-B. *High-responsivity graphene/silicon-heterostructure waveguide photodetectors*. Nat. Photonics **7**, 888-891 (2013).

[212] Fu, S., du Fossé, I., Jia, X., Xu, J., Yu, X., Zhang, H., Zheng, W., Krasel, S., Chen, Z. & Wang, Z. M. *Long-lived charge separation following pump-wavelength–dependent ultrafast charge transfer in graphene/WS_2 heterostructures*. Sci. Adv. **7**, eabd9061 (2021).

[213] Massicotte, M., Schmidt, P., Vialla, F., Watanabe, K., Taniguchi, T., Tielrooij, K. J. & Koppens, F. H. *Photo-thermionic effect in vertical graphene heterostructures*. Nat. Commun. **7**, 12174 (2016).

[214] Trovatello, C., Piccinini, G., Forti, S., Fabbri, F., Rossi, A., De Silvestri, S., Coletti, C., Cerullo, G. & Dal Conte, S. *Ultrafast hot carrier transfer in WS_2/graphene large area heterostructures*. npj 2D Mater. Appl. **6** (2022).

[215] Lee, Y., Kwon, J., Hwang, E., Ra, C. H., Yoo, W. J., Ahn, J. H., Park, J. H. & Cho, J. H. *High-performance perovskite-graphene hybrid photodetector*. Adv. Mater. **27**, 41-46 (2015).

[216] Chang, P. H., Liu, S. Y., Lan, Y. B., Tsai, Y. C., You, X. Q., Li, C. S., Huang, K. Y., Chou, A. S., Cheng, T. C., Wang, J. K. & Wu, C. I. *Ultrahigh responsivity and detectivity graphene-perovskite hybrid phototransistors by sequential vapor deposition*. Sci. Rep. **7**, 46281 (2017).

[217] Slavney, A. H., Hu, T., Lindenberg, A. M. & Karunadasa, H. I. *A bismuth-halide double perovskite with long carrier recombination lifetime for photovoltaic applications*. J. Am. Chem. Soc. **138**, 2138-2141 (2016).

[218] Zhang, H., Debroye, E., Zheng, W., Fu, S., Virgilio, L. D., Kumar, P., Bonn, M. & Wang, H. I. *Highly mobile hot holes in $Cs_2AgBiBr_6$ double perovskite*. Sci. Adv. **7**, eabj9066 (2021).

[219] Ferrari, A. C. & Basko, D. M. *Raman spectroscopy as a versatile tool for studying the properties of graphene*. Nat. Nanotechnol. **8**, 235-246 (2013).

[220] Das, A., Pisana, S., Chakraborty, B., Piscanec, S., Saha, S. K., Waghmare, U. V., Novoselov, K. S., Krishnamurthy, H. R., Geim, A. K., Ferrari, A. C. & Sood, A. K. *Monitoring dopants by Raman scattering in an electrochemically top-gated graphene transistor*. Nat. Nanotechnol. **3**, 210-215 (2008).

[221] Jia, X., Hu, M., Soundarapandian, K., Yu, X., Liu, Z., Chen, Z., Narita, A., Mullen, K., Koppens, F. H. L., Jiang, J., Tielrooij, K. J., Bonn, M. & Wang, H. I. *Kinetic ionic permeation and interfacial doping of supported graphene*. Nano Lett. **19**, 9029-9036 (2019).

[222] Yu, X., Fu, S., Mandal, M., Yao, X., Liu, Z., Zheng, W., Samori, P., Narita, A., Mullen, K., Andrienko, D., Bonn, M. & Wang, H. I. *Tuning interfacial charge transfer in atomically precise nanographene-graphene heterostructures by engineering van der waals interactions*. J. Chem. Phys. **156**, 074702 (2022).

[223] Jnawali, G., Rao, Y., Yan, H. & Heinz, T. F. *Observation of a transient decrease in terahertz conductivity of single-layer graphene induced by ultrafast optical excitation*. Nano Lett. **13**, 524-530 (2013).

[224] Shi, S. F., Tang, T. T., Zeng, B., Ju, L., Zhou, Q., Zettl, A. & Wang, F. *Controlling graphene ultrafast hot carrier response from metal-like to*

semiconductor-like by electrostatic gating. Nano Lett. **14**, 1578-1582 (2014).

[225] Tomadin, A., Hornett, S. M., Wang, H. I., Alexeev, E. M., Candini, A., Coletti, C., Turchinovich, D., Kläui, M., Bonn, M. & Koppens, F. H. *The ultrafast dynamics and conductivity of photoexcited graphene at different fermi energies*. Sci. Adv. **4**, eaar5313 (2018).

[226] Pogna, E. A. A., Jia, X., Principi, A., Block, A., Banszerus, L., Zhang, J., Liu, X., Sohier, T., Forti, S., Soundarapandian, K., Terrés, B., Mehew, J. D., Trovatello, C., Coletti, C., Koppens, F. H. L., Bonn, M., Wang, H. I., van Hulst, N., Verstraete, M. J., Peng, H., Liu, Z., Stampfer, C., Cerullo, G. & Tielrooij, K.-J. *Hot-carrier cooling in high-quality graphene is intrinsically limited by optical phonons*. ACS Nano **15**, 11285-11295 (2021).

[227] Aeschlimann, S., Rossi, A., Chávez-Cervantes, M., Krause, R., Arnoldi, B., Stadtmüller, B., Aeschlimann, M., Forti, S., Fabbri, F., Coletti, C. & Gierz, I. *Direct evidence for efficient ultrafast charge separation in epitaxial WS_2/graphene heterostructures*. Sci. Adv. **6**, eaay0761 (2020).

[228] Wang, H. I., Infante, I., Brinck, S. T., Canovas, E. & Bonn, M. *Efficient hot electron transfer in quantum dot-sensitized mesoporous oxides at room temperature*. Nano Lett. **18**, 5111-5115 (2018).

[229] Wu, C., Zhang, Q., Liu, Y., Luo, W., Guo, X., Huang, Z., Ting, H., Sun, W., Zhong, X. & Wei, S. *The dawn of lead-free perovskite solar cell: Highly stable double perovskite $Cs_2AgBiBr_6$ film*. Adv. Sci. **5**, 1700759 (2018).

[230] Yang, X., Chen, Y., Liu, P., Xiang, H., Wang, W., Ran, R., Zhou, W. & Shao, Z. *Multifunctional dye interlayers: Simultaneous power conversion efficiency and stability enhancement of $Cs_2AgBiBr_6$ lead-free inorganic perovskite solar cell through adopting a multifunctional dye interlayer*. Adv. Funct. Mater. **30**, 2070147 (2020).

[231] Yu, Y. J., Zhao, Y., Ryu, S., Brus, L. E., Kim, K. S. & Kim, P. *Tuning the graphene work function by electric field effect*. Nano Lett. **9**, 3430-3434 (2009).

Acknowledgments

How time flies! Four years ago, I came here to MPIP with a strong curiosity about the world of physics; Four years later, I know this is what I want to do for the rest of my entire life. During this difficult but beautiful journey, there are so many people I want to acknowledge for leading and guiding me to the wonderful world of science, for helping and supporting me through the challenges every day in science and in life, for sharing and cherishing their friendship and love with me. It's these people who made my science so warm and made my life so bright.

For sure, everything would not be possible without my supervisor: Mischa Bonn. I can't believe how lucky I am to have you as my mentor in science. Thank you for offering me such an incredible opportunity to work in this Department at a world-leading institute. Thank you for being there whenever I need you for a discussion. It doesn't matter if it's in the lab, in the office, or even when you are at home. It doesn't matter if it's a workday or on the weekend. I need you, and you will be there. I won't take this for granted. Thank you for always bringing brilliant ideas to my works and keeping me in the right direction in science. Also, thank you for being so generous, kind, and funny to all of us.

Hai Wang, my co-supervisor, is one of the most important people in my PhD career. You are such a wonderful person and passionate scientist who has had a big influence on me. You taught me everything I need to do science. You taught me how to perform THz spectroscopy, how to give a good presentation, how to analyze and organize the data in a paper, how to communicate and collaborate with others, and so on. Thank you for always being patient with me when I couldn't get your point in our discussions. Not only in science, I express my gratitude to you for being a good friend to me in life as well.

Laurie, I can't thank you enough for everything you did and are doing right now for me and for all of us. Since the first day I came here, you are the one I went to first whenever I got problems with my life. Your big smile and kindness make me feel so welcomed and so relax. Your incredible work holds us as in a big family. Thank you!

It's a great pleasure to have a worldwide collaboration with many excellent people. All the work in this thesis relies on a tight and productive collaboration with Prof. Elke Debroye and Prof. Johan Hofkens from KU Leuven. Thank you for providing us with the best perovskite samples. Prof. Aron Walsh and Prof. Jarvist M. Frost from Imperial College London, thank you for the theoretical input for our work in Chapter 4. Prof. Yanfa Yan and Dr. Xiaoming Wang from the University of Toledo, thank you for the effective mass discussions. Prof. Arjan Houtepen and Indy du Fossé from TU Delft, thank you for the transient absorption measurement. Dr. Zhaoyang Liu and Dr. Can Wang from ISIS, thank you for the device measurement. Besides,

I'm grateful to have close in-house collaboration with Dr. Charusheela Ramanan and Esther del Pino Rosendo. You have done great works.

There is a group of people I want to express my special acknowledgment to, my group members, teammates, the Low-dimensional Stars. These people are: Alex, Paniz, Xiaoyu, Wenhao, Shuai Fu, Xiaoqing, Shuai Chen, Lucia, Pushpendra, Lei, Min, Samir, Jiabao, Jingyin, Sven, Aliaa. Among these people, there is one who is so cool, my friend, Alex. Thank you for helping me with all the documents, lab tour, supermarket shopping at my first day here in MPIP. Thank you for all the encouragement and pleasant conversations you brought to me. And thank you for messaging me and keeping our friendship after you finished your PhD. Paniz, I miss you from the bottom of my heart. You are such a beautiful and lovely person. Thank you for always talking to me and helping improve my English-speaking skills when I just came here. I still can't believe I said 'Thank you' when you welcomed me by saying 'Nice to meet you!' the first time we met. Xiaoyu, you are truly one of the smartest people I know. I have learned a lot from you about the magic graphene. Wenhao and Shuai, what can I say? We learn from each other, laugh with each other, and help each other to be the best in ourselves. I would definitely have had a different PhD career without you. Thanks! Lucia, Xiaoqing, Shuai C, thank you for the theoretical and technical help whenever I came to you. I wish you all the best!

Except for my group members, there are more people I have to give my genuine appreciation for the help in my work. Heejae, Ronald, Xiaomin, Keno, Marco, Peng, Wentao, Eduard, Jaco, Sheng, Yongkang, Pankaj. You have helped me in different ways. I have learned a lot from the discussions with you. A special thanks to Jaco for the Dutch translation of my thesis summary. I would like to thank Maksim for helping me with the broadband THz setup. It's been a wonderful and fruitful experience for me.

Next, I want to thank our terrific in-house technicians: Marc-Jan, Florian, Hansjörg, Detlev-Walter, Gabi, Leon, Jürgen. I couldn't have done my experiments without your help. Thank you for your excellent work, which builds the foundation for our department.

In addition to the great science, I enjoyed my time here very much also due to many wonderful friends inside and outside of MPIP. I want to first thank my officemates for their pleasant company in these years: Prerna, Giovanni, Alex, Lucas, Veronika, Alankar, Ali, Xiaoqing, Sheng. You have made my office time full of joy. Bence, Hao (Lyu), Daizong, Shumei, Cong, Jing Chen, I have enjoyed so much the conversations we had from now and then. Lijun, I feel so lucky to meet you the first day I came to MPIP. You are the kindest person. Hongyan and your cute baby Huanghuang, thank you for bringing so much fun to my wife and me. Junlong, thank you for being my big brother in Germany. I will never forget the great moment with you of drinking wines, playing basketball, and house moving. Your wife Sunqiao, my big sister, thank you for always welcoming us and helping us with life issues. Wish your brilliant kid Julian a healthy and bright future! Fan and Xiaohua, I wish you a happy wedding

and a beautiful marriage journey. Laoxu, Mingsen, Teng Wu, Shuai Jiang, and Shiqi, thank you for the wonderful time we shared for basketball. I will certainly miss you guys.

In the end, I want to give my biggest thanks to my family. I want to thank my parents for taking care of me and supporting me all the time. I have no words to express my super gratitude to you. My parents-in-law, thank you for trusting me and letting me take care of your daughter. Last but definitely not least, my wife Nan Wang, my sweetheart, my everything. Thank you for loving me and marrying me. Thank you for always having my back and making me laugh. Thank you for all the sacrifices you made and are making right now for our small family. Life couldn't be happier.